A University of Sussex PhD thesis

Available online via Sussex Research Online:

http://sro.sussex.ac.uk/

This thesis is protected by copyright which belongs to the author.

This thesis cannot be reproduced or quoted extensively from without first obtaining permission in writing from the Author

The content must not be changed in any way or sold commercially in any format or medium without the formal permission of the Author

When referring to this work, full bibliographic details including the author, title, awarding institution and date of the thesis must be given

Please visit Sussex Research Online for more information and further details

UNIVERSITY OF SUSSEX

Mathematical studies of a mechanobiochemical model for 3D cell migration

Laura Murphy

Submitted for the degree of Doctor of Philosophy

University of Sussex

September 2018

Declaration

I hereby declare that this thesis has not been and will not be submitted in whole or in part to another University for the award of any other degree.

Signature:

Laura Murphy

UNIVERSITY OF SUSSEX

Laura Murphy, Doctor of Philosophy

Mathematical studies of a mechanobiochemical model for 3D cell migration

Summary

This work presents the development, analysis and numerical simulations of a model for cell deformation and movement, which couples biochemical reactions and biomechanical forces. The way that cells move is key to the creation and development of most organisms on earth. Consequently a deeper understanding of cell motility is likely to have significant applications to medicine. We propose a mechanobiochemical model which considers the actin filament network as a viscoelastic and contractile gel. The mechanical properties are modelled with a force balancing equation for the displacement. The pressure and contractile forces are influenced by actin and myosin and we model these with a system of reaction-diffusion equations.

The model consists of highly non-linear partial differential equations. To analyse the model, we carry out linear stability analysis to determine key bifurcation parameters and find analytical solutions close to bifurcation points. We then approximate the equations and produce numerical solutions in multi-dimensions, using an evolving finite element method. The solutions predicted from linear stability theory are replicated in the early stages of cell movement. Subsequently, both simple and complex deformations, such as expansions, protrusions, contractions and translations of the cell are observed.

This theoretical and computational framework allows the study of more complex and experimentally driven reaction kinetics involving, actin, myosin and other molecular species that play an important role in cell movement and deformation.

Acknowledgements

I am hugely grateful to my supervisor Professor Anotida Madzvamuse for introducing me to this topic and for his enthusiasm, patience and kindness throughout my studies. I am also very grateful to Dr Chandrasekhar Venkataraman for his co-supervision and support even after leaving the department. Many thanks to Professor Peter Giesl for his very helpful advice during annual reviews. I would like to thank my colleagues in the School of Mathematical and Physical Sciences in particular Mr Albert Asawaroengchai, Dr Andy Chung and Dr Laurie Trott helping me develop my programming skills early in my research. Additionally, many thanks to Rosanna Barnard, Bootan Rahman, Benard Kipchumba Kiplangat, Eduard Campillo-Funollet, Muflih Alhazmi, Davide Cusseddu, Victor Juma, James van Yperen, Joe Eyles and many others in the department for all the friendly and insightful discussions.

This work was jointly funded by the University of Sussex and the Engineering and Physical Sciences Research Council, who have my lasting gratitude.

I would also like to thank my parents, Louise Manners and Phillip Murphy, for their love and support throughout my life and my sister Isabelle for her excellent advice, and unflinching and aggressive support. And finally to my friends, for keeping me smiling this last year.

Contents

List of Tables

List of Figures

Chapter 1

Introduction and Background

1.1 Introduction to cell motility

Cells embody and empower every living creature on earth. Given their great complexity and variety, there are endless biological and physical questions to answer. Cell biologists and biochemists attempt to uncover the chemical composition of cells (Berg et al., 2015) and the different components and processes (Cooper, 2000). Then taking this into account, how, and why, does a cell grow, divide and die? (Alberts et al., 2002). The question we want to help answer is crucial to evolution and medicine, from the very simple first cells that existed, to the millions that work together inside our bodies: How, and why do cells move? Cells were first observed to move under a microscope in 1674 by Anthony van Leeuwenhoek, and from then onwards, scientists have been investigating and hypothesising on the mechanisms involved. The movement of cells from one location to another helps unicellular organisms to find nutrients. Cell movement is just as critical in multicellular organisms due to roles in embryogenesis, wound healing, immune response, cancer metastasis, tumour invasion, and other processes, therefore, understanding cell movement is of great importance to medicine and to understanding our origins (Bray, 2001; Friedl and Gilmour, 2009; Brinkmann et al., 2004; Condeelis and Segall, 2003).

Some methods of movement are easier to explain than others, for example, many bacteria and sperm cells have a tail which rotates to propel the cell body forward. There are many other ways a cell can move such as crawling, swimming and squeezing mechanisms. They can move collectively or individually. In this thesis, we restrict ourselves to single cell movement, collective cell movement will be an interesting extension.

Cell motility combines complex biochemical reactions and biomechanical forces to move a cell through an environment. Many mechanisms of movement depend on changes to the

shape of the cell, which is defined by the space that it occupies (Paluch and Heisenberg, 2009). The cell is confined by a plasma membrane, thus, its shape is dependent on the internal and external forces which act on the membrane, as well as the stiffness and curvature of the membrane itself. The internal forces are primarily produced by a complex filamentous network, the cytoskeleton, which supports the cell. A key component of the cytoskeleton is actin, a globular protein which polymerises to form filaments, which in turn form relatively rigid bundles and networks. Myosin is a motor protein which attaches to filaments causing contractions which pull on the membrane. In contrast, the polymerisation of actin filaments, and/or osmotic pressure from contractions, can push the membrane outward. The external forces on the membrane are usually due to adhesions and confinement in an extracellular matrix. To balance these forces the cell needs tight regulation through signalling and feedback between protein activation and mechanical properties of the cell and its environment (Paluch and Heisenberg, 2009).

The most commonly described and modelled motility is a crawling mechanism which consists of three steps: protrusion at the front of the cell, adhesion to the surface at the front while adhesions at the back weaken, and finally a contraction of the rear (Mogilner, 2009; Rafelski and Theriot, 2004). This two dimensional model works well and is applicable to cells translating across a surface. However, in most cases *in vivo*, cells are moving in three dimensions, often through dense and varying environments. Thanks to advances in microscopy, it is now possible to observe cell movement in three dimensions (Petrie and Yamada, 2012). Along with these advances there has also been huge increases in computing power, this means computing in three dimensions is not as time consuming as it once was. The protrusion, adhesion and contraction processes are still seen but in highly varying amounts, for example some cells can move fast with little to no adhesion to their surroundings, while others have little need for contraction (Petrie et al., 2012; Poincloux et al., 2011; te Boekhorst et al., 2016). In addition, it has been observed that cells can change their mode of motility due to changes in conditions, for example, the introduction of drugs which inhibit a certain method of movement, or migration into a different environment (Sanz-Moreno et al., 2011; Wolf et al., 2003; Sahai and Marshall, 2003).

The objective of this chapter is to give the relevant biological background which is considered when formulating the cell movement model, and to provide an overview of mathematical approaches which have been implemented. In the next section we will detail the biology involved in cell movement. In Sections 1.3 and 1.4 we will review the existing

mathematical models. Section 1.5, and 1.6 introduce numerical methods, in particular the finite element method, used to produce simulations of mathematical models proposed in this thesis.

1.2 Biological Overview

1.2.1 Why study cell motility?

Cells are the fundamental unit of life. They have existed on earth for at least 3500 million years (Schopf et al., 2007). There are similarities in structure between those first cells and the multitudinous, diverse types of cells which exist now. A fundamental question in biology is how cells group together to form tissues, which become organs, providing different functions inside organisms, from fruit flies to human beings. The first cells did not move autonomously since their environment contained the food and energy they required. However to evolve further they needed to create their own energy. They do this using adenosine triphosphate (ATP), giving them the energy required to replicate and move (Cooper, 2000). This movement is what we wish to understand. In this section we will motivate this and give a non-mathematical description of cells, in particular the components and processes involved with movement.

Motility, is defined as "the ability of a living system to exhibit motion and to perform mechanical work at the expense of metabolic energy" (Allen, 1981). Or more simply in our case: a cell can make itself move. Single celled organisms use a process called chemotaxis to detect chemical signals which tell them which direction has the highest concentration of food (Petrie and Yamada, 2012; Eisenbach, 2004; Bray, 2001). In multicelluar organisms, it is vital to understand motility because it is a key behaviour for growth, repair, and defence (Bray, 2001). Cells can move collectively to build and repair complex tissues, for example, the organisation of cells during the development of different organs in an embryo, and the migration of a large sheet of epithelial cells over a wound (Friedl and Gilmour, 2009). However in this work we focus on a cell moving independently. Single cell movement allows cells to integrate into tissues or migrate around the body (Friedl and Wolf, 2009). The most established example is neutrophils (the most common type of white blood cells). Neutrophils also use chemotaxis to follow stimuli to sites of inflammation or infection where they can engulf and kill bacteria (Bray, 2001; Brinkmann et al., 2004). A second example of crucial importance in oncology, is the need to understand metastasis, this happens when cancer cells can move from a primary tumour into the bloodstream,

and create new tumours in different organs, this is a often when cancer becomes its most deadly (Chambers et al., 2002; Condeelis and Segall, 2003). Thus, the importance to medicine is clear. To begin, we need to introduce the main parts of a cell.

1.2.2 What are the important components in a cell?

Cells can be divided into two types. First, prokaryotes are typically single-celled organisms like bacteria and are identified as lacking a nuclear envelope to enclose genetic material. Secondly, eukaryotes are generally bigger and more complex. The first eukaryotes were single celled, and many still are, with yeast being an example. Others evolved to group together, become specialised and divide labour to make up the plants and animals which exist today. Prokaryotes and eukaryotes both have an enormous diversity of subtypes. Here we focus on eukaryotes and outline several of a cell's integral parts.

Definition 1.2.1. *(Nucleus)* The nucleus is where most of the genetic material (DNA) of the cell is enclosed in a membrane. This provides the stability for DNA to form structures which control functions within the whole cell (Cooper, 2000).

Definition 1.2.2. *(Membrane)* The cell is bordered by a plasma membrane which protects and allows the cell to interact with its surroundings. It is selectively permeable to substances in and out of the cell. Embedded in the membrane are proteins called *integrins*, which allow the cell to adhere to the extracellular matrix and are involved in signalling within and between cells (Alberts et al., 2002).

Definition 1.2.3. *(Cytoplasm and Cytoskeleton)* The cytoplasm is everything enclosed in the membrane but the nucleus. This includes membrane bound organelles suspended in a water-solution called cytosol. It also contains the cytoskeleton which is a dense network of filaments which support the structure and aid transport of substances around the cell. The filaments have three types: microtubules, intermediate filaments and microfilaments (also known as actin filaments). Table 1.1 summarises the differences between the three. These filaments support and are supported by crosslinking, motor and regulation proteins, actomyosin complexes and ions (Pullarkat et al., 2007). Microtubules are stiff hollow polymers that transfer materials within the cell. Intermediate filaments play an indirect role in reinforcing elasticity in the cell (Pullarkat et al., 2007). Actin filaments, and the myosin motors which attach to them, are thought to be especially significant in cell motility therefore are the two proteins we will consider in our generalised mechanobiochemical model. Next, we describe in more detail the actin and myosin proteins, and their roles in cell motility.

	Actin	Microtubule	Intermediate
Thickness	~ 8 nm	~ 25 nm	~ 10 nm
Persistence length	~ 10 μm	~ 1 mm	~ 0.6 μm
Polar?	✓	✓	×
Formed from	globular actin	tubulin	keratin, vimentin +
Associated motor proteins	myosin	kinesin, dynein	none known
Disrupted by drug?	Latrunculin-A	Nocodazole	not easily

Table 1.1: Properties of cytoskeletal filaments (Pullarkat et al., 2007)

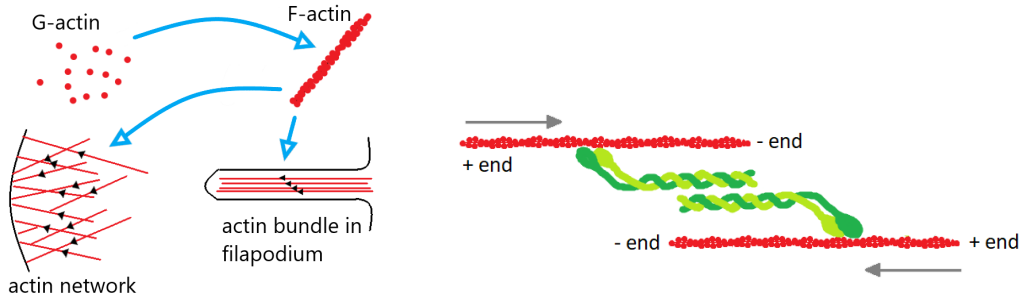

(a) (b)

Figure 1.1: (a) Actin globular subunits (G-actin) arrange into long spiral chains called filaments (F-actin) which in turn arrange into either bundles or networks. During cell motility both bundles and networks can push on the cell membrane to produce a protrusion at the front of the cell (in this figure the membrane is the black line. The plus end of the filament is where polymerisation occurs and black arrows point to this end). (b) Myosin II (in green) attaches to actin filaments and pulls in the direction of the grey arrows.

Actin

Actin is a globular protein which forms filaments in virtually all cells and is crucial for cell structure and movement (Cooper, 2000). The filaments assemble into long bundles and mesh networks (Figure 1.1). This provides scaffolding for the cell's movement and function.

Actin filaments are polarised, with growth at one end and disassembly at the other. This polymerisation by actin subunits, and subsequent elongation of filaments, as well as depolymerisation is the most widely studied and understood mechanism for movement in the cell (Bray, 2001; Mogilner, 2009). Drugs that stabilise or depolymerise actin filaments completely stop movement (Carlier et al., 2015). Polymerisation and depolymerisation will form part of our modelling, as described in Section 3.2. The "treadmilling" of actin

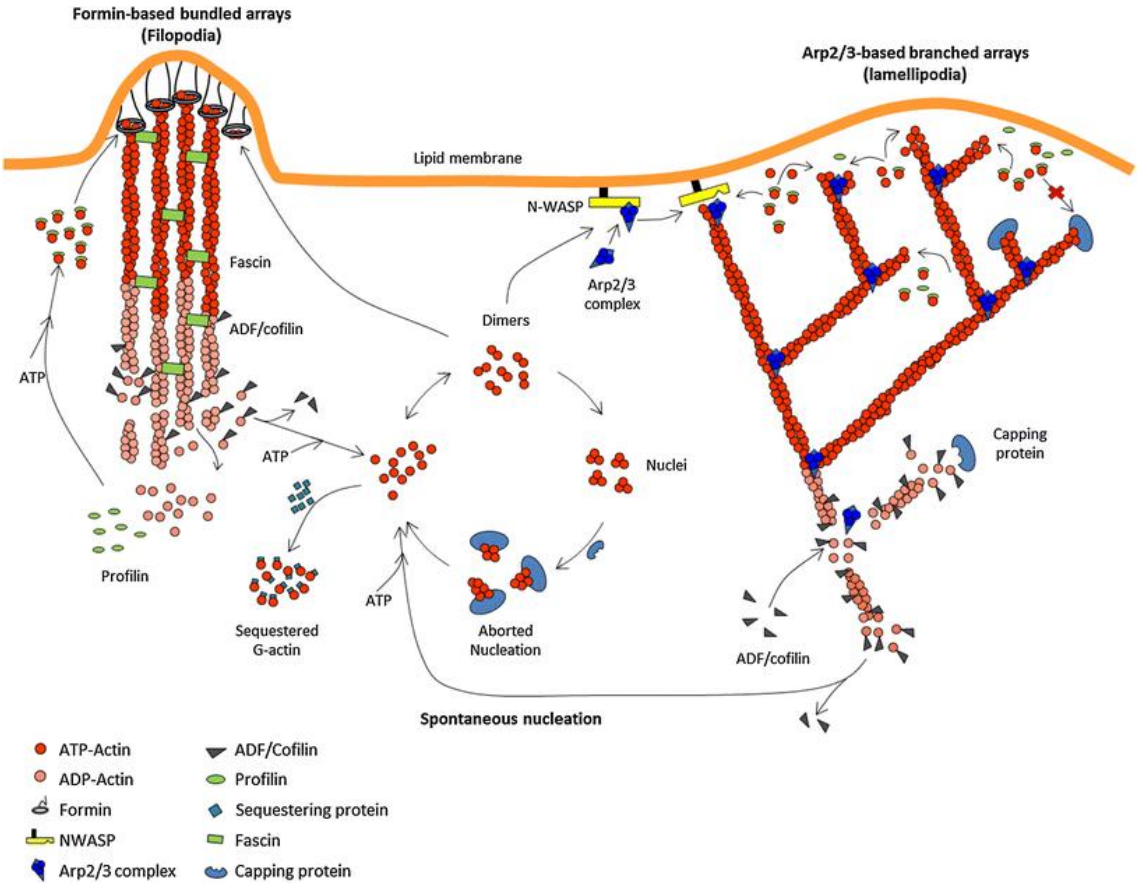

Figure 1.2: The barbed (plus) end of an actin filament is where regulation of assembly is most significant. In this figure, we see the various agonists and antagonists of filament assembly. Barbed ends elongate and push on the membrane. Capping proteins halt elongations. ADF/cofilin severs and depolymerises older filaments. (With permission from Carlier et al. (2015).)

has been described in detail in, for example, (Pollard and Borisy, 2003; Ananthakrishnan and Ehrlicher, 2007; George, 2012; Mogilner, 2009). Figure 1.2 shows some of the many protein machineries involved.

Myosin

Myosin II is a motor protein which converts chemical energy (ATP) into mechanical power (Cooper, 2000). It is fundamental for muscle contraction but also plays an important role in contractions during cell motility (Bray, 2001; Alt and Dembo, 1999; Mogilner, 2009). Myosin attaches to actin filaments and slides them in opposite directions to produce the contraction (Cooper, 2000). The presence of myosin is observed across cell types, but the effect on motility varies (Murrell et al., 2015). Myosin is generally observed at the rear of the cell, where the force generated from pulling on the actin filaments produces the

contraction needed to pull the cell body forward. Wilson et al. (2010) show that myosin also has a direct role in actin disassembly, which may have an effect on contractility, since an excess of these rigid filaments would be harder to compact. Myosin II contractile activity can be reversibly stopped by the drug blebbistatin, hindering the cell's movements (Kovács et al., 2004).

1.2.3 Types of cell movement

Two-dimensional crawling

In vitro observations have motivated two-dimensional (2D) models of a cell crawling on a surface using three main processes: protrusion, adhesion and contraction (Abercrombie, 1980; Mogilner, 2009). These processes can happen in turn or, more often, continuously and simultaneously. Protrusion is part of the cell extending in the direction of motion. The main component of a protrusion is usually filamentous actin taking the form of wide, flat lamellapodia, or long, thin filapodia (illustrated in Figure 1.2) (Mogilner and Edelstein-Keshet, 2002a; Mogilner and Rubinstein, 2005; Atilgan et al., 2006; Carlier et al., 2015). The area of the protrusion then strongly adheres to the surface while mature adhesions at the rear weaken (Bershadsky et al., 2006). Finally, a myosin induced contraction of the trailing edge completes the translocation of the cell (Svitkina et al., 1997). This 2D crawling mechanism is preferred by some single celled organisms such as amoebae and diatoms since it is more efficient for survival than swimming in a three dimensional (3D) environment (Bray, 2001). The most recognised shape of motility is the semicircular or fan shape which is commonly used by keratocytes. The majority of a keratocyte's area is a lamellapodium which pushes outwards and attaches itself to the substrate. Simultaneously, actomyosin contraction pulls the rear of cell together and towards the front of the cell. Thus the cell appears to keep its shape while translating. This is illustrated in Figure 1.3. Modelling in two dimensions can help us understand the role of cell motility in wound healing, and migration on blood and lymph vessels (Schneider et al., 2010; Carlin et al., 2013). 2D models have limited application, however, since cells on a 2D surface move differently to those moving in a more true to life 3D environment.

Note that in this thesis we will use 1D, 2D and 3D to mean either one-/two-/three-dimensional or one/two/three dimensions, interchangeably.

Three-dimensional cell movement

In vivo cells generally travel in three dimensions through diverse environments such as

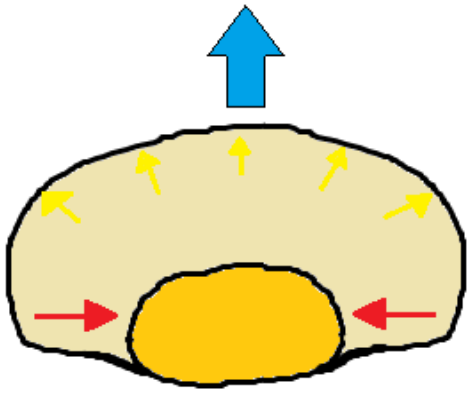

Figure 1.3: The characteristic shape of a keratocyte crawling. Blue arrow is the direction of motion, yellow arrows are the protrusive force due to actin polymerisation and red is the contractile forces. The darker yellow is the nucleus. The cell stays approximately the same shape as it migrates upwards.

body fluids, or dense connective tissue referred to as the extracellular matrix (ECM). Because of these diverse environments, the cell crawling model is just one of many observed modes of migration (Petrie and Yamada, 2012). For example, in dense tissue, cells deform significantly and sometimes use traction from adhesions, whereas in bodily fluids they become rounded, lack adhesions, and undergo passive drift or propel themselves using actomyosin flow (te Boekhorst et al., 2016; Poincloux et al., 2011; Tjhung et al., 2015; Chan et al., 2015).

Some cells can only use one mode of migration, however, many can change their mode due to changes in environmental conditions. Mode switching is a topic of much interest for two reasons. Firstly, attempts to control cancer cell motility by using a drug which inhibits a method of movement have resulted in cells adapting by moving using different mechanisms (Wolf et al., 2003; Sahai and Marshall, 2003; Petrie et al., 2012; Sanz-Moreno et al., 2011). Secondly, in the process of metastasis, cancer cells are able to change modes in order to move from one type of tissue to another, for example, breast cancer cells can migrate into the very different environment of bone (Katti and Katti, 2017).

The three most commonly discussed migration strategies are termed mesenchymal, amoeboid and blebbing. We briefly describe each of these modes below. Some studies define up to 6 distinct modes (Zhu and Mogilner, 2016) which are variations and combinations of these three.

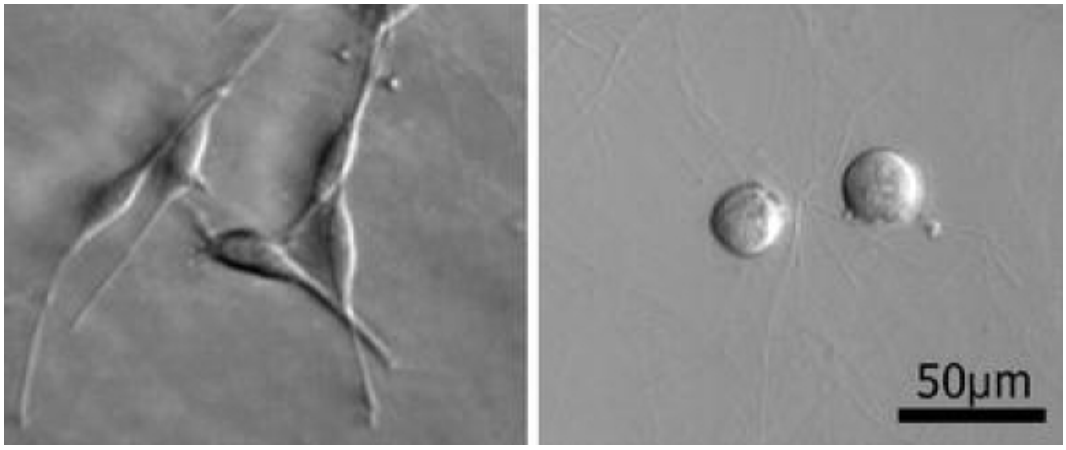

Figure 1.4: Different morphologies of the invasive tumour cells. Left mesenchymal morphology of K4 sarcoma cells. Right amoeboid morphology of A3 sarcoma cells (representative modulation contrast image recorded at an invasion depth of 50 μm). (With permission from Paňková et al. (2010)).

Mesenchymal

Mesenchymal motility mode is characterised by an elongated shape, protruding at the front and retracting at the rear. This mode relies on adhesions in the same way as 2D crawling. In contrast to 2D migration, 3D cell migration is often more spindle-like with one or more leading pseudopods. In addition, when migrating in this way, the cell utilises proteolysis which entails enzymes breaking down ECM to create a path for migration (Paňková et al., 2010). Examples of cells which commonly use mesenchymal migration are fibroblasts, keratinocytes and endothelial cells (Aguilar-Cuenca et al., 2014; Paňková et al., 2010).

Amoeboid

During amoeboid motility, the cell has a rounder shape and uses pressure to squeeze through or deform, instead of degrading, the ECM. The cell forms actin networks or blebs at the front of the cell and uses little to no adhesion. This means amoeboid is faster than mesenchymal movement. The name comes from the movement of amoeba and can also be seen in leukocytes and some tumour cells (Aguilar-Cuenca et al., 2014; Sahai and Marshall, 2003; Wolf et al., 2003).

Blebbing

Blebs are round expansions at the edge of a cell commonly observed during apoptosis (cell death) (Mills et al., 1998) and cytokinesis (cell division) (Porter et al., 1973). They are caused by an increase in pressure and the decoupling of the membrane from the actin cortex, this causes cytosol to flow out of the cortex and inflate the bleb (Charras, 2008; Cunningham, 1995). In most cases, the bleb then retracts, however when it does not, it has been observed to induce motility (Friedl et al., 2001; Sahai and Marshall, 2003; Even-Ram and Yamada, 2005; Wolf et al., 2003; Fackler and Grosse, 2008). In this case, when a bleb stops growing an actin cortex is reformed on the membrane. This action can produce sustained movement when the cell is polarised, with a sustained bleb at the front of the cell and the rear of the cell contracting to move the whole cell forward.

Consideration of the nucleus

Generally, in two dimensions, the nucleus is considered a passive cargo at the rear. However the contribution of the nucleus cytoskeleton to movement is a current area of interest. The location of the nucleus in migrating cells varies widely, particularly when considering three dimensions. The nucleus is much more rigid than the rest of the cell which can hinder the cell's movement through small gaps in the extracellular matrix (Friedl et al., 2011; Cao et al., 2016). In contrast, the nucleus appears to play a part in, for example, leukocyte migration where it is positioned at the front, Barzilai et al. (2017) observed nuclear lobes being incorporated into lamellapodia which generated gaps between and inside the endothelial cells. This could be described as the nucleus helping to drill through endothelial layers (Calero-Cuenca et al., 2018).

Collective migration

Cells can move in sheets in two dimensions during wound healing or in strands, or clusters, through a three-dimensional environment. These processes utilise actin and myosin in a similar way to single cell migration but also employ junctions between cells to collectively polarise, generate force and make decisions (Friedl and Gilmour, 2009). Collective cell migration is lesser studied than single cell migration and cell-to-cell communication is not considered in this thesis but could be an extension of the model in the future.

Next we will review mathematical and computational models which may aid our understanding of cell movement.

1.3 Mathematical models of cell motility

There are thousands of proteins and processes involved in cell motility, so choosing which processes to focus on is a daunting task. Accordingly, the problem of mathematically modelling this movement has been approached in numerous ways. There are many models which model a certain aspect of cell movement, for example, how protrusions are affected by the concentration and orientation of actin filaments, and the stiffness of the membrane (Mogilner and Edelstein-Keshet, 2002a; Mogilner and Rubinstein, 2005; Atilgan et al., 2005, 2006). Mogilner and Edelstein-Keshet (2002a) found that the ability of a cell to create a protrusion is correlated with the number of barbed ends of actin filaments pushing at the membrane. If there are too few filaments then the force is not strong enough to cause a protrusion, while if there are too many this decreases the velocity because there are fewer monomers around for the filaments to extend themselves. Additionally, the significance of the size and amount of actin filaments, and the stiffness of the membrane and shown in Mogilner and Edelstein-Keshet (2002a), Mogilner and Rubinstein (2005) and Atilgan et al. (2006). Another principal aspect concerns the assembly and disassembly of adhesions (Webb et al., 2002).

Our model considers the whole cell, rather than just one aspect, therefore we will discuss some existing models. First we will consider models in different dimensions, then in Section 1.4 we will discuss particular types of models that relate to our objectives. Table 1.2 orders all the models we discuss by dimension and by year published.

1.3.1 One- and two-dimensional mathematical models

As is often the case it makes sense to first consider just one dimension. A simple 1D model by DiMilla et al. (1991) described cytoskeletal force with viscoelastic-solid model with compartments containing springs, dashpots and contractile elements in different arrangements. Nodes are linked with the substrate through dashpots and can be added at the front and deleted at the rear. The model hypothesised that the cell speed is controlled by the difference in adhesion at the front and back of the cell. If the difference is increased, the velocity increases even when the adhesiveness of the substrate is different.

To obtain a more realistic view of cell movement, it makes sense to consider a continuous model. For example in Gracheva and Othmer (2004), the 1D model considers the cell to have a viscoelastic cytoskeleton, with actin polymerisation causing an active protrusive force and myosin II motors creating contractile stress. It also incorporates integrin receptors to model adhesion to a substrate. The model's numerical solutions display areas

1D	2D	3D
DiMilla et al. (1991)	Lewis and Murray (1991)^{R}	
	Lee et al. (1993)$^{-}$	
	Alt and Tranquillo (1995)^{R}*	
Caille et al. (2002)		
		Karcher et al. (2003)
Gracheva and	Stephanou et al. (2004)^{R}	
Othmer (2004)^{R}		
	Rubinstein et al. (2005)^{R}	Zaman et al. (2005)
Larripa and		Du et al. (2006)*
Mogilner (2006)^{R}		Zaman et al. (2006)
	Darling et al. (2007)	Gladilin et al. (2007)
	Rubinstein et al. (2009)^{R}	
		Wolgemuth and Zajac (2010)^{R}
	Neilson et al. (2011)^{R}	Hawkins et al. (2011)^{R}
	Chen et al. (2012)	Elliott et al. (2012)^{R}
	George (2012)^{R}	
	Shao et al. (2012)^{R}*	
		Tozluoğlu et al. (2013)
	Sakamoto et al. (2014)^{R}	
	Dreher et al. (2014)^{R}	
	Blazakis (2015)$^{-}$*	Tjhung et al. (2015)
	MacDonald et al. (2016)^{R}*	
	Cao et al. (2016)	Zhu and Mogilner (2016)
	Camley et al. (2017)^{R}	Katti and Katti (2017)*
		Campbell and Bagchi (2018)^{R}*

Table 1.2: Features of different models are highlighted in this table. All but those labelled with $^{-}$ consider mechanical forces and those labelled ^{R} consider reaction kinetics. Labelled * are discussed in the numerical methods section.

of stretch and compression and a number of agreements with experimental data: Firstly, at the front of the cell the traction is large and negative while at the back it is large and positive. Secondly cell speed as a function of cell-substrate has a similar bell-shaped distribution to experimental observations.

However, a one-dimensional model is not appropriate for many cell types. The motion of keratocytes must be considered in two dimensions because key active forces act orthogonal to the direction of motion. A cell moving across a flat surface (often a keratocyte in its characteristic fan shape) is the basis of most *in vitro* studies. The shape is shown in Figure 1.3. Two dimensional models are the most common in literature because they can satisfactorily model this type of movement.

An early 2D model for cell migration is that proposed by Lee et al. (1993) which gave a simple geometric formula for movement. This model was based on the suggestion that extension and retraction of the cell boundary is locally normal to the boundary and local rate of extension/retraction decrease from the centre to the sides of the cell. This model provides an understanding of semi-circular moving cells, but does not identify how this might be regulated by the cell.

Another noteworthy and much more complex 2D model by Rubinstein et al. (2005) considers the actin network as elastic. Coupled to this is a convection-reaction-diffusion model of actin transport, and a 1D model for actomyosin contraction at the rear of the lamellipod. The simulations showed the persistent crescent shaped movement observed in keratocytes. Notably this does not occur if the initial shape is a disk. Cell turning can also be simulated. In a later paper Rubinstein et al. (2009) considered a steadily moving cell as viscoelastic and computed the actin flow, myosin distribution and traction forces in order to compare this to experimental values. The viscoelastic movement of the cell is powered by myosin contraction, which happens at the rear. The reason for aggregation of myosin at the rear is that, when the cell is moving, the relatively stiff F-actin network has graded assembly and disassembly from front to back, and so myosin effectively is swept to backwards.

As previously mentioned 2D modelling can tell us much more about how cells move on a surface, in Rubinstein et al. (2005) they suggest the fan shape is likely to be the "pure form" of a cell crawling. However, many cells do not have a steady shape when moving and, more importantly, a flat surface is not the environment most cells find themselves in. *In vivo*, the majority of cell movement is in a three-dimensional environment.

1.3.2 Three-dimensional mathematical models

Modelling 3D migration can be approached in many ways, most of which consider the ECM. This is because, in 3D environments, the dense fibres affect how a cell can push forward. An early effort by Zaman et al. (2005) modelled motion of the centre of a cell by balancing forces at discrete time steps. Under this model, maximum speed is predicted at intermediate ECM stiffness and intermediate amounts of cell-matrix adhesion. However, this model did not consider the shape of the cell and the difference in forces between the front and rear. A more recent, multiscale model of cancer cell motility was presented by Tozluoğlu et al. (2013). It is a hybrid, agent-based/finite-element model which incorporates actin protrusions, contractility, the cell nucleus, adhesions, changes in the ECM, and blebbing. Similar to Zaman et al. (2005) the model predicts that speed is affected by the level of adhesion and that traction forces for amoeboid motility could be provided by steric interactions between the cell and the ECM. Sakamoto et al. (2014) investigated the effects of both internal cell mechanics and adhesions on migration behaviour. The proposed hyperviscoelastic model predicted that the transition between the amoeboid and mesenchymal (elongated) migration modes are caused by reduced adhesion and increased elongation/retraction rates.

A computational approach to modelling further adaptability of migration modes was recently proposed by Zhu and Mogilner (2016). The cell and ECM are treated as 2D node-spring networks connected, but kept separate, by a node-spring chain representing the membrane. They found that, by varying the adhesions, locations of protrusion and contraction, and including or excluding degradation of the ECM, the model reproduces six distinct modes of motility which have been observed in experiments. These modes are mesenchymal, chimneying, amoeboid, blebbing, finger-like protrusion and rear-squeezing. The authors also note that since it is a discrete model it should be developed in parallel with continuous 3D models such as the one we propose in this study.

The models of Tozluoğlu et al. (2013); Sakamoto et al. (2014); Zhu and Mogilner (2016) are essentially in 2D but model 3D behaviour. There are also several models in 3D which model movement on a 2D surface (Holmes and Edelstein-Keshet, 2012; Tjhung et al., 2015). Tjhung et al. consider a crawling cell by presenting a simplified physical model of an active fluid droplet which supports the idea that cells may use physics based mechanisms which do not directly depend on biochemical feedback networks.

A model which addresses a significantly different mode of migration to the classical 2D idea is that of Hawkins et al. (2011) which assumes cell to be a spherical surface. By

considering instabilities in the cell cortex the model shows spontaneous cell motility could be generated by acto-myosin contraction.

Surface PDEs are central element of many cell motility models (Neilson et al., 2011; Elliott et al., 2012; Campbell and Bagchi, 2018). Elliott et al. (2012) considered the cell membrane as an evolving surface whose movement was determined by internal and external forces including pressure (in the enclosed volume and outside), the bending and stretching of the surface, and a protrusive force which was linked to a reaction-diffusion equation posed on the surface. The model was similar to 2D model by Neilson et al. (2011) and the behaviour, such as pseudopod splitting, persisted into three dimensions. Numerical simulations of both models successfully imitated features of directed pseudopod-driven migration due to an external chemoattractant.

Mechanical forces and RDEs on an evolving surface are also part of the model of Campbell and Bagchi (2018) which effectively modelled highly deforming pseudopod-driven motility through a porous medium. The model included the resistance of the membrane to shearing deformation, bending and surface area dilation. The bending energy was modelled with a strain energy function and following Helfrich's formulation. On the evolving cell surface, the protein interactions which cause protrusions were governed by reaction-diffusion equations for activators and inhibitors. The activator concentration directly affected the protrusive force ($\mathbf{f}_p = \xi a_1 \mathbf{n}$, where ξ is the force per actin filament). Additionally, the cytoplasm and extracellular matrix were assumed to be incompressible, Newtonian fluids and obstacles were considered in the form of rigid, non-moving spheres. It was postulated that a deforming surface causes the RD system to be more unstable. Additionally, high curvature causes species to aggregate, this enhances the growth of pseudopods. The significant deformations predicted by the simulation were similar to experimental observations of cells squeezing through narrow spaces. It was observed in simulations that the deformability must be sufficiently large to induce efficient motility, this behaviour is experimentally observed in the more efficient migration of softer immune cells through tissue compared to stiffer fibroblasts (Petrie and Yamada, 2015). The model is a demonstration of non-adhesion driven motility. This model, and models of Elliott et al. (2012) and Neilson et al. (2011) do not include any protein interactions in the bulk of the cell.

1.4 Research thesis objectives

In order to model 3D cell migration, clearly there are countless modelling goals to consider. In this thesis, we will address the following research questions: What are the forces acting on and being produced by the cytoskeleton? How does the actin - myosin network self organise? How are these concepts connected?

In the next section we will discuss mechanical forces inside the cell and how they relate to cell migration and in Section 1.4.2 we discuss biochemical interactions.

1.4.1 Biomechanical models for cell migration

Cytoskeletal dynamics have been studied using numerous force balancing models (Sun and Zaman, 2017; Zaman et al., 2005, 2006; Camley et al., 2017). There are several models which consider the actin network as hyperelastic (Caille et al., 2002; Wang and Gao, 2011; Gladilin et al., 2007; Chen et al., 2012). From these studies it is reported that the stiffness of the cytoplasm increases nonlinearly and that when it is stretched it becomes more stiff and incompressible (Gladilin et al., 2007). Additionally, cell's stiffness depends significantly on the stiffness of the extracellular environment (Chen et al., 2012). Other models, similar to the one proposed in this study, consider the cytoplasm to be viscoelastic (Karcher et al., 2003; DiMilla et al., 1991; Darling et al., 2007; Larripa and Mogilner, 2006; Shao et al., 2012; Rubinstein et al., 2009).

As mentioned in Section 1.2.3 deformability of the nucleus can be a limiting factor for cell migration. Therefore, Cao et al. (2016) developed a chemomechanical model of nuclear strains and shapes for a cell squeezing through endothelial layers. The model considers the nucleus to contain a soft poroelastic material enclosed in a stiff elastic shell to represent the nuclear envelope, the mechanical resistance of which may be overcome by actin contraction and cytosolic back pressure.

To produce directional movement, there must be a mechanism to introduce polarity into the model. This may be done directly, by adding an asymmetry to one or more of the forces. An example is Wolgemuth et al. (2011), who describe a biophysical model for myosin contraction driven motility which deforms significantly but does not have a steady moving space until polarity is added to the model with graded actin treadmilling.

The concentration of F-actin has been modelled to affect forces in very different ways. For example, in Dreher et al. (2014), actin simply pushes on the membrane. The created protrusion force is likely to be confined to the periphery of the cell (Shao et al., 2012). In other models it is involved in generating contractile stresses and flows (Lewis and Murray,

1991; Stephanou et al., 2004; George, 2012). The rate of adhesions forming can also be considered to be proportional to the concentration of actin.

The concentration of myosin is thought to linearly affect either the stress (Gracheva and Othmer, 2004; Wolgemuth et al., 2011; Rubinstein et al., 2009; Hodge and Papadopoulos, 2012; Shao et al., 2012) or similarly the rate of contraction (Murrell et al., 2015; Bendix et al., 2008). The concentration of myosin and the stress forces in the cell have a positive feedback on each other, when attached to fixed point myosin induces movement of the membrane, conversely, myosin responds to membrane tension (Aguilar-Cuenca et al., 2014).

Actin and myosin interact with each other therefore the next question we address is how to understand the biochemical interactions between them.

1.4.2 Biochemical reaction kinetics

A plausible paradigm for the consideration of molecules involved in cell motility is to consider a reaction-diffusion system (Gierer and Meinhardt, 1972; Meinhardt, 1999; Turing, 1952; Schnakenberg, 1979) which typically take the form

$$\frac{\partial \mathbf{u}}{\partial t} = \mathbf{D}\Delta\mathbf{u} + \mathbf{F}(\mathbf{u}), \tag{1.1}$$

where $\mathbf{D}$ is the matrix of diffusion coefficients and $\mathbf{F}$ is a vector of reaction terms which may depend on the vector of concentrations, $\mathbf{u}$. Equations of this type have long been used to explain pattern formation in a great variety of areas. The seminal work by Turing (1952) presented the elegant and counter-intuitive theory that patterning could be driven by diffusion rather than reactions. This means a linearly stable homogeneous steady state in the absence of diffusion can be driven unstable by the presence of diffusion. This model is especially applicable in chemistry where the presence of diffusion-driven instability was first verified (Castets et al., 1990; Ouyang and Swinney, 1991). General reaction-diffusion systems are discussed in detail in Chapter 2.

Since there are many molecules which affect cell movement, reaction-diffusion systems have been widely proposed in cell motility models (Levchenko and Iglesias, 2002; Mogilner, 2009; Rubinstein et al., 2009; Hawkins et al., 2011; Camley et al., 2017). Many models of single cell motility focus on the key proteins actin and myosin Mogilner (2009), therefore, we next discuss various proposed reaction-diffusion models which emphasise different mechanisms between actin and myosin.

Actin can be described as scaffold for myosin (Murrell et al., 2015) but not all myosin within the cell is attached to the actin therefore many mathematical models consider

"bound" and "unbound" states. The amount of bound myosin generally depends on binding/unbinding rate constants and the amount of free myosin (Hawkins et al., 2011; Hodge and Papadopoulos, 2012; Rubinstein et al., 2005) as well as the concentration of actin (Gracheva and Othmer, 2004). Often, either unbound myosin, or the sum of bound and unbound, is treated as constant (Wolgemuth et al., 2011; Gracheva and Othmer, 2004; Hodge and Papadopoulos, 2012).

There are also various ways to consider diffusion. Shao et al. (2012) emphasise that the diffusion term for actin is not technically diffusion in the physical sense but is an effect of polymerisation and depolymerisation and can be thought of as having the same effect as diffusion. In their model, the diffusion coefficient for myosin is an inversely proportional function of actin concentration. Rubinstein et al. (2009) only have a diffusion term for unbound myosin, bound myosin and F-actin are instead affected by the drift of F-actin compared to the velocity of the lamellipod. This is similar to the actomyosin model in Wolgemuth et al. (2011), which does not have an equation for actin concentration and unbound myosin diffuses while bound myosin moves with the network.

It is observed that the actin network becomes weaker towards the rear of the cell and this is where myosin molecules (attached to actin filaments) become more concentrated (Mogilner, 2009). To compound this, it is thought that contraction causes disassembly of actin (Murrell et al., 2015) and that myosin bundles at rear reduce polymerisation of actin (Wolgemuth et al., 2011).

There are a great number of studies which consider directed movement utilising chemotaxis (Hillen and Painter, 2009), the majority of which model populations of cells and their collective migration. It has also been suggested that cells can amplify this signal or even self-generate gradients (Mackenzie et al., 2016). This is considered in a single cell by Neilson et al. (2011), often a very small difference in concentration across a cell can cause a cell to orient itself and move. Another such model, which has similarities to ours, is that of Mackenzie et al. (2016), and one counterpart MacDonald et al. (2016), the model includes reaction-diffusion equations on the surface and protrusive forces generated, these concepts are coupled to local degradation of chemoattractants to study how cells may interpret and create gradients and the resulting movement. In our model we do not consider an external attractant and model only random deformations.

In summary, actin and myosin can be modelled to react with each other and diffuse. Many cell motility models have been proposed to include one or two reaction-diffusion equations but the kinetics are usually very simple. We will propose a framework such that

it is possible for more complex dynamics to be considered.

1.4.3 A mechanobiochemical model for cell movement

In order to address the questions posed at the beginning of this Section 1.4, we will consider a mechanobiochemical model previously studied in George (2012), George et al. (2013) and Madzvamuse and George (2013), which we will extend to 3-dimensions as well as introducing for the first time, the role of myosin in the model. The model considers the cell to be viscoelastic and balances this with protrusions and contractions which are influenced by the concentration of actin. The previous model consisted of a force balance equation whose solution described the displacement of the cell and a reaction-diffusion equation for actin. The model of George (2012) was in 2D, and the first novelty of ours is that we will extend it into 3D, in the hope that it can be more applicable in real life. The second novelty is the additional consideration of myosin, this is implemented with a second reaction-diffusion equation for myosin and a new term in the force balance equation to represent contraction due to myosin is added. Unlike previous studies of this nature, our approach allows us to investigate more complex reaction kinetics between actin and myosin.

1.5 Numerical methods for cell motility models

In this thesis we wish to formulate and solve a mechanobiochemical model comprising of a system of reaction-diffusion equations and a viscoelastic mechanical model for cell movement and deformation. Given that the model in its full glory is highly nonlinear, exact analytical solutions are not possible to obtain in closed form, instead, we will seek to compute numerical approximations to these exact solutions. Numerical methods abound for solving complex PDEs. Methods that have been employed to model cell motility include finite differences, phase field methods, boundary element methods (BEM), immersed boundary methods or level set methods (LSM), (Alt and Tranquillo, 1995; Stephanou et al., 2004; Pozrikidis, 2005; Strychalski et al., 2010; Wolgemuth and Zajac, 2010; Bottino and Fauci, 1998; Neilson et al., 2011). Choosing a suitable method for a particular model is a balance between the ease of application within the model's framework and the reliability of solutions the produced.

Finite differences were used in previous incarnations of our model (Alt and Tranquillo, 1995; Stephanou et al., 2004). This method is very useful and easy to implement on fixed and simple domains but it is significantly more complicated to incorporate an evolving

domain and there are often problems with a moving boundary.

Phase Field methods are useful to study the interface between two materials with differing characteristics or "phases" thus it is natural to apply this to the inside and outside of a cell. The technique involves taking distinct values in the two phases, for example 1 and -1, and a smooth change between these two values in a width around the interface. This allows the problem to be solved on the whole system without explicit conditions on the interface. Blazakis (2015) used a phase-field framework to fit a model of a cell membrane derived form physical principles to experimental image data. Additionally, the method has been used to understand deformation due to elastic bending in for example Du et al. (2006), and closer to our problem, Shao et al. (2012) also consider protrusion and contraction forces.

BEM are a way to solve PDEs which have been formulated as integral equations. It is computationally efficient for linear problems where the surface is small in comparison to the volume. This boundary integral method has been used to investigate elastic properties when considering the micropipette aspiration contact problem (Haider and Guilak, 2002). Our problem is inhomogenous and non-linear so this approach is not appropriate.

A technique to deal with the complex deforming boundary has been developed from computational fluid dynamics: The immersed boundary method can model the cell as a force field immersed in fluid domain (Peskin, 2002; Bottino and Fauci, 1998). The previously mentioned paper by Campbell and Bagchi (2018) combined this with surface finite elements, finite volumes and a spectral method, to present a 3D model of amoeboid cell motility with obstacles. This means the model includes solid and fluid mechanics, and pattern formation.

Level set methods are used extensively in cell simulations and are useful when cells split and reconnect, therefore, it may be advantageous to use this method in the future when considering cell proliferation (cell division) and apoptosis (cell death) (Yang et al., 2017). In this thesis we are not concerned with cells splitting.

The finite element method is well known to easily handle complex and evolving cellular domains and can be generalised to multidimensions with little complication, hence is the ideal method to numerically solve our model system. In addition to the most recent incarnation of this model (George, 2012), finite element methods have been widely used to model cell motility (Bottino et al., 2002; Rubinstein et al., 2005; Gladilin et al., 2007; Elliott et al., 2012; Chen et al., 2012; Tozluoğlu et al., 2013; Sakamoto et al., 2014; Blazakis, 2015; MacDonald et al., 2016; Manhart et al., 2017), and can be implemented in diverse

ways depending on the model. For example, Rubinstein et al. (2005) propose a multiscale 2D model considering both an elastic network, and concentrations and orientation of actin and myosin. Sakamoto et al. (2014) also use it in 2D to model the biomechanical properties, in a hyperviscoelastic model, to find the velocity at each time step. Elliott et al. (2012) focus on evolving surface finite elements. MacDonald et al. (2016) develop a moving finite element method on coupled meshes of the bulk and surface to model the interaction of a cell with a chemotactic field. Katti and Katti (2017) study the mechanics of a cancer cell by separately modelling various elements, including cytoskeletal filaments, cytoplasm, membrane and the nucleus, with different elastic moduli. This estimated the force-displacement response of the cell. They see very small displacements and inelastic behaviour.

1.6 The finite element method

Given the considerations of the previous section, we employ the moving grid finite element method (Baines, 1994; Madzvamuse et al., 2003; Madzvamuse, 2006; Madzvamuse and George, 2013) to compute approximate numerical solutions to the mechanobiochemical models studied. The details of the finite element methodology, which is used to obtain the numerical solutions in Chapters 2, 3 and 4, is described in Appendix A.

In this section, as an introduction, we briefly discuss the concept and motivation behind the widely successful numerical method known as the finite element method.

The finite element method began with Galerkin and the concept of a collection of trial functions (also known as test, or later shape, functions). Combinations of these functions are then chosen to be close to the function to be approximated. Thus, the problem becomes that of finding the appropriate amounts of each function. This means solving many, very small equations. The idea was then developed in the seminal work of Courant (1943) to have many more but simpler functions and this was made possible for computer simulations.

The finite element discretisation transforms the partial differential equation into a system of algebraic equations to be solved to find an approximate solution of the continuous problem. A *finite element mesh* is a polygonal or polyhedral mesh that approximates a geometric domain. The mesh is made up of many parts called *elements* with no gaps. Elements are joined together by discrete *nodes*. *Shape functions* describe how a variable can vary inside an element. They are usually low order polynomials which interpolate the solution between the values at the nodes. A shape function equals one at its related node

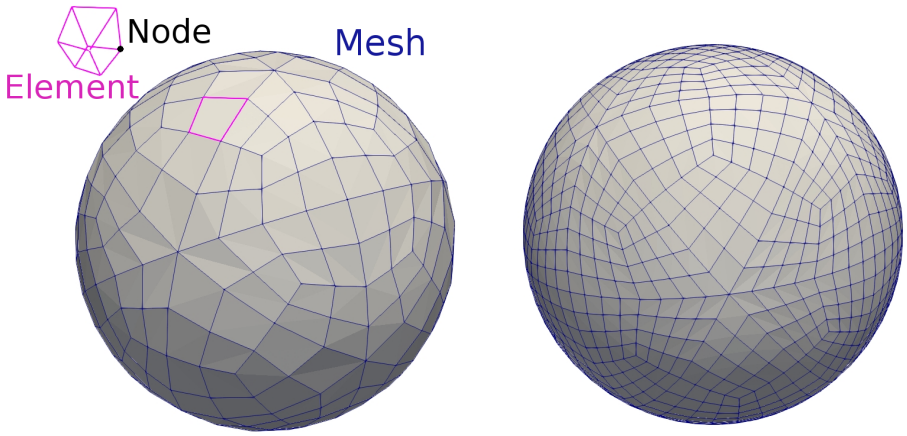

(a) (b)

Figure 1.5: Representations of our mesh. The second, on which we perform most simulations is a refined version of the first, each element has been split into eight new elements and the boundary has been appropriately modified.

and is zero at all others and the sum of all shape functions at any point is one. *Degrees of freedom* are unknowns to be found at each node. Each node may have multiple degrees of freedom for example the displacement in each direction.

The domain of our problem is continuously deforming so we use the moving grid finite element method (Baines, 1994; Madzvamuse et al., 2003), this allows the nodes of the computational grid to move. In fact, velocity of the nodes is computed directly from the displacement solutions of the force balance equation. To obtain our finite element approximation we follow the same steps as George (2012), namely:

1. Derive the weak formulation of the equations.
2. Find spatial and temporal discretisations to give a system of algebraic equations.
3. Assemble the element equations.
4. Implement domain velocity and movement.

Since we are now considering three, rather than two dimensions, our system of equations is much bigger and more complex. See Appendix A for full derivations.

1.7 Summary

In this chapter we have given a biological introduction to cells and their movement. We then discussed mathematical models and numerical methods describing cell movement.

The importance of understanding cell motility cannot be underestimated, firstly to understand our existence, and more urgently, because of the medical consequences in oncology and the processes of wound healing. In this section we have given a brief introduction to a typical cell, the complexity of cells, however, cannot be underestimated. One estimate of the number of different proteins in a single cell type was 100,000 (Savage, 2015). Many biologists give descriptions of cell movement which outline the importance of dozens of different proteins whose functions may include signalling, activation or inhibition. A model including everything would be excessively complex, and even if the computing power was sufficient, the results would be impossible to interpret. Thus the mathematician's answer to this is to propose a model which captures some important processes and gives believable, and ideally, useful results.

There is little argument that the two most important proteins are actin and myosin. Actin filaments give the cell structure and are the primary component of protrusions. Meanwhile, myosin attaches to, and pulls on the filaments to induce a contraction. These two concepts, in combination with descriptions of the mechanical properties of the cytoplasm, are the focus of this thesis.

The well studied 2D model of protrusion, adhesion and retraction has proven very useful. However when moving in three dimensions it is observed that the morphology and processes used to move change significantly. Additionally, there are a number of observed modes of migration in 3D and some cells can change their mode depending on their environment. Advances in microscopy means studying cells in 3D is becoming feasible while still technically complex. Correspondingly the advancement in computing power means we can run much larger simulations, so implementing computational models in 3D is less of a burden.

The majority of mathematical models of cell motility are in one, or two dimensions. As computing power increases, more models are considering three dimensions. This allows for more complex behaviour to be observed and is more applicable to what really happens *in vivo*.

Mechanical systems are an intuitive choice for whole cell models because the structural properties of a cell will directly affect their ability to move. In particular, the elasticity of a cell is usually considered, often in combination with viscosity. This makes sense because a cell is neither a solid nor a liquid but displays properties of both. The various stresses can sometimes be measured *in vitro* and perturbations to their environment will lead to movement.

The mechanical forces will be affected by chemicals and proteins in the cell. The presence of some proteins is often prescribed but in reality their concentrations vary. A common solution is some variation of a reaction-diffusion equation (RDE). Many proteins come in different forms, for example, actin alternates between being globular and polymerised into filaments, and myosin can be bound or unbound to actin. Several models include all four of these states. Most models consider at least actin or myosin to be constant and there are few models which have reaction terms between the two. We will explicitly model just actin filaments (F-actin) and bound myosin since these directly affect the forces.

Due to cell movement being such a complex process, the models can rarely be solved exactly. Therefore numerical methods are utilised to produce simulations. Which method is chosen depends on the equations and domain used. Finite differences, finite elements, finite volumes, phase field methods, boundary element methods (BEM), immersed boundary methods and level set methods (LSM) have all been used. We choose the finite element method for its simplicity, and ability to cope with complex and evolving geometries in multidimensions.

1.8 Thesis outline

Reaction-diffusion systems play an important role in our model, and many other cell motility models. These describe the concentrations of actin and myosin. We would like to see patterns developing with areas of high and low concentration since this may cause instability which leads to movement. Therefore, before describing our model of a cell moving, in Chapter 2, we introduce reaction-diffusion systems and a method for finding parameter values which will lead to particular patterns developing.

Our key contributions to the mathematical interpretation of cell motility are the extension of the 2D model of George et al. (2013) into 3D, and the introduction of myosin into the model. In Chapter 3 we introduce and discuss the original model and begin our extension by formulating it in three dimensions. Mechanical forces and actin concentration are modelled. We then add myosin concentration to the model in Chapter 4. The model now consists of a force balance equation and two coupled reaction-diffusion equations. In both of these chapters predictions for behaviour of solutions will be made using linear stability theory.

Since our models are highly non-linear with many parameters, we cannot find solutions analytically, therefore, we choose here to use the finite element method for its efficiency

in dealing with complex nonlinear systems on evolving domains (Johnson, 1987; Reddy, 1993). Numerical simulations are presented in Chapters 3 and 4, and show a wide variety of protrusions and retractions due to, and affecting, the dynamics of actin and/or myosin in the cell. Appendix A details the finite element method used. Finally, we discuss our findings, limitations of the model and possible future directions in Chapter 5.

Chapter 2

Biochemical reaction-diffusion systems on arbitrary stationary 3-dimensional geometries

2.1 Introduction

In his seminal work, Turing (1952) presented an elegant mathematical theory of reaction-diffusion type for pattern formation in developmental biology. He showed that, via a symmetry breaking, a homogeneous steady state which is linearly stable in the absence of diffusion may be driven unstable in the presence of diffusion to give rise to the emergence of a spatially inhomogeneous pattern. This process is now well known as *diffusion-driven instability* or *Turing instability*. Since then, reaction-diffusion systems have been proposed and applied to model many natural phenomena including cancer invasion and angiogenesis in cancer biology (Chaplain et al., 2001; Chaplain, 1995; Gatenby and Gawlinski, 1996), pattern formation in developmental biology (Hunding, 1992; Maini and Solursh, 1991), wound healing in biomedicine (Dale and Maini, 1994; Sherratt et al., 1992), cell motility (Mogilner, 2009; Mogilner and Edelstein-Keshet, 2002b; George, 2012) and material science (Bozzini et al., 2012; Krinsky, 1983), among many others. Despite their numerous applications, Turing's theory of pattern formation has been widely criticised mainly due to the lack of robustness of the model system to changes in the parameters as well as the lack of experimental evidence of the existence of so-called morphogens with varying diffusivities. Only recently has the existence of chemical morphogens been experimentally validated in hair follicle pattern formation by Sick et al. (2006).

Often, we are interested in identifying parameters which will lead to a particular pat-

tern. Our approach, which is the basis of this chapter, is to compute eigenpairs of the Laplacian on a variety of domains and use linear stability analysis to determine parameter values for the system that will lead to spatially inhomogeneous steady states whose patterns correspond to particular eigenfunctions. This method has previously been used on domains and surfaces where the eigenvalues and eigenfunctions are found analytically in closed form (Madzvamuse, 2000; Chaplain, 1995). Our extension of this methodology considers arbitrary domains and surfaces on which we numerically compute eigenpairs.

The remainder of this chapter is structured as follows. In Section 2.3 we introduce the mathematical model which we study in this work. We derive the necessary and sufficient conditions for Turing *diffusion-driven instability* in Section 2.4. We then detail how mode selection and parameter identification are carried out. In Sections 2.5 and 2.7 we outline the new theoretical and computational framework for mode selection and parameter identification. The numerical implementation is discussed in Section 2.6 and the formulation of the finite element method is described in Section A.1. We then give specific examples in 3-dimensions for regular (by which we mean domains on which analytic expressions for the eigenfunctions are available) as well as general domains and surfaces (where no analytical solutions exist). Our first example is the sphere, this is where we go into most detail. In later chapters, we will perform mode isolation of a more complex system on the sphere since this will be the assumed initial shape of a cell. We discuss the implications of our framework in the context of current methodologies and conclude that given a biological pattern and a reaction-diffusion system, our approach provides a useful tool for estimating parameter values which may give rise to the observed pattern. The results in this chapter are published in our paper (Murphy et al., 2018) : Laura Murphy, Chandrasekhar Venkataraman, and Anotida Madzvamuse. Parameter identification through mode isolation for reaction–diffusion systems on arbitrary geometries. *International Journal of Biomathematics*, 16(4):1850053, 2018. (A.M. conceived the idea, L.M. performed the analysis and computations supervised by A.M. and C.V., article was written by L.M. with input from A.M. and C.V.)

2.2 Mathematical preliminaries

2.2.1 Bessel's equation and Bessel Functions

We will need Bessel functions when solving the eigenvalue problem on the sphere in Section 2.8.1. The solutions to Bessel's equation are well known and we will give an outline of the

solutions (Bessel functions) which can be found using the method of Frobenius (Zill and Cullen, 2000; Arfken et al., 2013). Before introducing the problem, we define a regular singular point and Frobenius' theorem.

Definition 2.2.1. *(Regular Singular Point)* Consider the ODE

$$y'' + P(x)y' + Q(x)y = 0. \tag{2.1}$$

If $P(x)$ and $Q(x)$ remain finite at $x = x_0$, then x_0 is called an *ordinary point*. If either $P(x)$ or $Q(x)$ diverges as $x \to x_0$, then x_0 is called a **s**ingular point. If either $P(x)$ or $Q(x)$ diverges as $x \to x_0$ but $(x - x_0)P(x)$ and $(x - x_0)^2 Q(x)$ remain finite, then x_0 is a *regular singular point*.

Theorem 1. *(Frobenius' Theorem)* If an ODE has a regular singular point at $x = x_0$ then, by Frobenius theorem, there exists at least one solution of the form

$$y = \sum_{n=0}^{\infty} c_n (x - x_0)^{n+\kappa}. \tag{2.2}$$

Where κ is a constant to be determined. The series will converge on at least some interval $0 < x - x_0 < R$. (Zill and Cullen, 2000).

Bessel's Equation

The Bessel equation is:

$$x^2 y'' + xy' + (x^2 - \alpha^2)y = 0. \tag{2.3}$$

The origin is a regular singular point of this equation so there is at least one solution of the form $y = x^\kappa \sum_{n=0}^{\infty} c_n x^n$. Inputting this into (2.3) we obtain

$$\begin{aligned} x^2 y'' + xy' + (x^2 - \alpha^2)y = &\sum_{n=0}^{\infty} c_n (n+\kappa)(n+\kappa-1)x^{n+\kappa} + \sum_{n=0}^{\infty} c_n (n+\kappa)x^{n+\kappa} \\ &+ \sum_{n=0}^{\infty} c_n x^{n+\kappa+2} - \alpha^2 \sum_{n=0}^{\infty} c_n x^{n+\kappa} = 0, \end{aligned} \tag{2.4}$$

which simplifies to

$$c_0(\kappa^2 - \alpha^2) + c_1((\kappa+1)^2 - \alpha^2)x + \sum_{n=2}^{\infty} [c_n((n+\kappa)^2 - \alpha^2) + c_{n-2}]x^n = 0. \tag{2.5}$$

We cannot have that $c_0 = 0$ because that would lead to the trivial solution but the first term must be zero, therefore κ satisfies $\kappa^2 - \alpha^2 = 0$. Therefore $\kappa = \pm\alpha$, so first considering $\kappa = \alpha > 0$, which gives

$$c_1(2\alpha + 1)x + \sum_{n=2}^{\infty} [c_n((n+\alpha)^2 - \alpha^2) + c_{n-2}]x^n = 0. \tag{2.6}$$

We must have that each coefficient of power of x is equal to zero, i.e.

$$c_1(2\alpha+1)=0, \tag{2.7a}$$

$$c_n((n+\alpha)^2-\alpha^2)+c_{n-2}=0, \quad n=2,3,\dots . \tag{2.7b}$$

So from (2.7a) we infer $c_1=0$ and $c_n=\frac{-c_{n-2}}{n(n+2\alpha)},\ n=2,3,\dots$ combining these two leads to see that $c_3=c_5=c_7\dots=0$. Then we can choose $n=2k,\ k=1,2,3,\dots$ and deduce that

$$c_{2k}=\frac{-1}{2^2k(k+\alpha)}c_{2k-2}. \tag{2.8}$$

So this c_{2k} can be written in terms of c_0 (this can be seen by writing out c_2, c_4, c_6, etc.)

$$c_{2k}=\frac{(-1)^k\alpha!}{2^{2k}k!(k+\alpha)!}c_0. \tag{2.9}$$

Let

$$c_0=\frac{1}{2^\alpha\Gamma(1+\alpha)}=\frac{1}{2^\alpha\alpha!},$$

to give:

$$c_{2k}=\frac{(-1)^k\alpha!}{2^{2k}k!(k+\alpha)!}\frac{1}{2^\alpha\alpha!}=\frac{(-1)^k}{2^{2k+\alpha}k!\Gamma(1+k+\alpha)}.$$

So one solution is

$$y=\sum_{k=0}^{\infty}c_{2k}x^{2k+\alpha}=\sum_{k=0}^{\infty}\frac{(-1)^k}{k!\Gamma(1+k+\alpha)}\left(\frac{x}{2}\right)^{2k+\alpha}=:J_\alpha(x).$$

Similarly for the second root $\kappa=-\alpha$ gives the solution:

$$y=\sum_{k=0}^{\infty}\frac{(-1)^k}{k!\Gamma(1+k-\alpha)}\left(\frac{x}{2}\right)^{2k-\alpha}=:J_{-\alpha}(x). \tag{2.10}$$

Bessel Functions of the First Kind

$J_\alpha(x)$ and $J_{-\alpha}(x)$ are called Bessel functions of the first kind. If α is not an integer, these functions are linearly independent, so are distinct solutions of Bessel's equation and the general solution would be

$$y=c_1J_\alpha(x)+c_2J_{-\alpha}(x).$$

However if $\alpha\in\mathbb{Z}$ then $J_\alpha(x)=(-1)^\alpha J_{-\alpha}(x)$ so they are not linearly independent.

Bessel Functions of the Second Kind

If $\alpha\notin\mathbb{Z}$ then we can define:

$$Y_\alpha(x)=\frac{\cos(\alpha\pi)J_\alpha(x)-J_{-\alpha}(x)}{\sin(\alpha\pi)}. \tag{2.11}$$

This allows us to define solutions that have singularities at zero.

2.2.2 Spaces and norms

We introduce the spaces and norms that will be used in formulating the approximation of the model problem. For $1 \leq p < \infty$, we define the Banach space for $\mathbf{\Omega}_t \subset \mathbb{R}^3$

$$L^p(\mathbf{\Omega}_t) = \left\{ v(\boldsymbol{x},t) \text{ a measurable function: } \int_{\mathbf{\Omega}_t} |v(\boldsymbol{x},t)|^p d\mathbf{\Omega}_t < \infty \text{ for } \boldsymbol{x} \in \mathbf{\Omega}_t, t \in I \right\},$$

and its norm $||v(\boldsymbol{x},t)||_{L^p(\mathbf{\Omega}_t)} = \left(\int_{\mathbf{\Omega}_t} |v(\boldsymbol{x},t)|^p d\mathbf{\Omega}_t \right)^{\frac{1}{p}}$. We also define the Hilbert space

$$H^1(\mathbf{\Omega}_t) = \left\{ v(\boldsymbol{x},t) \in L^2(\mathbf{\Omega}_t), D^{\boldsymbol{\alpha}} v \in L^2(\mathbf{\Omega}_t), |\boldsymbol{\alpha}| \leq 1 \text{ for } \boldsymbol{x} \in \mathbf{\Omega}_t, t \in I \right\},$$

where $\boldsymbol{\alpha} = (\alpha_1, \alpha_2, \alpha_3)$, $|\boldsymbol{\alpha}| = \alpha_1 + \alpha_2 + \alpha_3$ and D^α represents the distributional derivative at every time $t \in I$

$$D^\alpha v = \frac{\partial^{|\boldsymbol{\alpha}|} v}{\partial^{\alpha_1} x \partial^{\alpha_2} y \partial^{\alpha_3} z}.$$

2.3 Mathematical modelling framework

In order to illustrate with clarity the novelty of our approach, we will introduce the standard theoretical framework for reaction-diffusion systems in multi-dimensions (Murray, 2003). First we will outline how a reaction-diffusion equation can be derived.

2.3.1 Derivation of a reaction-diffusion equation

Let $\Omega \subset \mathbb{R}^n$ $(n = 1, 2, 3)$ be a simply connected bounded stationary domain for all time and $\partial\Omega$ be the boundary enclosing Ω. Also let $a(\boldsymbol{x},t)$ and $m(\boldsymbol{x},t)$ be two chemical concentrations at position $\boldsymbol{x} \in \Omega \subset \mathbb{R}^n$ and times $t \in I$. To define the equation we consider the flux $\mathbf{J}(\boldsymbol{x}(t),t) \in C^1(\Omega)$. This is the amount of a which passes the across boundary. The conservation equation tells us that the rate of change of the total amount of a material in a volume is equal to the flux through (normal to) the boundary plus the net formation of the material within the domain. Hence we can write the conservation of material as follows

$$\frac{\partial}{\partial t} \int_\Omega a \, d\Omega = - \int_{\partial\Omega} \mathbf{J} \cdot \mathbf{n} \, d\mathbf{S} + \int_\Omega f(a,m) \, d\Omega, \tag{2.12}$$

where $\mathbf{n}$ is the unit normal to the boundary $\partial\Omega$ and $f(a,m)$ is the net formation of a due to the chemical concentrations, a and m. Using the divergence theorem on the boundary integral leads to

$$\frac{\partial}{\partial t} \int_\Omega a \, d\Omega = \int_\Omega (-\nabla \cdot \mathbf{J} + f(a,m)) \, d\Omega. \tag{2.13}$$

Next, we assume classical diffusion, i.e. that a substance moves from high to low concentration at a magnitude proportional to the concentration gradient. Thus we use Fick's law of mass diffusion, which states that $\mathbf{J} = -D_a \nabla a$, where D_a is a positive constant diffusion coefficient and Δ denotes the usual Cartesian Laplace operator. Hence:

$$\int_\Omega \Big(\frac{\partial a}{\partial t} - D_a \Delta a - f(a,m) \Big) d\Omega = 0. \tag{2.14}$$

Since this holds for any arbitrary domain and the integrand is continuous we have:

$$\frac{\partial a}{\partial t} - D_a \Delta a = f(a,m) \text{ for } \boldsymbol{x} \in \Omega,\ t \in I. \tag{2.15}$$

The same argument can be made for $m(\boldsymbol{x}, t)$ with corresponding diffusion coefficient D_m and reaction term $g(a,m)$. In fact, we can generalise to many species as was described in Equation (1.1), in Section 1.4.2.

2.3.2 Theoretical framework

We consider the standard two component dimensional system

$$\begin{cases} \begin{cases} a_t = D_a \Delta a + f(a,m), \\ m_t = D_m \Delta m + g(a,m), \end{cases} & \boldsymbol{x} \in \Omega,\ t > 0, \\ \mathbf{n} \cdot \nabla a = \mathbf{n} \cdot \nabla m = 0, & \boldsymbol{x} \in \partial\Omega,\ t \geq 0, \\ a(\boldsymbol{x}, 0) = a_0(\boldsymbol{x}), \quad \text{and} \quad m(\boldsymbol{x}, 0) = m_0(\boldsymbol{x}), & \boldsymbol{x} \in \Omega,\ t = 0, \end{cases} \tag{2.16}$$

where $D_a > 0$ and $D_m > 0$ are diffusion coefficients and initial conditions are prescribed through non-negative bounded functions $a_0(\boldsymbol{x})$ and $m_0(\boldsymbol{x})$. In the above, $f(a,m)$ and $g(a,m)$ represent nonlinear reactions. We have zero flux boundary conditions (homogeneous Neumann) because we want only internal sources of instability, i.e. self-organisation of the system. However, our same procedure may be adapted to use Dirichlet or mixed conditions.

In the case where the domain is a surface, the Laplace operator is replaced by the Laplace-Beltrami operator Δ_Γ, where Γ is the (smooth) surface. Surface gradients are also employed. This can be described as follows (for further details we refer the interested reader to see Dziuk and Elliott (2013)). If $f : \Gamma \to \mathbb{R}$ is differentiable at $\boldsymbol{x} \in \Gamma$ we can define the *tangential gradient* of f at $\boldsymbol{x} \in \Gamma$ by

$$\nabla_\Gamma f = \nabla \bar{f} - \nabla \bar{f} \cdot \mathbf{n}\mathbf{n}. \tag{2.17}$$

Here $\bar{f}$ is a smooth extension of $f : \Gamma \to \mathbb{R}$ to an $(n+1)$-dimensional neighbourhood U of the surface Γ, so that $\bar{f}|_\Gamma = f$. ∇ is the gradient in $\mathbb{R}^{n+1}$ and $\mathbf{n}$ is the unit normal. The

Laplace-Beltrami operator applied to a twice differentiable function $f \in C^2(\Gamma)$ is given by

$$\Delta_\Gamma f = \nabla_\Gamma \cdot \nabla_\Gamma f. \tag{2.18}$$

It must be observed that if the surface does not have a boundary, no boundary conditions are needed. If the surface has a boundary, we assume homogeneous Neumann boundary conditions.

Since the reaction terms are nonlinear, analytical solutions cannot normally be obtained. Therefore we investigate solution behaviour using linear stability theory and numerical methods. Linear stability analysis is one way of determining the behaviour of a nonlinear system near a given stationary point, normally a uniform steady state, of the given system. The idea is to find under what conditions on the nonlinear reaction kinetics is the uniform steady state linearly asymptotically stable in the absence of diffusion. When diffusion is introduced, the uniform steady state is driven unstable in what is now known as the process of *diffusion-driven instability* with the system converging to a spatially inhomogeneous steady state, thereby giving rise to patterning (Murray, 2003; Turing, 1952). The mathematical treatment of the derivation of the necessary conditions for *diffusion-driven* instability requires solving the well known eigenvalue problem, with W a solution of

$$\Delta W + k^2 W = 0, \quad \boldsymbol{x} \in \Omega, \tag{2.19a}$$

$$(\mathbf{n} \cdot \nabla) W = 0, \quad \boldsymbol{x} \in \partial\Omega, \tag{2.19b}$$

where the solution pairs (k (eigenvalues), $W_k(\boldsymbol{x})$ (eigenfunctions) are obtained either analytically on certain spatial domains or numerically for the general case) of this equation can be compared to the spatially inhomogeneous steady state solutions of (2.16), with good agreement expected near primary bifurcation points.

This approach is generally called mode isolation. The most famous exploration of this problem is the celebrated article "Can one hear the shape of the drum?" by Mark Kac (1966). The posed question is, if one knows all the eigenvalues of the eigenvalue problem is it possible to determine the domain? It was later proven by Gordon et al. (1992) that the answer is no and they gave examples of distinct regions with identical eigenvalues.

Other work concerned with mode isolation and linear stability theory for reaction-diffusion systems can be found in Chaplain et al. (2001) and Madzvamuse (2000), here the validation has been mainly restricted to special domains and volumes where the eigenvalue problem can be solved analytically. In this chapter we will depart from this framework, instead we will compute approximations of the eigenpairs on arbitrary, simply connected

domains, volumes and surfaces. We then use these eigenvalues to calculate, by use of the Turing-parameter space restrictions, appropriate model parameter values. This approach can be thought to be analogous to an inverse parameter identification approach whereby, given the eigenvalues and eigenfunctions solving the eigenvalue problem (2.19), find model parameter values that would give rise to an inhomogeneous spatially varying solution similar to that exhibited by the eigenfunction. To confirm numerical predictions, we use the computed model parameter values to solve the full nonlinear reaction-diffusion systems and compare approximated eigenfunctions on these arbitrary domains, volumes and surfaces to the spatially inhomogeneous solutions obtained numerically.

To proceed, next we show the two-component form which we will work with and derive the conditions for *diffusion-driven* instability. These will help us to isolate particular modes.

2.4 Conditions for diffusion-driven instability for reaction-diffusion systems

All two component reaction-diffusion systems of the form (2.16) can be non-dimensionalised and scaled to take the form

$$a_t = \gamma f(a,m) + \Delta a, \quad m_t = \gamma g(a,m) + d\Delta m, \quad \boldsymbol{x} \in \Omega \subset \mathbb{R}^n,\ t \in [0,\infty], \tag{2.20a}$$

$$(\mathbf{n}\cdot\nabla)\begin{pmatrix} a \\ m \end{pmatrix} = 0 \quad \boldsymbol{x} \in \partial\Omega\ t \in [0,\infty], \tag{2.20b}$$

$$a(\boldsymbol{x},0),\ m(\boldsymbol{x},0) \text{ given}, \tag{2.20c}$$

where $a = a(\boldsymbol{x},t), m = m(\boldsymbol{x},t)$, d is the ratio of diffusion coefficients, $f(a,m)$ and $g(a,m)$ describe the non-dimensionalised reaction kinetics. For simplicity, we assume that f and g are continuously differentiable, γ can be described as the relative strength of the reaction terms or alternatively as proportional to the domain size. A uniform steady state (a_s, m_s) is a fixed point where $(a,m) = (a_s, m_s)$, constant in time and space, satisfies (2.20). We can find the steady state by solving $f(a_s, m_s) = g(a_s, m_s) = 0$.

The conditions for instability due to diffusion are well known and we recall the method here (Murray, 2003). Linear stability begins by considering a small spatial perturbation from the steady state (a_s, m_s). We will then examine the behaviour as $t \to \infty$. We define the perturbation as

$$\varepsilon\hat{a}(\boldsymbol{x},t) = a(\boldsymbol{x},t) - a_s, \quad \varepsilon\hat{m}(\boldsymbol{x},t) = m(\boldsymbol{x},t) - m_s, \quad |\varepsilon| << 1. \tag{2.21}$$

2.4.1 Stability without diffusion

The first objective is finding the conditions for stability without diffusion. Inputting (2.21) into the system $a_t = \gamma f(a,m),\ m_t = \gamma g(a,m)$ and discarding higher order terms, we obtain

$$\varepsilon \hat{a}_t = \gamma(\varepsilon \hat{a} f_a(a_s, m_s) + \varepsilon \hat{m} f_m(a_s, m_s)), \tag{2.22a}$$

$$\varepsilon \hat{m}_t = \gamma(\varepsilon \hat{a} g_a(a_s, m_s) + \varepsilon \hat{m} g_m(a_s, m_s)). \tag{2.22b}$$

εs cancel and the system can be written in matrix-vector form

$$\mathbf{w}_t = \gamma \mathbf{A} \mathbf{w}, \tag{2.23}$$

where

$$\mathbf{w} = \begin{pmatrix} \hat{a} \\ \hat{m} \end{pmatrix} \text{ and } \mathbf{A} = \begin{pmatrix} f_a & f_m \\ g_a & g_m \end{pmatrix}_{a_s, m_s} \text{ (this is the stability matrix).} \tag{2.24}$$

Let λ be an eigenvalue of $\mathbf{A}$, then solutions are of the form $\mathbf{w} = \mathbf{b}e^{\lambda t}$, where $\mathbf{b}$ is a constant vector. If $\mathrm{Re}(\lambda) < 0$ then $\mathbf{w} \to 0$ as $t \to \infty$. In other words, since $\mathbf{w}$ is a perturbation from the steady state, $\mathrm{Re}(\lambda) < 0$ means that the steady state is linearly stable. Thus, to proceed, we find the eigenvalues of $\mathbf{A}$ as follows

$$|\mathbf{A} - \lambda \mathbf{I}| = \begin{vmatrix} f_a - \lambda & f_m \\ g_a & g_m - \lambda \end{vmatrix} = 0 \tag{2.25a}$$

$$\implies \lambda_1, \lambda_2 = \frac{1}{2}\left\{ f_a + g_m \pm \sqrt{(f_a + g_m)^2 - 4(f_a g_m - f_m g_a)} \right\}, \tag{2.25b}$$

where f_a, f_m, g_a and g_m are evaluated at (a_s, m_s). We consider the first eigenvalue

$$\lambda_1 = \frac{1}{2}\left\{ f_a + g_m - \sqrt{(f_a + g_m)^2 - 4(f_a g_m - f_m g_a)} \right\}, \tag{2.26}$$

and see that, for $Re(\lambda_1) < 0$, it is a sufficient condition that $f_a + g_m < 0$. We also want $Re(\lambda_2) < 0$ so we also need

$$\begin{aligned} & f_a + g_m + \sqrt{(f_a + g_m)^2 - 4(f_a g_m - f_m g_a)} < 0 \\ \iff\ & f_a g_m - f_m g_a > 0. \end{aligned}$$

Therefore, in the absence of diffusion, the steady state (a_s, m_s) is linearly stable if and only if the partial derivatives of f and g at (a_s, m_s) satisfy

$$f_a + g_m < 0 \text{ and } f_a g_m - f_m g_a > 0. \tag{2.28}$$

2.4.2 Instability due to diffusion

Now considering the full system (2.20) with perturbation (2.21) we obtain

$$\mathbf{w}_t = \gamma \mathbf{A}\mathbf{w} + \mathbf{D}\nabla^2 \mathbf{w}, \text{ where } \mathbf{D} = \begin{pmatrix} 1 & 0 \\ 0 & d \end{pmatrix}. \tag{2.29}$$

To solve this, we let $\mathbf{W}(\boldsymbol{x})$ be a time-independent solution of

$$\nabla^2 \mathbf{W} + k^2 \mathbf{W} = 0 \quad \boldsymbol{x} \in \Omega,$$
$$(\mathbf{n} \cdot \nabla)\mathbf{W} = 0 \quad \boldsymbol{x} \in \partial\Omega.$$

$\mathbf{W}_k(\boldsymbol{x})$ is the eigenfunction corresponding to k satisfying boundary conditions. We look for solutions of (2.29) of the form:

$$\mathbf{w}(\boldsymbol{x}, t) = \sum_k c_k e^{\lambda t} \mathbf{W}_k(\boldsymbol{x}). \tag{2.31}$$

The coefficients c_k are determined by Fourier expansion when $t = 0$. For each k, substituting $\mathbf{w}(\boldsymbol{x}, t) = c_k e^{\lambda t}\mathbf{W}_k(\boldsymbol{x})$ and its derivatives into (2.29) gives

$$\lambda e^{\lambda t}\mathbf{W}_k(\boldsymbol{x}) = \gamma \mathbf{A} e^{\lambda t}\mathbf{W}_k(\boldsymbol{x}) - \mathbf{D}k^2 e^{\lambda t}\mathbf{W}_k(\boldsymbol{x})$$
$$\implies \lambda \mathbf{W}_k = \gamma \mathbf{A}\mathbf{W}_k - \mathbf{D}k^2 \mathbf{W}_k.$$

This is true if $\mathbf{W}_k = 0$ (which is trivial) or $|\lambda \mathbf{I} - \gamma \mathbf{A} + \mathbf{D}k^2| = 0$, i.e.

$$\left| \lambda \begin{pmatrix} 1 & 0 \\ 0 & 1 \end{pmatrix} - \gamma \begin{pmatrix} f_a & f_m \\ g_a & g_m \end{pmatrix} + \begin{pmatrix} 1 & 0 \\ 0 & d \end{pmatrix} k^2 \right| = 0, \tag{2.33}$$

which becomes the dispersal relation

$$\lambda^2 + b(k^2)\lambda + c(k^2) = 0,$$
$$\text{where } \begin{cases} b(k^2) = k^2(1+d) - \gamma(f_a + g_m), \\ c(k^2) = dk^4 - \gamma(df_a + g_m)k^2 + \gamma^2(f_a g_m - f_m g_a). \end{cases} \tag{2.34}$$

For instability we need the real part of at least one root of this polynomial to be positive. We know that $b(k^2) > 0$ because in the previous section we imposed that $f_a + g_m < 0$, and $k^2, d > 0$. Therefore $Re(\lambda_1) = \frac{1}{2}\{-b(k^2) - \sqrt{(b(k^2))^2 - 4c(k^2)}\} < 0$. Then considering the second root

$$Re(\lambda_2) = \frac{1}{2}\{-b(k^2) + \sqrt{(b(k^2))^2 - 4c(k^2)}\} > 0$$
$$\implies c(k^2) = dk^4 - \gamma(df_a + g_m)k^2 + \gamma^2(f_a g_m - f_m g_a) < 0.$$

Since dk^4 and $\gamma^2(f_a g_m - f_m g_a)$ are positive we need $(df_a + g_m) > 0$. This is a necessary but not sufficient condition. We now must consider if

$$c(k^2) = d(k^2)^2 - \gamma(df_a + g_m)k^2 + \gamma^2(f_a g_m - f_m g_a) < 0, \tag{2.36}$$

to ensure $\mathrm{Re}(\lambda_2) > 0$. We differentiate twice to find the value of k^2 at the turning point and determine if it is a minimum

$$\frac{\partial c}{\partial (k^2)} = 2d(k^2) - \gamma(df_a + g_m) = 0 \implies k^2 = \frac{\gamma(df_a + g_m)}{2d} \text{ is a turning point,} \tag{2.37a}$$

$$\frac{\partial^2 c}{\partial (k^2)^2} = 2d > 0 \implies \text{ it is a minimum.} \tag{2.37b}$$

The minimum of $c(k^2)$ is the value at this turning point

$$\begin{aligned} c(k^2)_{min} &= c\left(\frac{\lambda(df_a + g_m)}{2d}\right) \\ &= \gamma^2\left[\frac{1}{4d}(df_a + g_m)^2 - \frac{1}{2d}(df_a + g_m)^2 + f_a g_m - f_m g_a\right] \\ &= \gamma^2\left[-\frac{1}{4d}(df_a + g_m)^2 + |\mathbf{A}|\right]. \end{aligned} \tag{2.38}$$

For c_{min} to be negative for some $k \neq 0$ we require

$$\begin{aligned} \frac{(df_a + g_m)^2}{4d} &> |\mathbf{A}| \\ &\iff (df_a + g_m)^2 - 4d(f_a g_m - f_m g_a) > 0. \end{aligned} \tag{2.39}$$

This is the final condition for instability with diffusion.

Qualitative solutions of the dispersal relation change at $c_{min} = 0$, or

$$(df_a + g_m)^2 = 4d(f_a g_m - f_m g_a).$$

So we can define a critical diffusion coefficient ratio d_c as the root of

$$d_c^2 f_a^2 + 2(2f_m g_a - f_a g_m)d_c + g_m^2 = 0, \tag{2.40}$$

and define a critical wave number

$$k_c^2 = \gamma\frac{d_c f_a + g_m}{2d_c} = \gamma\sqrt{\frac{f_a g_m - f_m g_a}{d_c}}.$$

The roots of $c(k^2) = 0$ (2.34) give the range of k^2 that mean instability for certain d. These roots are

$$k_\pm^2 = \gamma\frac{(df_a + g_m) \pm \sqrt{(df_a + g_m)^2 - 4d(f_a g_m - f_m g_a)}}{2d}. \tag{2.41}$$

Therefore we conclude that instability will occur if

$$df_a + g_m > 0, \qquad (df_a + g_m)^2 - 4d(f_a g_m - f_m g_a) > 0 \tag{2.42}$$

and k^2 lies in the range $k_-^2 < k^2 < k_+^2$ from equation (2.41).

We exploit this range to isolate particular patterns/modes. The unstable modes will correspond to the eigenfunctions of the Laplacian (or Laplace-Beltrami) on the chosen domain or surface with the selected boundary conditions and k^2 the associated eigenvalues. The effect of varying d and γ on (2.34) is shown in Figure 2.1 on page 41.

In summary the necessary conditions for diffusion-driven instability are

$$f_a + g_m < 0, \qquad f_a g_m - f_m g_a > 0, \tag{2.43a}$$

$$df_a + g_m > 0, \qquad (df_a + g_m)^2 - 4d(f_a g_m - f_m g_a) > 0. \tag{2.43b}$$

Additionally, the sufficient conditions for patterning formation are that one must be able to isolate distinct real wave numbers and that the domain must be large enough (Madzvamuse et al., 2010, 2015; Murray, 2003).

2.4.3 Examples of reaction kinetics

For illustrative purposes, we consider three classical reaction kinetics as summarised below. The work presented in this chapter holds true for other similar reaction kinetics capable of generating Turing patterns. In later chapters we will introduce similar equations for proteins in a cell.

Schnakenberg or activator-depleted substrate kinetics

The Schnakenberg kinetics (Schnakenberg, 1979) are a condensed version of the well documented Brusselator model describing a series of autocatalytic reactions also known as activator-depleted models (Gierer and Meinhardt, 1972; Prigogine and Lefever, 1968), and these are characterised by

$$A \rightleftharpoons X \qquad B + X \to Y + D \qquad 2X + Y \to 3X. \tag{2.44}$$

If a and m are the concentrations of X and Y respectively, using the law of mass action and the non-dimensionalisation of f and g, within system (2.20), we obtain that

$$f(a, m) = c - a + a^2 m \quad \text{and} \quad g(a, m) = b - a^2 m, \tag{2.45}$$

where c and b are positive parameters.

Gierer-Meinhart kinetics

One of the models proposed by Gierer and Meinhardt (1972) describes a system whereby an "activator" activates the production of an "inhibitor" which inhibits the production of

the activator. Again the non-dimensionalised form can be obtained

$$f(a,m) = c - ba + \frac{a^2}{m(1+ka^2)}, \quad \text{and} \quad g(a,m) = a^2 - m, \tag{2.46}$$

where c and b are positive parameters (representing constant production rate and linear degradation respectively) and k can be thought of as the saturation concentration of a.

Thomas kinetics

The Thomas model (Thomas and Kernevez, 1976) is an immobilised-enzyme substrate-inhibition mechanism which can be written in non-dimensional form as

$$f(a,m) = c - a - \frac{\rho am}{1+a+Ka^2}, \quad g(a,m) = \alpha b - \alpha m - \frac{\rho am}{1+a+Ka^2}, \tag{2.47}$$

where c, ρ, K, α, β are all non-negative parameters. This can be interpreted as in Murray (1982) by saying that a and m: (i) are generated by constant production a and αb respectively, (ii) decay linearly proportional to a and αm respectively and (iii) are used up in a substrate inhibition manner $\frac{\rho av}{1+a+Ka^2}$.

We have presented forms that reaction-diffusion equations can take, and the conditions for patterns to occur. These patterns are called modes and relate to the wavenumber k^2. This means we are now in a position to ask how we can identify parameters in order for a particular pattern to appear (or, in other words, which parameters cause particular modes to be isolated)?

2.5 Parameter identification through mode isolation for reaction-diffusion systems on 3-D geometries

To-date mode selection and parameter identification for reaction-diffusion systems have been mainly carried out on regular planar domains and surfaces where the eigenvalue problem can be analytically solved to yield analytical forms of the wave numbers as well as their corresponding eigenfunctions (Madzvamuse, 2000; Madzvamuse et al., 2003; George, 2012). Here, we will depart from this framework and extend computationally mode selection and parameter identification to include arbitrary domains and stationary surfaces. First, we will solve the eigenvalue problem numerically using finite elements on planar domains or surface finite elements on smooth surfaces, respectively, to obtain the eigenmodes and their corresponding eigenfunctions. Here, we employ the Krylov-Schur algorithm (Stewart, 2002) for solving the resulting algebraic system arising from the finite

element discretisation. Second, we then pick an eigenmode to which we apply the necessary and sufficient conditions for Turing diffusion-driven instability in order to isolate reaction-kinetic model parameter values within a reaction-diffusion system. This process can be loosely thought of as an inverse problem for model parameter identification. Once the parameter values are isolated, the full reaction-diffusion system is then solved with these isolated parameter values to obtain an inhomogeneous spatially varying solution which is then compared to the numerically computed eigenfunction on the domain or surface. Alternatively, one could pose the following problem to which this methodology will provide insightful information which is otherwise out of reach with the current methodology: *Given a biological pattern on a domain or surface and a plausible reaction-diffusion system, what are the model parameter values within this reaction-diffusion system that will give rise to the observed pattern?* This chapter provides a theoretical and computational framework to answer such a question. A recent article by Dhillon et al. (2017) uses a similar approach to model pattern development and presents a multiresolution algorithm for tracing bifurcation branches.

It must be observed that the eigenvalue problem and the reaction-diffusion system are both solved by a similar numerical method, the finite element method in multi-dimensions (Johnson, 1987). The finite element method is well known for its capability to deal with complex irregular geometries (Barreira et al., 2011; Elliott et al., 2012; Venkataraman et al., 2011). Alternative numerical methods such as finite differences (Beckett and Mackenzie, 2001), spectral methods (Chaplain et al., 2001; Ruuth, 1995) and finite volume methods among others could be used but with considerable efforts in dealing with geometrical complexities. The finite element method is discussed more extensively in Appendix A. As mentioned above one interpretation of our approach is that it provides a means of estimating parameter values such that the pattern predicted by linear stability analysis is close to a desired pattern. It must be noted that in many cases the steady state pattern may not be an eigenfunction (or a linear combination of the eigenfunctions) of the Laplacian on the given domain. This is since the nonlinear terms play a role in the resultant steady state pattern (Murray, 2003). In such a setting our approach may provide parameters which serve as a suitable initial guess for a more advanced parameter identification algorithm (Croft et al., 2014; Garvie et al., 2010).

The goal of mode isolation is to choose parameters, in our case (d, γ), so that a trajectory starting from a small random perturbation from the steady state will evolve into a spatial pattern generated by one that corresponds, or at least is close to, a chosen eigen-

function of the Laplacian on that domain. Wavenumber isolation of reaction-diffusion systems is described in one dimension, squares and triangles in Madzvamuse (2000). In George (2012) wavenumbers of a visco-elastic model are isolated on the unit disk. We use similar ideas in the present work. The basic steps are as follows.

1. Determine a subset of eigenpairs of the Laplacian with suitable boundary conditions on the domain. For special domains this can be done analytically but in general must be done numerically.

2. Compute the dispersal relation (2.34) for the chosen reaction kinetics (this is independent of the geometry) and the range of admissible wave numbers as a function of d and γ.

3. Compute d^* and γ^* such that only one of the eigenvalues (wave numbers) computed in step 1 is in the range.

4. In order to compare with the patterned state, solve the reaction-diffusion system numerically with computed parameter values and compare with the numerically computed eigenfunctions.

It is possible to implement the above procedure simply because if a domain is bounded and the boundary is sufficiently regular, the Neumann Laplacian has a discrete spectrum of infinitely many non-negative eigenvalues with no finite accumulation point

$$0 < \lambda_1 \leq \lambda_2 \leq \cdots, \lambda_n \to \infty, \tag{2.48}$$

and this is due to the spectral theorem for compact self-adjoint operators (Benguria, 2015; Kreyszig, 1978; Taylor, 1996).

The aim is to have an algorithm to find the parameter values d and γ for a given eigenpair (k^2, W) such that only patterns analogous to W will grow. For this, one needs that the corresponding k is in the range defined in (2.41)

$$\gamma L = k_-^2 < k^2 < k_+^2 = \gamma R, \tag{2.49}$$

where

$$L = \frac{(df_a + g_m) - \sqrt{(df_a + g_m)^2 - 4d(f_a g_m - f_m g_a)}}{2d}, \tag{2.50a}$$

$$R = \frac{(df_a + g_m) + \sqrt{(df_a + g_m)^2 - 4d(f_a g_m - f_m g_a)}}{2d}, \tag{2.50b}$$

and that no other k is in this range. In other words, the sign of the polynomial $c(k^2)$ for

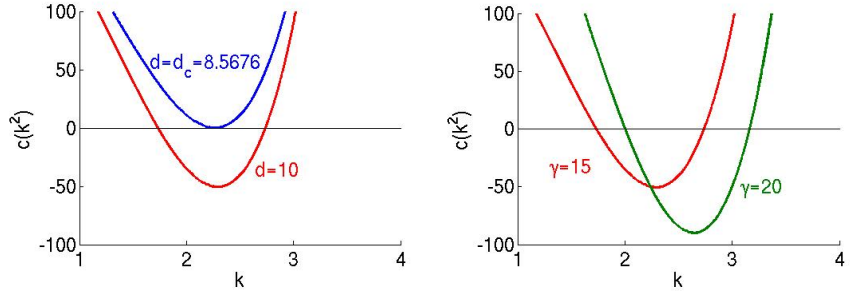

(a) $\gamma = 15$ (b) d = 10

Figure 2.1: Here the $c(k^2)$ is plotted (for Schnakenberg kinetics). For a fixed value of γ, when d is below the critical value d_c, $c(k^2)$ has no roots so no modes can be isolated. As d increases as does the difference between the two roots so there is more chance the value of k we seek will be between k_-^2 and k_+^2. Similarly, for a fixed value of d, increasing γ causes both k_-^2 and k_+^2 to increase.

a given k determines if the mode will grow. Figure 2.1 illustrates how the graph of $c(k^2)$ changes as d and γ are varied. On page 36, we defined the critical diffusion ratio d_c as the root of

$$d_c^2 f_a^2 + 2(2f_m g_a - f_a g_m)d_c + g_m^2 = 0, \tag{2.51}$$

$c(k^2)$ in the case when $d = d_c$ is illustated in Figure 2.1(a).

We find (k^2, W) either analytically or numerically. Then we propose the following algorithm described in pseudo-code:

Input: $d = d_c + \epsilon$, $\epsilon \approx d_c/5$, $\gamma > 0$, f, g and the $k_{l,n}$ that we wish to be uniquely isolated.

1. Compute k_-^2 and k_+^2 from (2.49).
2. If $k_{l,n}^2 < k_-^2$ increase γ by 1 (this number is arbitrary but should be small). This moves the curve to higher values of k.
3. If $k_{l,n}^2 < k_+^2$ decrease γ by 1. This moves the curve to lower values of k.
4. If there exists another $k_{l,n}^* \neq k_{l,n}$ such that $k_-^2 < k_{l,n}^{*2} < k_+^2$ then decrease ϵ by $d_c/100$. This shifts the curve upwards so the difference between k_-^2 and k_+^2 is smaller.
5. If $k_{l,n}$ is uniquely isolated END. If not go to 3.

Output: The appropriate d, γ.

Note that we cannot have $d < d_c$ (because then $c(k^2)$ would have no roots so the conditions on page 36 are not met), nor $\gamma < 0$ (because $k^2 > 0$).

2.6 Numerical methods

In order to validate that our mode isolation algorithm does indeed isolate the desired unstable mode, we will simulate the reaction-diffusion systems under consideration with the computed parameter values. To do this we employ a finite element method for the space discretisation and an implicit-explicit time-stepping scheme for the temporal approximation (Lakkis et al., 2013; Madzvamuse, 2006; Ruuth, 1995). We implement using the C++ software library deal.II (Bangerth et al., 2016). For an introduction and more information regarding the finite element method, see Section 1.6 and Appendix A, in particular the implementation used in this chapter is described in Section A.1.

2.6.1 Mesh generation

All the mesh generation is carried out using the deal.II library. We use hexahedral meshes for the volumes and quadrilaterals for the surfaces. In Figure 2.2 we exhibit different meshes generated by this package on which we will carry out computations. We also consider smooth surfaces; these meshes are generated by creating a triangulation Ω_h of the bulk of the domain Ω then the surface triangulation is defined by collecting the faces of the elements of the bulk triangulation that lie on the surface ($\Gamma_h = \Omega_h|_d\Omega$), i.e., the surface mesh is the trace of the volume mesh (in the example of the cylinder with open ends we use only the elements on the curved surface). For this reason the equations are not being approximated on the actual surface but on an approximation of it. For more details on surface mesh generation the reader is referred to Bangerth et al. (2016) and the references therein.

2.6.2 Numerical computations

We take the parameter values as shown in Table 2.1. The uniform states for Schnakenberg kinetics were obtained analytically while for the Gierer-Meinhardt and Thomas reaction kinetics these were calculated computationally using the Newton-Raphson method (Arfken et al., 2013; Madzvamuse, 2000). For the initial data we use small quasi-random perturbations around the uniform steady state values. The linear system (A.7) is solved using the conjugate gradient method (Bangerth et al., 2016; Golub and Van Loan, 1993; Hestenes and Stiefel, 1952).

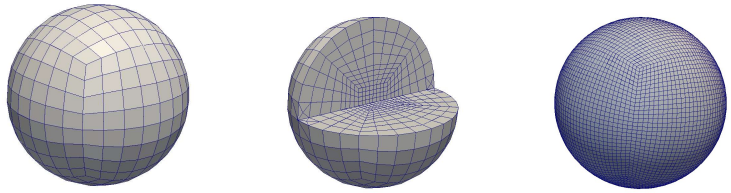

(a) Unit sphere

(b) Unit sphere cut to show inside

(c) Surface of sphere

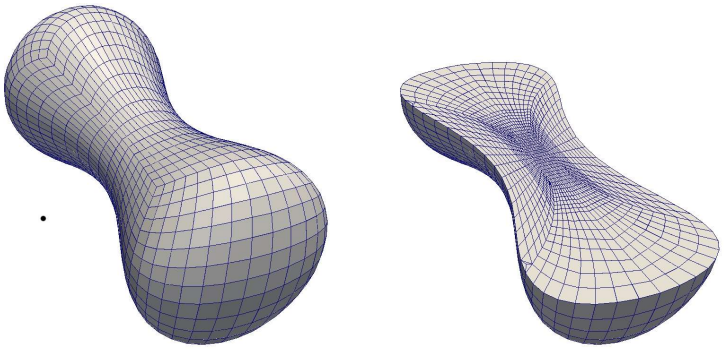

(d) Dumbbell mesh

(e) Inside dumbbell mesh

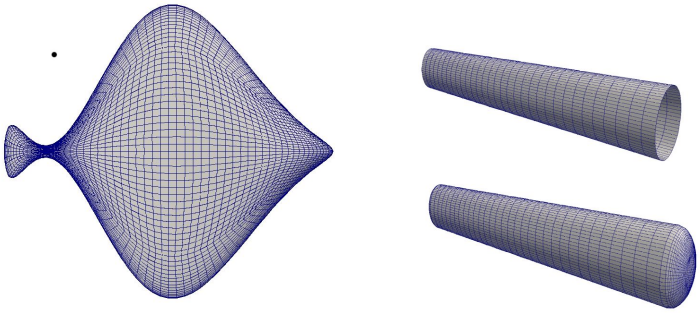

(f) "fish" mesh

(g) "eel" meshes (with and without boundary)

Figure 2.2: Examples of mesh generation for different volumes and surfaces: (a-c) Mesh generation on the unit sphere. (d-e) The dumbbell is a deformation of the bulk of a sphere. (f) The "fish" shape is a deformation of the surface of a sphere. (g) An "eel" is modelled by a cylinder with an open boundary and additionally as the same cylinder with added rounded boundaries.

Model	a	b	k	K	α	ρ	a_s	m_s
Schnakenberg	0.9	0.1					1	0.9
Gierer-Meinhart	0.1	1	0.5				0.8395	0.7047
Thomas	150	100		0.05	1.5	13	37.74	25.16

Table 2.1: Parameters for reaction kinetic models and the corresponding uniform steady states.

Domain	Type	Degrees of freedom	No. of cells	h
Sphere	Volume	3817	3584	0.0915064
Dumbbell	Volume	29521	28672	0.0280245
Sphere surface	Surface area	6146	6144	0.0630101
"fish"	Surface	6146	6144	0.00940557
"eel open"	Surface	2112	2048	0.0540314
"eel closed"	Surface	4610	4608	0.00631303

Table 2.2: Discretisation parameters. Time-step fixed as 10^{-3}.

2.6.3 Convergence

Figure 2.3 plots the L_2 norm of the discrete time-derivative of U and V against the elapsed time. To begin with the difference is large. This quickly decays due to diffusion then there is a rapid growth, because of the exponentially growing modes. The time-derivative eventually starts to decay due to the effects of the nonlinear terms that act to bind the exponentially growing solution thereby giving rise to a spatially inhomogeneous steady state.

2.7 Isolating modes on general domains

On arbitrary domains, analytical solutions for the eigenvalue problem are not typically available but approximate eigenpairs can be computed numerically. Numerically approximating these pairs is a significant challenge. In general, as we are typically interested in a small number of eigenpairs, it is not necessary to find all solution pairs, however for our approach to mode isolation to remain applicable, it is important that we obtain consecutive pairs.

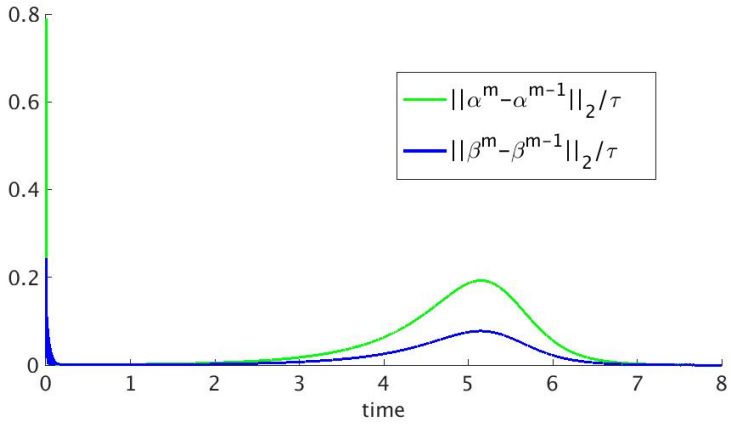

Figure 2.3: Plot of the L_2 norm of the discrete time-derivative over time for a typical example. There is an initial decay due to diffusion followed by a growth because of the exponentially growing modes which eventually decays, due to the dominant nonlinear terms.

As previously stated, the eigenvalue problem we wish to solve is as follows,

$$\begin{cases} \Delta W + k^2 W = 0, & \boldsymbol{x} \in \Omega, \\ (\mathbf{n} \cdot \nabla) W = 0, & \boldsymbol{x} \in \partial\Omega. \end{cases} \tag{2.52}$$

To approximate the solution we employ the finite element method for the spatial discretisation outlined in Section A.1. We work with the weak formulation of the eigenvalue problem and look for an approximate eigenpairs $(W_h, k_h^2) \in V_h \times \mathbb{R}_+$ (where V_h contains all continuous piecewise linear functions on a given mesh) such that

$$\int_\Omega \nabla W_h \cdot \nabla \phi = k^2 \int_\Omega W_h \cdot \phi, \qquad \forall \phi \in V_h. \tag{2.53}$$

As in (A.4) this may be written in matrix-vector form, we want to find $(\mathbf{w}, k_h^2) \in \mathbb{R}^m \times \mathbb{R}_+$, where m is the dimension of V_h such that

$$\mathbf{A}\mathbf{w} = k^2 \mathbf{M}\mathbf{w}, \tag{2.54}$$

where $\mathbf{A}$ and $\mathbf{M}$ are stiffness and mass matrices defined in the same way as in equation (A.5). This is a generalised eigenvalue problem. We utilise the same finite element software library as we use for numerical simulations, namely, deal.II (Bangerth et al., 2016), in this case for its approximation using SLEPc and the Krylov-Schur algorithm.

2.8 Comparisons of eigenfunctions and spatially inhomogeneous steady states

2.8.1 Example 1: Sphere

We start by considering the unit sphere, a domain for which the eigenvalue problem can be solved analytically. We will refer back here later in the thesis because we assume the starting shape to be a sphere in our 3D simulations of a cell moving.

Eigenvalues and eigenfunctions on a sphere

The wavenumbers on the sphere are found by solving the eigenvalue problem. The solutions of this are well known and are obtained using separation of variables (Arfken et al., 2013; Morimoto, 1998). First, it is necessary to convert into spherical coordinates with

$$x = r\sin\theta\cos\phi, \quad y = \sin\theta\sin\phi, \quad z = r\cos\theta. \tag{2.55}$$

Substituting these into $\Delta w + k^2 w = 0$ leads to

$$\frac{1}{r^2}\frac{\partial}{\partial r}\left(r^2\frac{\partial w}{\partial r}\right) + \frac{1}{r^2\sin\theta}\frac{\partial}{\partial\theta}\left(\sin\theta\frac{\partial w}{\partial\theta}\right) + \frac{1}{r^2\sin^2\theta}\frac{\partial^2 w}{\partial\phi^2} + k^2 w = 0. \tag{2.56}$$

Similarly to Arfken et al. (2013), we assume there are solutions of the form $w(r,\theta,\phi) = R(r)Y(\theta,\phi)$. Multiplying through by $\frac{r^2}{RY}$, we can separate into two equations:

$$\frac{1}{R}\frac{\partial}{\partial r}\left(r^2\frac{\partial R}{\partial r}\right) + k^2 r^2 = c, \quad \frac{1}{Y}\frac{1}{\sin\theta}\frac{\partial}{\partial\theta}\left(\sin\theta\frac{\partial Y}{\partial\theta}\right) + \frac{1}{Y}\frac{1}{\sin^2\theta}\frac{\partial^2 Y}{\partial\phi^2} = -c, \tag{2.57}$$

where c is a constant. It happens that $c = l(l+1)$. Multiplying the first equation of (2.57) by R we obtain

$$r^2\frac{\partial^2 R}{\partial r^2} + 2r\frac{\partial R}{\partial r} + [k^2 r^2 - l(l+1)]R = 0. \tag{2.58}$$

Since we are now only working on the radius of the circle (so in one dimension), we can let $x = kr$ and look for solutions of the form $R(r) = X(x)x^{-\frac{1}{2}}$, so we now have

$$x^2\frac{\partial^2 X}{\partial x^2} + x\frac{\partial X}{\partial x} + [x^2 - (l+\frac{1}{2})^2]X = 0. \tag{2.59}$$

This is a Bessel differential equation, whose solutions we defined these in Section 2.2.1. The normalised general solution is

$$R(r) = A\frac{J_{l+\frac{1}{2}}(kr)}{\sqrt{kr}} + B\frac{Y_{l+\frac{1}{2}}(kr)}{\sqrt{kr}}. \tag{2.60}$$

We require the solution to be continuous and therefore not unbounded as $r \to 0$, this means $B = 0$. Next we must satisfy the Neumann boundary conditions ($\frac{\partial w}{\partial r} = 0$ when

$r = 1$). To do this we define $j'_{l+\frac{1}{2},n}$ as the zeros of $J'_{l+\frac{1}{2}}(kr)$. Therefore the eigenvalues and eigenfunctions are

$$\lambda_{l,n} = k^2_{l,n} = (j'_{l+\frac{1}{2},n})^2, \quad f_{l,n}(r) = J_{l+\frac{1}{2}}(j'_{l+\frac{1}{2},n}r), \quad l = 0, 1, 2, ..., \quad n = 1, 2, 3, ... \tag{2.61}$$

Now considering the second equation of (2.57), we separate variables again by assuming $Y(\theta, \phi) = \Theta(\theta)\Phi(\phi)$, to obtain the two equations:

$$\frac{1}{\Phi}\frac{\partial^2\Phi}{\partial\phi^2} = -m^2, \quad l(l+1)\sin^2(\theta) + \frac{\sin\theta}{\Theta}\frac{\partial}{\partial\theta}\left(\sin\theta\frac{\partial\Theta}{\partial\theta}\right) = m^2. \tag{2.62}$$

The first gives the general solution $\Theta(\theta) = Be^{im\phi} + Ce^{-im\phi}$. In the second, we can use the substitution

$$x = \cos\theta \quad \Longrightarrow \quad \sin^2\theta = 1 - x^2 \quad \& \quad \partial\theta = -\frac{\partial x}{\sin\theta}, \tag{2.63}$$

so the equation assumes the form of the Associated Legendre Differential Equation:

$$\frac{\partial}{\partial x}\left[(1-x^2)\frac{\partial\Theta}{\partial x}\right] + \left[l(l+1) - \frac{m^2}{1-x^2}\right]\Theta = 0, \tag{2.64}$$

which, for a given integer $l \geq 0$, and each integer m such that $-l \leq m \leq l$, has the solutions

$$\Theta = P_l^m(x) = (-1)^m(1-x^2)^{\frac{m}{2}}\frac{\partial^m}{\partial x^m}(P_l(x)), \tag{2.65}$$

where $P_l(x)$ is the Legendre polynomial which can be defined by $P_l(x) = \frac{1}{2^l l!}\frac{\partial^l}{\partial x^l}(x^2-1)^l$. (**Note:** It is sufficient to say $l \geq 0$ because if $l < 0$, $l(l+1) = ((-1-l')((-1-l')+1) = l'(l'+1)$ for some $l' \geq 0$.)

Therefore, for the full system we have:

$$w^m_{l,n}(r, \theta, \phi) = A^m_{l,n}J_{l+\frac{1}{2}}(j'_{l+\frac{1}{2},n}r)e^{im\phi}P_l^m(\cos\theta), \tag{2.66}$$

where $A^m_{l,n}$ is a constant.

Thus, there are an infinite number of solutions of this form with corresponding wavenumbers $k^2_{l,n} = (j'_{l+\frac{1}{2},n})^2$. We can find the eigenvalues $k^2_{l,n} = (j'_{l+\frac{1}{2},n})^2$ numerically (using the fact that $J'_{l+\frac{1}{2},n} = \frac{l}{k}J_{l+\frac{1}{2}}(k) - J_{l+\frac{3}{2}}(k)$). The first 21 of these are shown in Table 2.3. It follows that for each eigenvalue $\lambda_{l,n} = k^2_{l,n}$ there are $2l+1$ possible eigenfunctions. Figure 2.4 shows the eigenfunctions for some selected values of l, m and n. For example $k_{1,1} = 2.08158$ is the first zero of $J_{\frac{3}{2}}(x)$ and corresponds to the eigenfunctions

$$w^m_{1,1}(r, \theta, \phi) = J_{\frac{3}{2}}(k_{1,1}r)e^{im\phi}P_1^m(\cos\theta), \text{ with } m = -1, 0, 1. \tag{2.67}$$

The spherical Bessel function is given by $J_{\frac{3}{2}}(k_{1,1}r) = \frac{\sin(k_{1,1}r)}{(k_{1,1}r)^2} - \frac{\cos(k_{1,1}r)}{k_{1,1}r}$. Meanwhile $Y_1^m = e^{im\phi}P_1^m(\cos\theta)$ are spherical harmonics whose real parts can be written in Cartesian

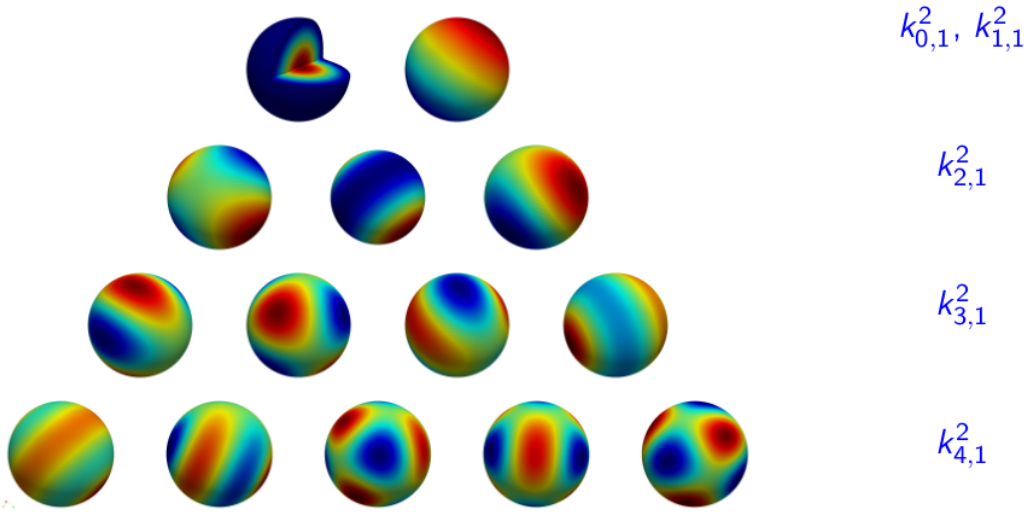

Figure 2.4: Analytical solutions to the eigenvalue problem on the unit sphere i.e. (2.66) for selected values of l, m, n. For $l \geq 1$ there are multiple eigenfunctions for each eigenvalue.

n	$k^2_{0,n}$	$k^2_{1,n}$	$k^2_{2,n}$	$k^2_{3,n}$	$k^2_{4,n}$	$k^2_{5,n}$
1	4.4934	2.0816	3.3421	4.5141	5.6467	6.7565
2	7.7253	5.9404	7.2899	8.5838	9.8404	11.0702
3	10.9041	9.2058	10.6139	11.9727	13.2956	14.5906
4	14.0662	12.4044	13.8461			

Table 2.3: Zeros of the first derivatives of the spherical Bessel functions. These are our wavenumbers $k^2_{l,n}$.

coordinates as $Y_1^{-1} = \sqrt{\frac{3}{4\pi}} \cdot \frac{y}{r}$, $Y_1^0 = \sqrt{\frac{3}{4\pi}} \cdot \frac{z}{r}$ and $Y_1^1 = \sqrt{\frac{3}{4\pi}} \cdot \frac{x}{r}$ (Hobson, 1931). Since the system we are solving is not sensitive to polarity we can consider these to be equivalent. Figure 2.4 contains a plot of the eigenfunction

$$w_{1,1}^1 = \left(\frac{\sin(k_{1,1}r)}{(k_{1,1}r)^2} - \frac{\cos(k_{1,1}r)}{k_{1,1}r}\right) \cdot \frac{x}{r}, \tag{2.68}$$

corresponding to $k_{1,1}^2$, where as usual $r^2 = x^2+y^2+z^2$. The second example, $k_{2,1} = 3.34209$ corresponds to the eigenfunctions

$$w_{2,1}^m(r,\theta,\phi) = J_{\frac{5}{2}}(k_{2,1}r)e^{im\phi}P_2^m(\cos\theta), \text{ with } -l \leq m \leq l. \tag{2.69}$$

Choosing $m = 0$, converting the above to Cartesian coordinates and taking the real part gives

$$w_{2,1}^0(x,y,z) = \left(\left(\frac{3}{k_{2,1}^2r^2} - 1\right)\frac{\sin(k_{2,1}r)}{k_{2,1}r} - \frac{3\cos(k_{2,1}r)}{k_{2,1}^2r^2}\right)\left(\frac{1}{4}\sqrt{\frac{5}{\pi}} \cdot \frac{-x^2-y^2+2z^2}{r^2}\right).$$

The plot of the function $w_{2,1}^0$ is shown in the middle of the second row of Figure 2.4.

Mode isolation on the sphere

Using the method described in Section 2.5 with all other parameters fixed as in Table 2.1 we can isolate the wavenumbers for the reaction-diffusion system with Schnakenberg kinetics and these are shown in Table 2.4. Similarly, for Thomas and Gierer-Meinhart (Table 2.5). In all these cases the interval $[k_-, k_+]$ is centred on $k_{l,n}$.

d	γ	k_-	k_+	Wavenumbers excited
10	15	1.7321	2.7386	$k_{1,1} = 2.08158$
10	40	2.8284	4.4721	$k_{2,1} = 3.34209$
9	60	3.9319	5.0866	$k_{0,2} = 4.49341$, $k_{3,1} = 4.51410$
8.81	85	4.8575	5.8955	$k_{4,1} = 5.64670$

Table 2.4: Given a particular d and γ we obtain values for k_- and k_+ meaning that the shown wavenumbers are isolated on the sphere, for the system with Schnakenberg kinetics.

Simulations of the reaction-diffusion systems on the unit sphere

Solving using deal.II we use the mesh shown in Figure 2.2(a). The time-step is taken to be $\tau = 10^{-3}$. We take the initial conditions to be a small random perturbation from the

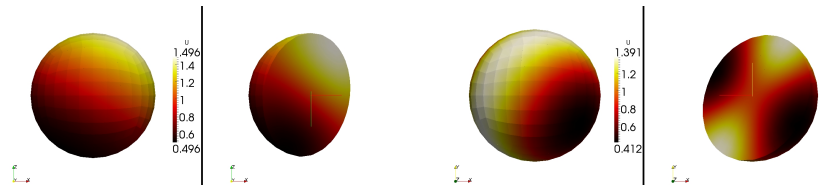

(a) $\gamma = 15$, d=10 (b) $\gamma = 40$, d=10

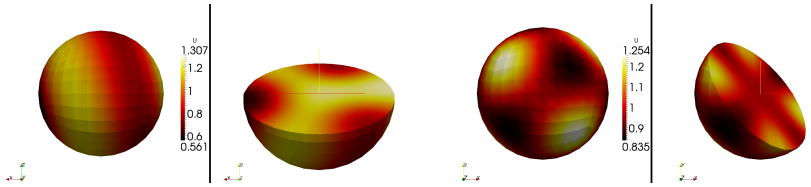

(c) $\gamma = 70$, d=9 (d) $\gamma = 85$, d=8.81

Figure 2.5: Converged solutions of system (2.20) with Schnakenberg kinetics (2.45). These solutions represent the species u. The isolated modes are $w^1_{1,1}$, $w^0_{2,1}$, $w^0_{3,1}$ and $w^{-3}_{4,1}$.

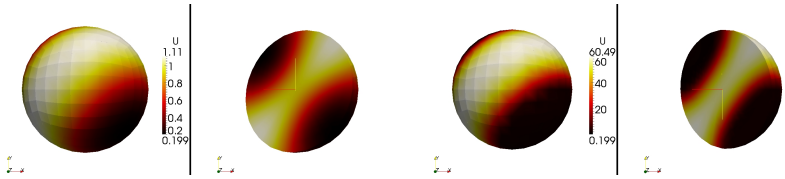

(a) GM, $\gamma = 80$, d=74 (b) Thomas, $\gamma = 40$, d=30

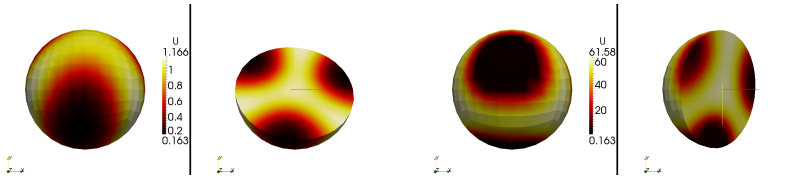

(c) GM, $\gamma = 160$, d=74 (d) Thomas, $\gamma = 70$, d=28

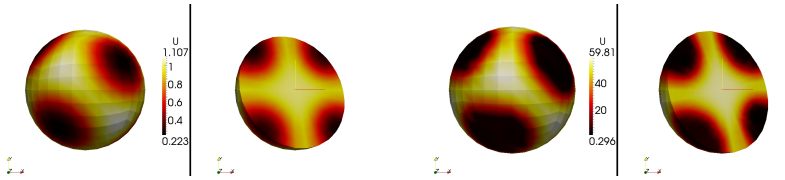

(e) GM, $\gamma = 200$, d=72 (f) Thomas, $\gamma = 90$, d=27.5

Figure 2.6: Converged solutions of system (2.20) for the species u with Gierer-Meinhart kinetics (2.46) on the left with isolated modes $w^0_{2,1}$, $w^3_{3,1}$ and $w^{-3}_{4,1}$ and Thomas (2.47) on the right with isolated modes $w^0_{2,1}$, $w^{-2}_{3,1}$ and $w^{-3}_{4,1}$.

Gierer-Meinhart	Thomas	Wavenumbers excited
d=74 γ=30	d=30 γ=15	$k_{1,1}$
d=74 γ=80	d=30 γ=40	$k_{2,1}$
d=74 γ=160	d=28, γ=60	$k_{0,2}$, $k_{3,1}$
d=72 γ=200	d=27.5 γ=90	$k_{4,1}$

Table 2.5: The values of d and γ which isolate the given wavenumbers on the sphere for the Gierer-Meinhart and Thomas reaction kinetics.

previously computed homogeneous steady state. So for the reaction-diffusion system with Schnakenberg kinetics, at each point in the grid we set the initial conditions to be:

$$\alpha^0 = 0.995 + 0.01\epsilon, \quad \beta^0 = 0.895 + 0.01\epsilon, \tag{2.70}$$

where ϵ is a uniformly distributed random variable between 0 and 1.

For each eigenvalue there are a number of different eigenfunctions. Computing using the values obtained with mode isolation, the solution converges to either one of the eigenfunctions or a linear combination. These converged solutions are shown in Figure 2.5 and 2.6. It is possible to force the solution to converge to an eigenfunction (which it does not appear to with random initial perturbation) by making a suitable choice of initial condition, for example a perturbation of the desired eigenfunction, suitably scaled. Hence, in the case where multiple wave numbers are excited, pattern selection is heavily influenced by the choice of initial conditions which act as the basin of attraction, one of the major criticisms of Turing's theory for pattern formation (Bard and Lauder, 1974). We notice similar phenomena later in the thesis in our mechanobiochemical model. See Section 3.6. Since the results are very similar for the three different models, in all subsequent examples we only show the results for Schnakenberg kinetics.

2.8.2 Example 2: Dumbbell

As a second example we consider the dumbbell shaped domain shown in Figure 2.2(d). The solver for the eigenvalue problem on this mesh gives the output of eigenvalues and eigenfunctions shown in Figure 2.7. Figure 2.8 shows the converged solutions of the reaction-diffusion system when the chosen values of d and γ isolate the corresponding wavenumbers $k_i^2 = \lambda_i$. It must be observed that the pattern computed will be a scalar multiple of the eigenfunction. This scalar may be negative which results in a reversed pattern (compare for example Figure 2.7 (f) and 2.8 (e). This is also seen later in 2.10 (a), (c), and (d)).

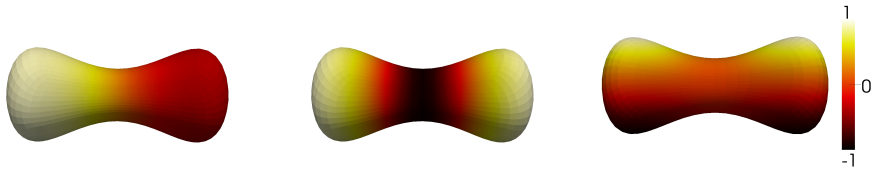

(a) $\lambda_1 = 1.49$ (b) $\lambda_2 = 12.68$ (c) $\lambda_3 = 22.86$

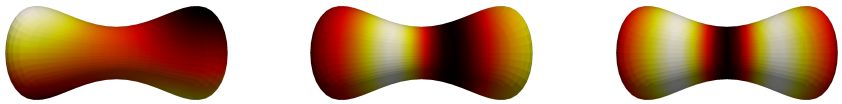

(d) $\lambda_4 = 22.98$ (e) $\lambda_5 = 26.52$ (f) $\lambda_6 = 49.91$

Figure 2.7: Eigenfunctions corresponding to the labelled eigenvalues on the dumbbell. These are solutions of (2.52) approximated using deal.II.

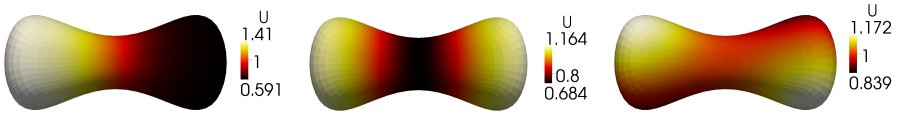

(a) d=10, $\gamma = 5$ (b) d=9, $\gamma = 40$ (c) d=8.8, $\gamma = 60$

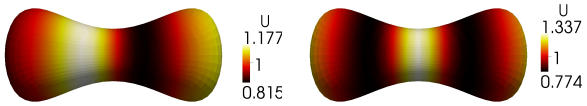

(d) d=8.8, $\gamma = 88$ (e) d=8.65, $\gamma = 130$

Figure 2.8: Converged u solutions of system (2.20) with Schnakenberg kinetics (2.45) on a dumbbell. Eigenvalues $\lambda_1, \lambda_2, \lambda_5, \lambda_6$ have been isolated, however since $\lambda_3 \approx \lambda_4$ in (c) we see a linear combination of their eigenfunctions. It must be noted that the pattern can appear to be reversed (e.g. in (e)), this is due to the choice of the initial conditions. Choosing appropriate initial conditions results in a pattern similar to that shown in Figure 2.7(e).

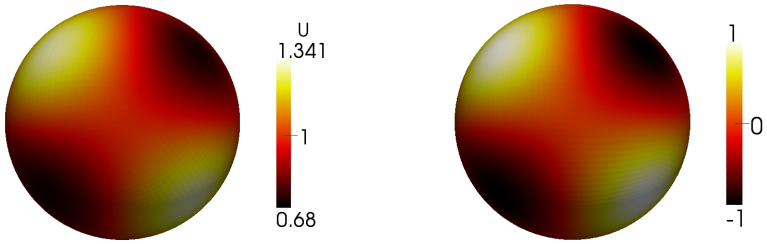

(a) The surface finite element solution with given parameters $d = 9$ and $\gamma = 35$

(b) Numerically computed eigenfunction corresponding to eigenvalue $\lambda_9 = 12.0186$

Figure 2.9: Mode isolation for the reaction-diffusion system with Schnakenberg kinetics on the surface of the sphere.

2.8.3 Example 3: Surface of a sphere

In all the previous examples we considered bulk, volumetric domains. In this example we have a curved surface as the domain. This means using the Laplace Beltrami operator Δ_Γ instead of the Laplacian Δ in (2.52) and (2.20). To approximate solutions in this case, we employ the surface finite element method (Barreira et al., 2011; Dziuk, 1988; Dziuk and Elliott, 2013; Elliott and Ranner, 2014; Elliott et al., 2012; Madzvamuse and Chung, 2016).

The eigenpairs on the surface of the unit sphere can be found analytically and are well known and documented in Chaplain et al. (2001) for example. The eigenfunctions are referred to as spherical harmonics. They are the restriction of the eigenfunctions (3.14) to the surface. The eigenvalues are of the form $k^2 = l(l+1)$, where l is an integer, and the eigenfunctions are

$$w_l^m(\theta, \phi) = A_l^m e^{im\phi} P_l^m(\cos\theta), \tag{2.71}$$

where m and P_l^m are as described in Section 2.8.1. Therefore we can test the performance of the eigenvalue problem solver with this example. Using the eigenvalue solver on an approximated mesh of the surface of the sphere using 98306 degrees of freedom we obtain

the following output of the first 30 eigenvalues computed to 6 significant figures.

$$\begin{aligned} k_h^2 \ = & \ 2.00009,\ 2.00009,\ 2.00009,\ 6.00042,\ 6.00042,\ 6.00042,\ 6.00053,\ 6.00053, \\ & \ 12.0013,\ 12.0015,\ 12.0015,\ 12.0015,\ 12.0016,\ 12.0017,\ 12.0017,\ 20.003, \\ & \ 20.003,\ 20.0032,\ 20.004,\ 20.0041,\ 20.0042,\ 20.0042,\ 20.0045,\ 20.0046, \\ & \ 30.0066,\ 30.0067,\ 30.0067,\ 30.0068,\ 30.0081,\ 30.0095. \end{aligned} \tag{2.72}$$

As expected these are the first 5 values of the form $k^2 = l(l+1)$ with $l = 1, 2, 3, 4, 5$. The multiplicity is due to the fact that for each l there are $2l + 1$ eigenfunctions (see Section 2.8.1). It must be observed that the finite element method is known to be less effective for higher eigenvalues due to the min-max theorem (Strang and Fix, 1973). This means we must use a highly refined mesh in order to obtain values that are closer to the analytical values. The eigenfunctions are analogous to those detailed in Section 2.8.1 restricted to the boundary. This shows that the eigenvalue solver gives the required output. Since the results are shown in Section 2.8.1 we only show one example of mode isolation in Figure 2.9. As mentioned in Section 2.4, γ can be thought of as being proportional to the domain size. Here we only consider a sphere with radius one. As the size of the sphere (radius R) increases, the eigenvalues decrease (specifically they are multiplied by $\frac{1}{R^2}$). This effect is demonstrated in Lacitignola et al. (2017) where they show that fixing other values and increasing R causes higher mode patterns and hence more complex patterns are obtained.

2.8.4 Example 4: "fish" surface

We now consider a smooth surface on which no analytical expression for the eigenpairs is available, the surface is taken to be diffeomorphic to the sphere and is shown in Figure 2.2(f), it is meant to (very loosely) mimic the shape of a fish. We found the first 100 eigenpairs then chose several to isolate. These are shown in Figure 2.10. Various patterns are observed including stripes, spots and concentric rings.

2.8.5 Example 5 and 6 "eel" shapes

When computing on surfaces, one has to consider whether or not the surface has a boundary. In papers modelling fish or eel patterns (see for example Venkataraman et al. (2011)), a surface with a boundary is often used. To investigate whether having a boundary is significant in this example we consider a surface with and without boundary. We see that the eigenvalues and eigenfunctions are very similar and it is possible to isolate similar patterns using the same parameter values.

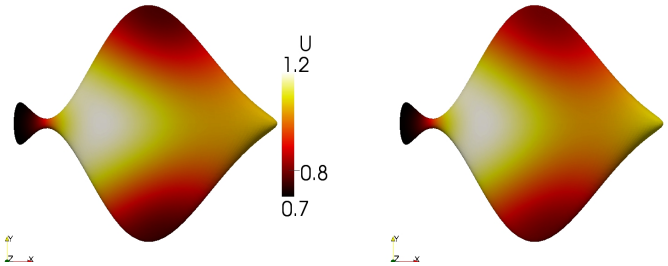

(a) $d = 8.9$, $\gamma = 130$

(b) $\lambda_5 = 40.18$

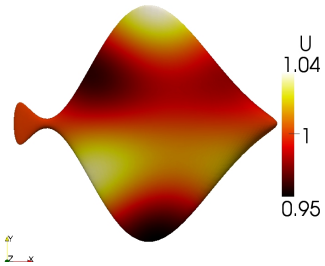

(c) $d = 8.58$, $\gamma = 240$

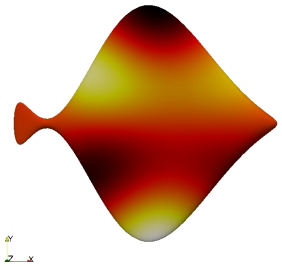

(d) $\lambda_{10} = 79.56$

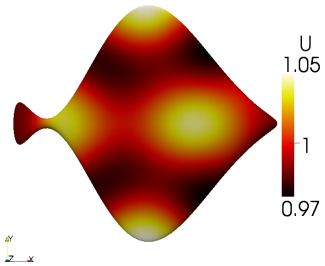

(e) $d = 8.58$, $\gamma = 400$

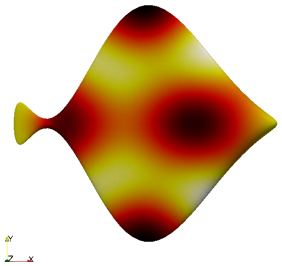

(f) $\lambda_{15} = 134.73$

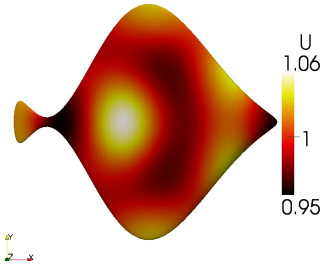

(g) $d = 8.58$, $\gamma = 510$

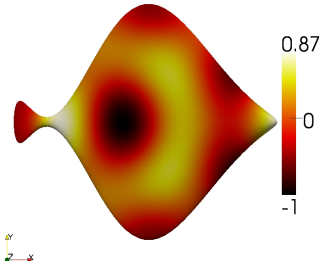

(h) $\lambda_{19} = 175.98$

Figure 2.10: Surface finite element solutions corresponding to the u species of the reaction-diffusion system with Schnakenberg kinetics with the given parameters on the left and numerically computed eigenfunctions corresponding to the given eigenvalue on the right. Again we observe reversed modes as described in subsection 2.8.2.

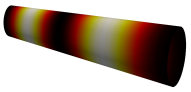

(a) $\lambda_{4(open)} = 54.43$

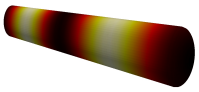

(b) $\lambda_{4(closed)} = 44.94$

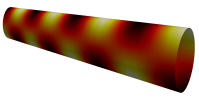

(c) $\lambda_{23(open)} = 253.69$

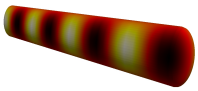

(d) $\lambda_{25(closed)} = 257.54$

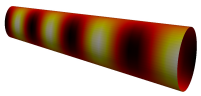

(e) $\lambda_{24(open)} = 253.73$

Figure 2.11: Eigenfunctions of the Laplace-Beltrami operator on the "eel" shape with the corresponding eigenvalue. The left column shows the surface without a boundary and the right has a boundary. Note that, although the eigenfunctions are different, $\lambda_{23} \approx \lambda_{24}$.

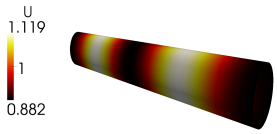

(a) $d = 8.8$, $\gamma = 140$

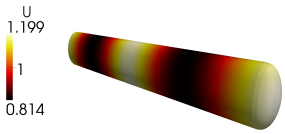

(b) $d = 8.8$, $\gamma = 140$

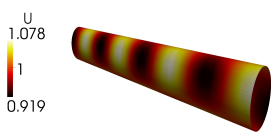

(c) $d = 8.6$, $\gamma = 750$

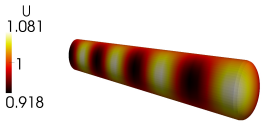

(d) $d = 8.6$, $\gamma = 750$

Figure 2.12: Converged solutions corresponding to the u species of the reaction-diffusion system with Schnakenberg kinetics on the surface of an eel. The surfaces on the right have a boundary whereas those on the left do not. We find that using the same parameter values on both surfaces gives very similar results.

2.8.6 Quantitative comparisons

By inspecting the plots it can be observed that the modes qualitatively appear to be isolated. To further expand on this, we normalise both the solutions and eigenfunctions so that all values are the range $[-1, 1]$ then compute the L_2 norm of their difference and results of these computations are shown in Table 2.6. Results on the sphere are not possible due to rotational symmetry. It turns out that these L_2 norm differences are small and are due to a number of factors: Firstly, the chosen numerical parameters: the differences get smaller and smaller with further grid refinement. On the other hand, numerical tests seem to suggest that refining the time-step does not make a significant difference in the decrease of the L_2 norms. Secondly, due to mode clustering, the L_2 norm differences can be affected by small contributions from nearby modes that are residing in the same excitable region. Lastly, the treatment of the nonlinear terms plays a significant role in the decrease of these L_2 norm differences.

Dumbbell	L_2	"Fish"	L_2
ω_1	0.35029	ω_5	0.076100
ω_2	0.034952	ω_{10}	0.015871
ω_5	0.020861	ω_{15}	0.010345
ω_6	0.010280	ω_{19}	6.9365×10^{-3}

Table 2.6: L_2 norm of difference between converged solution and the selected eigenfunction $(U - \omega_k)$ are found for the examples shown.

2.9 Conclusion and further challenges

In this chapter, we have considered reaction-diffusion systems and have presented a framework for isolating particular spatially inhomogeneous patterns. The method involves finding eigenpairs of the Laplacian, (or more generally Laplace-Beltrami), and computing parameters such that when the reaction-diffusion system is solved numerically, only patterns analogous to a particular eigenfunction will grow. In previous works the eigenvalue problem is solved analytically whereas in this paper both the eigenvalue problem and the reaction-diffusion system are solved using the finite element method. Advances in numerical software mean that we can find 100 eigenpairs in a few minutes and we have demonstrated that these eigenpairs match analytical results. The approach is shown to work for 3 different examples of nonlinear reaction kinetics and on a variety of domains

and surfaces. In summary, the main observations are:

- Mode isolation is straightforward for low values of k^2 but can become slightly more difficult for higher values of k^2. This is due to the approximation of the nonlinear terms and clustering of the eigenvalues of the linear problem.

- When two or more eigenvalues are clustered close to each other it becomes difficult to isolate them computationally as well as analytically. If two or more eigenvalues are in the permissible range then the inhomogeneous steady state could be a linear combination of the corresponding eigenfunctions.

- We display an example of two surfaces where pattern formation appears to be robust despite the fact one has a boundary while the other does not. An interesting investigation would be to see if this can be true for other geometries. Note that this observation is only for the case of zero-flux boundary conditions. Imposing Dirichlet or Robin-type boundary conditions would result in substantially different patterns.

In this chapter we have only considered stationary volumes and surfaces. However the domains of biological processes generally evolve with time (Barreira et al., 2011; Elliott et al., 2012; Lakkis et al., 2013; Madzvamuse, 2006; Venkataraman et al., 2011). This adds more complexity to solving the reaction-diffusion systems. An interesting and natural extension of this work would be to introduce domain growth and surface evolution. For this extension, studies on the effects of initial conditions would also be worthwhile.

For the rest of this thesis we will be formulating a model for cell movement which will include a reaction-diffusion system. It will be possible to isolate modes in a similar way for small time. However, at longer timescales, the deformation may be large and irregular, so mode isolation will be too time consuming to be useful. In the next chapter, we will introduce the model and begin our extension of it.

Chapter 3

Model 1: A 3D mechanobiochemical model with a single actin reaction-diffusion model

3.1 Introduction

In this chapter we introduce the first of two models for cell motility. This model is an extension of a previous model, from 2D to 3D. The equations are derived, linear stability analysis is carried out and numerical simulations are presented.

3.1.1 Origins of the model

The model we consider and extend is inspired by contractile models of the actin cytogel by Lewis and Murray (1991) and Oster et al. (1985). These models are composed of a force balance equation modelling the displacements of the cell when deformed and a reaction-diffusion equation for the concentration of the gel that in turn drives cell movement. The idea of pressure driven protrusion and the use of concentration of actin originates from Alt and Tranquillo (1995). In their model they assume movement is produced by a balance between contractile force of the actin network pulling on the membrane and pressure pushing on the membrane.

This was extended by Stephanou et al. (2004) so that large deformations could be modelled which is more realistic for most cells. George (2012) further extended this model

by adding that higher actin concentration in a region leads to more pressure.

In the previous models a polar coordinate system was used and radial extension of the cell was calculated (Alt and Tranquillo, 1995; Stephanou et al., 2004). Unlike this approach, we follow the work of George (2012) and study the mechanobiochemical model in its physical Cartesian coordinates without any need for coordinate transformation. In this chapter, we undertake our first major extension of the work by George (2012) by extending the same model to three dimensions. We remark further, that in this chapter, we will consider (as in previous studies) a single reaction-diffusion equation for F-actin with no other molecular species involved. Extensions to include more species are undertaken in Chapter 4.

3.2 Derivation of a single actin reaction-diffusion equation on moving 3D geometries

The model described in this chapter is the same as that of George (2012) but implemented in three rather than two dimensions. The RDE derivation is much the same as in Section 2.3.1 except that we are now considering a moving volume, thus, we introduce the flow velocity $\boldsymbol{\beta} = \frac{\partial \mathbf{u}}{\partial t}$. We assume that the cell shape is a simply connected and continuously deforming domain: $\boldsymbol{\Omega}_t \subset \mathbb{R}^3$ with boundary $\partial\boldsymbol{\Omega}_t$, where $t \in I = [0, T_f]$, $T_f > 0$. Any point $\boldsymbol{x} \in \boldsymbol{\Omega}_t$ is defined by $\boldsymbol{x} = (x(t), y(t), z(t))$. We define the displacement of $\boldsymbol{x}$ at time t by $\mathbf{u} = (u(\boldsymbol{x}(t), t), v(\boldsymbol{x}(t), t), w(\boldsymbol{x}(t), t))^T$. Let the concentration of F-actin at point $\boldsymbol{x}(t)$ be $a = a(\boldsymbol{x}(t), t)$. Define a_c to be the concentration of F-actin at chemical equilibrium. This differentiates the states of polymerisation and depolymerisation. Therefore, given a polymerisation rate k_a we can describe the net formation of F-actin from G-actin by $k_a(a_c - a)$. To define the equation we consider the flux $\mathbf{J}(\boldsymbol{x}(t), t) \in C^1(R_t)$ where $R_t \subset \boldsymbol{\Omega}_t$ is a portion of $\boldsymbol{\Omega}_t$ with boundary ∂R_t. This is the amount of actin which passes the across boundary. The conservation equation tells us that the rate of change of the total amount of a material in a volume is equal to the flux through (normal to) the surface boundary plus the net formation of the material within the volume. Hence we can write the conservation of actin as follows

$$\frac{\partial}{\partial t}\int_{R_t} a \, dR_t = -\int_{\partial R_t} \mathbf{J} \cdot \mathbf{n} \, d\mathbf{S} + \int_{R_t} k_a(a_c - a) \, dR_t, \tag{3.1}$$

where n is the unit normal to the boundary ∂R_t. Using the divergence theorem on the boundary integral leads to

$$\frac{\partial}{\partial t}\int_{R_t} a\, dR_t = \int_{R_t} (-\nabla \cdot \mathbf{J} + k_a(a_c - a))\, dR_t. \tag{3.2}$$

Here we can use the Reynolds transport theorem (for proof and use of this see Madzvamuse (2000); Acheson (1990)) which says, for $a(\boldsymbol{x}, t)$, a scalar function, and the material derivative $\frac{Da}{Dt} = \frac{\partial a}{\partial t} + \boldsymbol{\beta}\nabla a$, then

$$\frac{\partial}{\partial t}\int_{R_t} a\, dR_t = \int_{R_t} \Big(\frac{Da}{Dt} + a(\nabla \cdot \boldsymbol{\beta})\Big) dR_t. \tag{3.3}$$

Using this theorem and the product rule turns (3.2) into

$$\int_{R_t} \Big(\frac{\partial a}{\partial t} + \nabla \cdot (a\boldsymbol{\beta})\Big) dR_t = \int_{R_t} (-\nabla \cdot \mathbf{J} + k_a(a_c - a))\, dR_t. \tag{3.4}$$

Here we assume F-actin flows from high to low concentrations at a magnitude proportional to the concentration gradient. This means we can use Fick's law as in Section 2.3.1, and obtain that

$$\int_{R_t} \Big(\frac{\partial a}{\partial t} + \nabla \cdot (a\boldsymbol{\beta}) - D_a \Delta a - k_a(a_c - a)\Big) dR_t = 0, \tag{3.5}$$

where D_a is a positive constant diffusion coefficient for F-actin. Since this holds for any arbitrary domain $R_t \subset \boldsymbol{\Omega}_t$ and the integrand is continuous we have:

$$\frac{\partial a}{\partial t} + \nabla \cdot (a\boldsymbol{\beta}) - D_a \Delta a = k_a(a_c - a) \text{ for } \boldsymbol{x} \in \boldsymbol{\Omega}_t,\ t \in I. \tag{3.6}$$

The boundary conditions are zero flux because actin does not flow in or out of the cell. In the case $\boldsymbol{\beta} = 0$ we have a reaction-diffusion equations on a stationary volume.

3.3 A viscoelastic model of cell motility

For the sake of completeness, we state the model for the displacement of the cell through a force balance equation. The key point is that cell deformation is determined by the active mechanical forces. These forces are mostly due to the mechanical properties of the actin network. The F-actin network and myosin interact to generate contractile stress in the cytoplasm. This induces osmotic pressure (cytoplasm is 80% water) and there is additional pressure due to polymerisation. We assume the cell complies to Newtonian dynamics and inertial terms are negligible (Lewis and Murray, 1991).

The model represents the actin filament network as a viscoelastic and contractile gel in the same way as (Lewis and Murray, 1991; Stephanou et al., 2004). The polymerisation kinetics, described in Section 1.2.2, mean that the filaments push on the membrane when

they polymerise. Conversely actomyosin contractions pull on the membrane. This causes cytoplasmic flows and increased pressure. At any given time the actin network is in mechanical equilibrium so we have the force balance mechanical equation:

$$\nabla \cdot (\boldsymbol{\sigma}_v + \boldsymbol{\sigma}_e + \boldsymbol{\sigma}_c + \boldsymbol{\sigma}_p) = 0, \tag{3.7}$$

where stress tensors are described as follows

- Viscous tensor $\boldsymbol{\sigma}_v(\mathbf{u})$: The viscous tensor is defined by $\boldsymbol{\sigma}_v = \mu_1 \frac{\partial \boldsymbol{\varepsilon}}{\partial t} + \mu_2 \frac{\partial \phi}{\partial t}\mathbf{I}$, where μ_1 and μ_2 are shear and bulk viscosities respectively, $\boldsymbol{\varepsilon}$ is the strain tensor ($\frac{1}{2}(\nabla \mathbf{u} + \nabla \mathbf{u}^T)$) and ϕ is the dilation ($\nabla \cdot \mathbf{u}$).

- Elastic tensor $\boldsymbol{\sigma}_e(\mathbf{u})$: The elastic tensor is defined by $\boldsymbol{\sigma}_e = \frac{E}{1+\nu}(\boldsymbol{\varepsilon} + \frac{\nu}{1-2\nu}\phi\mathbf{I})$, where E is the Young's modulus and ν is the Poisson ratio.

- Contractile tensor $\boldsymbol{\sigma}_c(a)$: Let the contractile tensor $\boldsymbol{\sigma}_c = \psi a^2 e^{-a/a_{sat}}\mathbf{I}$, where ψ is the contractility coefficient, and a_{sat} is the saturation coefficient of actin. This formulation means that the contractility increases parabolically with actin density until it reaches the saturation concentration then decreases exponentially due to compaction of the network.

- Pressure tensor $\boldsymbol{\sigma}_p(a, \mathbf{u})$: Let the pressure tensor $\boldsymbol{\sigma}_p = \dfrac{p}{1+\phi}\big(1 + \frac{2}{\pi}\delta(l)\arctan a\big)\mathbf{I}$. This describes two types of pressure. First is the hydrostatic pressure which is present everywhere and corresponds to the osmotic pressure in the cell which depends on the dilation ϕ and pressure coefficient p. Secondly, close to the membrane there is also polymerisation pressure caused by the polymerising actin filaments pushing on the cell membrane. This increases with increasing concentration of filaments a. We choose close to the membrane to mean less than 20% of the cell radius from the surface in the initial state. To define this we use $\delta(l)$ and the points $\boldsymbol{\xi} = (\xi_x, \xi_y, \xi_z) \in \boldsymbol{\Omega}_0$. There exists a family of bijective mappings between the initial and current domains we can let $l : \boldsymbol{\Omega}_t \times I \to \mathbb{R}$ and corresponding $\hat{l} : \boldsymbol{\Omega}_0 \times I \to [0, 1]$ then $\hat{l}(\boldsymbol{\xi}, t) = l(\boldsymbol{x}(\boldsymbol{\xi}, t), t)$. So we calculate the distance from the centroid by

$$\delta(l) = \begin{cases} 1, & \text{if } \sqrt{\xi_x^2 + \xi_y^2 + \xi_z^2} > 0.8, \\ 0, & \text{otherwise.} \end{cases} \tag{3.8}$$

Therefore far from the membrane, only the osmotic component exists while close to the membrane polymerisation reinforces osmotic stress. A representation of this is displayed in Figure 3.1

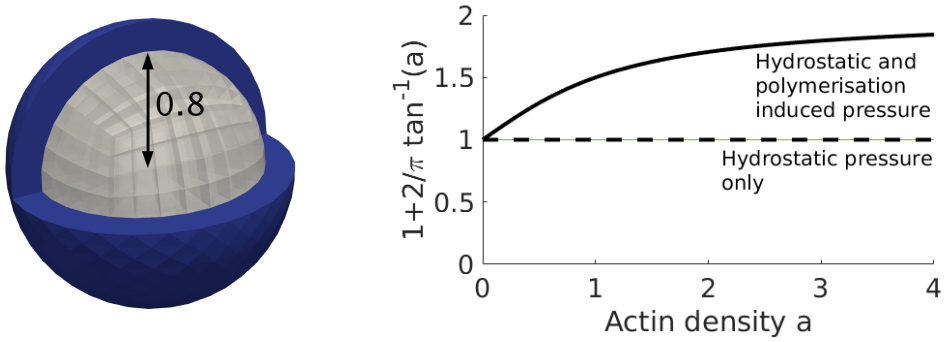

(a) (b)

Figure 3.1: Pictoral and graphical representation of the variation of pressure in the cell. (a) A 3-dimensional illustration where both the dark blue part shows where there is hydrostatic and polymerisation pressure, while the light shows the region where there is only the hydrostatic pressure. (b) Plot of how polymerisation pressure varies with the concentration of actin (letting $p = 1$ and $\phi = 0$).

3.4 A mechanobiochemical with a single actin reaction-diffusion equation

We have formulated a system of two equations which are interlinked. The solution to actin reaction-diffusion equation affects the contractile and pressure parts of the force balance equation and the displacement solution of the force balance equation drives the reaction-diffusion equation through the convection term and the changing shape of the domain.

We can now combine the equations to obtain the following system

$$\nabla \cdot (\boldsymbol{\sigma}_v + \boldsymbol{\sigma}_e + \boldsymbol{\sigma}_c + \boldsymbol{\sigma}_p) = \mathbf{0} \qquad \text{in } \boldsymbol{\Omega}_t, t \in I, \tag{3.9a}$$

$$\frac{\partial a}{\partial t} + \nabla \cdot (a\boldsymbol{\beta}) - D_a \Delta a - k_a(a_c - a) = 0 \qquad \text{in } \boldsymbol{\Omega}_t, t \in I, \tag{3.9b}$$

$$a(\boldsymbol{x}(t), t) = a_0, \quad \mathbf{u}(\boldsymbol{x}(t), t) = \mathbf{0} \qquad \text{for } \boldsymbol{x} \in \boldsymbol{\Omega}_0, \tag{3.9c}$$

$$\boldsymbol{\beta} = \boldsymbol{\omega}_n(\boldsymbol{x}) \qquad \text{for } \boldsymbol{x} \in \partial\boldsymbol{\Omega}_t, t \in I, \tag{3.9d}$$

$$\boldsymbol{\sigma}_v \cdot \mathbf{n} = \boldsymbol{\sigma}_e \cdot \mathbf{n} = \mathbf{n} \cdot \nabla a = 0 \qquad \text{for } \boldsymbol{x} \in \partial\boldsymbol{\Omega}_t, t \in I. \tag{3.9e}$$

For illustrative purposes, we assume that the initial domain is a unit sphere. Biologically, this corresponds to a cell just after mitosis. The initial condition for actin density is a small perturbation from the homogeneous steady state (when $a = a_c = 1$). The boundary conditions are zero-flux for the reaction-diffusion equation and stress-free for the force balance equation (3.9e). Other parameters are defined in Table 3.1. We will now examine

	Description	Form / Value	Reference
$\boldsymbol{\varepsilon}$	strain tensor	$\frac{1}{2}(\nabla\mathbf{u}+\nabla\mathbf{u}^T)$	
ϕ	dilation	$\nabla\cdot\mathbf{u}$	
$\boldsymbol{\beta}$	flow velocity	$\frac{\partial\mathbf{u}}{\partial t}$	
$\boldsymbol{\omega}_n$	normal velocity of boundary		
μ_1	shear viscosity	$96.15\frac{dyn\cdot s}{cm^2}$	Bausch et al. (1998)
μ_2	bulk viscosity	$250\frac{dyn\cdot s}{cm^2}$	Bausch et al. (1998)
E	Young's modulus	$1.5\frac{dyn\cdot s}{cm^2}$	Estimated George (2012)
ν	Poisson ratio	0.3	Estimated George (2012)
D_a	diffusion coefficient	$0.012\frac{cm^2}{s}$	Stephanou et al. (2004)
k_a	rate of polymerisation	$0.03s^{-1}$	Estimated George (2012)
a_c	conc. at equilibrium	$1\frac{mol}{cm^3}$ normalised	Derived in George (2012)
a_{sat}	saturation conc.	$1.4\frac{mol}{cm^3}$ normalised	Stephanou et al. (2004)
l_0	vicinity of the membrane	80% of cell radius	Estimated George (2012)
ψ	contractility coefficient	70	
p	pressure coefficient	1.7	

Table 3.1: Descriptions of parameters. ψ and p will be varied to select patterns.

linear stability when considering small perturbations around the uniform steady state.

3.5 Linear stability analysis of the mechanobiochemical model

We employ linear stability theory to identify key parameters and compute analytical solutions close to bifurcation points. It will validate the numerical scheme that we will use to find approximate solutions to the model problem. Close to the steady state, the problem can be approximated by a linear one. The method for the mechanobiochemical model is described in George et al. (2013) for the case of two dimensions, here we extend this analysis to 3-dimensions. Letting L be the typical radius of a cell, we use the following dimensionless quantities

$$\begin{cases} \tilde{t}=tk_a, & \tilde{a}=\frac{a}{a_c}=a, & \tilde{\mathbf{u}}=\frac{\mathbf{u}}{L}, & \tilde{\nabla}=L\nabla, & \tilde{\Delta}=L^2\Delta, \\ \tilde{a}_{sat}=\frac{a_{sat}}{a_c}=a_{sat}, & \tilde{p}=p\frac{1+\nu}{E}, & \tilde{\phi}=\phi, & \tilde{\boldsymbol{\varepsilon}}=\boldsymbol{\varepsilon}, & \tilde{\mu}_i=\mu_i k_a\frac{1+\nu}{E}, \\ \tilde{\psi}=\psi a_c^2\frac{1+\nu}{E}, & \tilde{\boldsymbol{\beta}}=\frac{\boldsymbol{\beta}}{k_aL}, & d=\tilde{D}_a=\frac{D_a}{k_aL^2}, & \tilde{l}_0=\frac{l_0}{L}. & \end{cases} \tag{3.10}$$

Substituting the appropriate scales above and using the dimensionless quantities defined, system (3.9) reduces to the following

$$\begin{cases} \tilde{\nabla}\cdot\Big[(\tilde{\mu}_1\tilde{\boldsymbol{\varepsilon}}_t+\mu_2\tilde{\phi}_t\mathbf{I})+(\tilde{\boldsymbol{\varepsilon}}+\frac{\nu}{1-2\nu}\tilde{\phi}\mathbf{I})+(\tilde{\psi}\tilde{a}^2e^{-\tilde{a}/\tilde{a}_{sat}}\mathbf{I})+ \\ \qquad\qquad \Big(\frac{\tilde{p}}{1+\tilde{\phi}}\big(1+\frac{2}{\pi}\delta(l)\arctan\tilde{a}\big)\mathbf{I}\Big)\Big]=0, \\ \frac{\partial\tilde{a}}{\partial\tilde{t}}+\tilde{\nabla}\cdot(\tilde{a}\tilde{\boldsymbol{\beta}})-d\tilde{\Delta}\tilde{a}=1-\tilde{a}. \end{cases} \tag{3.11}$$

We restrict our analysis by considering an initial volume which is a unit sphere. Furthermore, we assume that for a very short time, say $t_1>0$ such that $t_1=t_0+\Delta t<<1$ the deformed sphere is still very close to the initial unit sphere, i.e., $\boldsymbol{\Omega}_{t_1}\approx\boldsymbol{\Omega}_{t_0}$. This system has a steady state at $a_s=1,\ \mathbf{u}_s=\mathbf{0}$. Given small variations $\hat{a}$ and $\hat{\mathbf{u}}$ consider the perturbation from the steady state $\tilde{a}=a_s+\hat{a}=1+\hat{a}$ and $\tilde{\mathbf{u}}=\mathbf{u}_s+\hat{\mathbf{u}}=\hat{\mathbf{u}}$. Let $\sigma(a)=\psi a^2e^{-a/a_{sat}}$. Using Taylor expansion and neglecting all but the linear terms, we obtain the linearised partial differential equations

$$\begin{cases} \tilde{\nabla}\cdot\Big[(\tilde{\mu}_1\hat{\boldsymbol{\varepsilon}}_t+\mu_2\hat{\phi}_t\mathbf{I})+(\hat{\boldsymbol{\varepsilon}}+\frac{\nu}{1-2\nu}\hat{\phi}\mathbf{I})+\hat{a}\sigma'(1)\mathbf{I}+\tilde{p}(1-\hat{\phi})\mathbf{I}+\tilde{p}\frac{2}{\pi}\delta(l)\hat{a}\mathbf{I}\Big]=\mathbf{0}, \\ \frac{\partial\hat{a}}{\partial\tilde{t}}+\tilde{\nabla}\cdot(\hat{\beta})-d\tilde{\Delta}\hat{a}+\hat{a}=0, \end{cases} \tag{3.12}$$

where $\sigma'(1)=\frac{\partial\sigma(a)}{\partial a}|_{a=a_c}$. Next we look for solutions of the form $\hat{a}(\boldsymbol{x},t)=a^*e^{\lambda t+i\mathbf{k}\cdot\boldsymbol{x}}$ and $\hat{\mathbf{u}}(\boldsymbol{x},t)=\mathbf{u}^*e^{\lambda t+i\mathbf{k}\cdot\boldsymbol{x}}$ where λ and $\mathbf{k}$ represent the growth rate (also known as an eigenvalue) and the wave vector respectively, and assume that a^* and $\mathbf{u}^*$ are constants of proportionality. Inputting this into the nondimensionalised system leads to the dispersal relation,

$$\lambda(k^2)=\frac{-b(k^2)\pm\sqrt{(b(k^2))^2-4\tilde{\mu}k^2c(k^2)}}{2\tilde{\mu}k^2}, \tag{3.13}$$

where $b(k^2)=\tilde{d}k^2+1+\nu'+\tilde{\mu}-\sigma'(1)-\tilde{p}-\tilde{p}\frac{2}{\pi}\delta(l)$ and $c(k^2)=d(1+\nu'+\tilde{p})k^2+1+\nu'+\tilde{p}$. If $k^2=0$, the dispersal relation (3.13) is indeterminate so we consider only $k^2>0$. In order for there to be instability (i.e. modes to grow) we need $\lambda(k^2)>0$. This occurs if $b(k^2)<0$ or $c(k^2)<0$ or both. First considering $c(k^2)$ we can see that $\tilde{p}>1+\nu'\implies c(k^2)<0$, for all $k^2>0$. Next considering $b(k^2)$ and defining $G:=1+\nu'+\tilde{\mu}-\sigma'(1)-\tilde{p}-\frac{2}{\pi}\delta(l)$, we say that the necessary and sufficient conditions for growth of modes are (George et al., 2013):

- $G<0$,
- $\tilde{\mu}dk^2<|G|$,
- $k_1^2\leq k_{crit}^2=\frac{|G|}{\tilde{\mu}d}$.

In the last condition k_1^2 is the first positive wavenumber, this must be smaller than the value of k^2 where $b(k^2)$ is zero, to ensure there is a wavenumber in the region where $b(k^2)$ is negative. We see that the parameters affecting the sign of G are p and $\sigma'(1)$ which is proportional to ψ. Therefore we can vary p and ψ to isolate particular patterns/modes. Let $\mathbf{w}(\boldsymbol{x}) := (a(\boldsymbol{x}), \mathbf{u}(\boldsymbol{x}))^T$ denote the time independent eigenfunctions of the linear system (3.12). By considering only the spatial variations, we obtain the eigenvalue problem $\Delta \mathbf{w} = -k^2 \mathbf{w}$, thus the unstable modes will correspond to eigenfunctions of the Laplacian on the chosen domain, which in our case is the unit sphere $\mathbf{\Omega}_0 = \{(x, y, z) : x^2 + y^2 + z^2 \leq 1\}$.

We described how to find these eigenvalues, and eigenfunctions on the unit sphere (with homogeneous Neumann boundary condition) in Section 2.8.1. Following derivations in Section 2.8.1, there are an infinite number of discrete solutions of the form

$$w_{l,n}^m(r, \theta, \phi) = A_{l,n}^m J_{l+\frac{1}{2}}(j'_{l+\frac{1}{2},n} r) e^{im\phi} P_l^m(\cos\theta), \tag{3.14}$$

where l, m, n are all integers such that $|m| \leq l \leq n$, $A_{l,n}^m$ are constants, $J_\alpha(x)$ is a Bessel function of the first kind, i.e. $J_\alpha(x) = \sum_{j=0}^{\infty} \frac{(-1)^j}{j!\Gamma(1+j+\alpha)} \left(\frac{x}{2}\right)^{2j+\alpha}$ where $\Gamma(n) = (n-1)!$, $P_l^m(x)$ are associated Legendre polynomials, and $j'_{l+\frac{1}{2},n}$ are zeros of the differential of the spherical Bessel function. Using the approach described in Chapter 2, we compute the eigenvalues $k_{l,n}^2 = (j'_{l+\frac{1}{2},n})^2$ numerically. For each eigenvalue $\lambda_{l,n} = k_{l,n}^2$ there are $2l+1$ possible eigenfunctions. Figure 3.2 shows the eigenfunctions for some selected values of l, m and n. The wave numbers are discrete. Keeping all other parameters fixed as in Table 3.1 we can calculate the values of ψ which are required to make certain wavenumbers unstable. These are displayed in Table 3.2. Note that it is rarely possible to isolate just one eigenvalue and when $l \geq 1$ we have that each eigenvalue has many eigenfunctions so "mixed modes", which are a linear combination of eigenfunctions, will be common.

ψ	isolated wavenumbers
40	$k_{0,1}^2$
70	$k_{0,1}^2$, $k_{1,1}^2$
100	$k_{0,1}^2$, $k_{1,1}^2$, $k_{2,1}^2$
180	$k_{0,1}^2$, $k_{1,1}^2$, $k_{2,1}^2$, $k_{3,1}^2$
230	$k_{0,1}^2$, $k_{1,1}^2$, $k_{2,1}^2$, $k_{3,1}^2$, $k_{4,1}^2$

Table 3.2: The value of ψ required by the dispersal relation to isolate particular wavenumbers. Note that in the dispersal relation we use dimensionless $\tilde{\psi} = \psi a_c^2 \frac{1+\nu}{E}$.

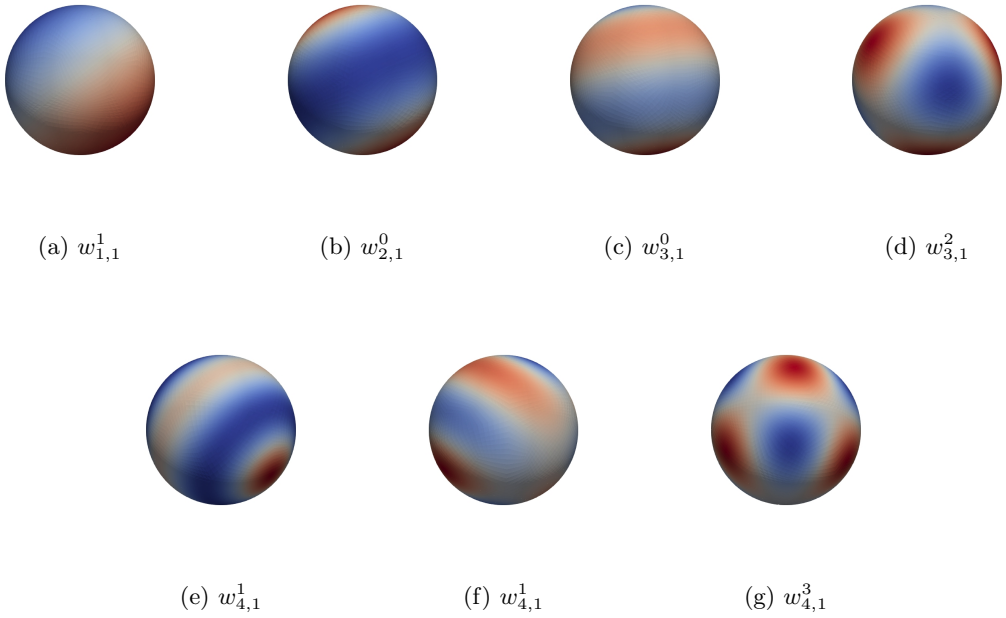

(a) $w^1_{1,1}$ (b) $w^0_{2,1}$ (c) $w^0_{3,1}$ (d) $w^2_{3,1}$

(e) $w^1_{4,1}$ (f) $w^1_{4,1}$ (g) $w^3_{4,1}$

Figure 3.2: Analytical solutions to the eigenvalue problem on the unit sphere i.e. (3.14) for selected values of l, m, n.

3.6 Numerical simulations for Model 1

As a first step, we computed numerical results in two dimensions following the work of George et al. (2013). We used the same finite element formulation but implemented it in the software library deal.II (Bangerth et al., 2016). Solving the actin and force balance equations on the unit disk over time, the results were found to be matching those reported by George et al. (results not shown for the sake of brevity), thereby giving us confidence that the numerical results are independent of the numerical method employed. We then proceeded to extend the numerical solutions into three dimensions using the finite element formulation as outlined in Appendix A. Note that the formulation in Appendix A includes myosin which is not yet considered in this Chapter therefore, we set myosin concentration $m = 1$ at all times (this makes reaction kinetics for actin $k_a(a_c - a)$ as required) and $c = 0$, then solve only for actin and displacement. In the same way as in two dimensions, we found it is possible to isolate modes and significant deformation is subsequently seen.

In this section, the results from linear stability of the last section are validated when $0 < t << 1$, this is possible because at that time the domain evolution from the unit sphere ($\mathbf{\Omega}_0$) is negligible. The time step $\Delta t = 10^{-3}$, unless otherwise stated. The finite element mesh has 8192 active cells and 27123 degrees of freedom. Initial perturbations of actin vary depending on which eigenmode we wish to excite but are always a small perturbation

from the steady state ($a = 1$) and include the variable *rand* which is a randomly generated number between 0 and 0.1. In all examples we continue computing the solution until the mesh is so deformed that the numerical method can no longer be used.

3.6.1 Excitation of eigenmodes

We solve the system over time, for varying ψ using the values from Table 3.2. We see that early in the simulations the modes are excited and are qualitatively similar to the eigenfunctions shown in Figure 3.2. When the geometry becomes deformed, linear stability no longer holds and the cell deforms significantly, generally with high displacement where actin concentration is high. In these simulations the displacement plotted is the magnitude of the vector $\mathbf{u} = (u(\boldsymbol{x}(t), t), v(\boldsymbol{x}(t), t), w(\boldsymbol{x}(t), t))^T$, i.e. $\sqrt{u^2 + v^2 + w^2}$.

Example 1 - $k_{0,1}$

The first eigenvalue is $\lambda = k_{0,1}^2 = 3.1416$. The eigenfunction is $w_{0,1}^0 = \frac{\sin(k_{0,1}r)}{k_{0,1}r}$. Choosing $\psi = 40$ isolates this mode. This eigenfunction depends only on r (the distance from the centre) and is monotonic between 0 and 1. We present numerical results with parameters chosen to excite $w_{0,1}^0$ in Figure 3.3. We can see that initially the solution looks like a scalar multiple of $w_{0,1}^0$. Subsequently this causes the cell to expand almost uniformly, the volume increase is shown in Figure 3.3(d).

Example 2 - $k_{2,1}$

Next, we select $k_{2,1}$ by choosing $\psi = 70$ and initial conditions $a(\boldsymbol{x}) = 1 + w_{2,0}^1(\boldsymbol{x}) \times rand$, and present this in Figure 3.4. The solution begins to resemble that of the corresponding eigenfunction $w_{2,1}^0$ (illustrated in Figure 3.2(b)) and then the cell expands in the y-direction. The cell pushes out significantly at both ends, where there is high actin concentration (in red), and resembles a cell just before mitosis. The displacement solutions are qualitatively similar to the actin solutions, therefore in the rest of this section, we only show the actin solutions.

Other modes

Choosing $\psi = 230$ means that the wavenumbers $k_{3,1}^2$ and $k_{4,1}^2$ can be excited (in addition to $k_{0,1}^2$, $k_{1,1}^2$ and $k_{2,1}^2$). $k_{3,1}^2$ and $k_{4,1}^2$ have 7 and 9 corresponding eigenfunctions, respectively. In order to encourage a particular mode $w_{l,1}^m$ to grow we choose initial perturbation $rand \times w_{l,1}^m$. Figures 3.5–3.9 show modes being selected and the subsequent large deformations.

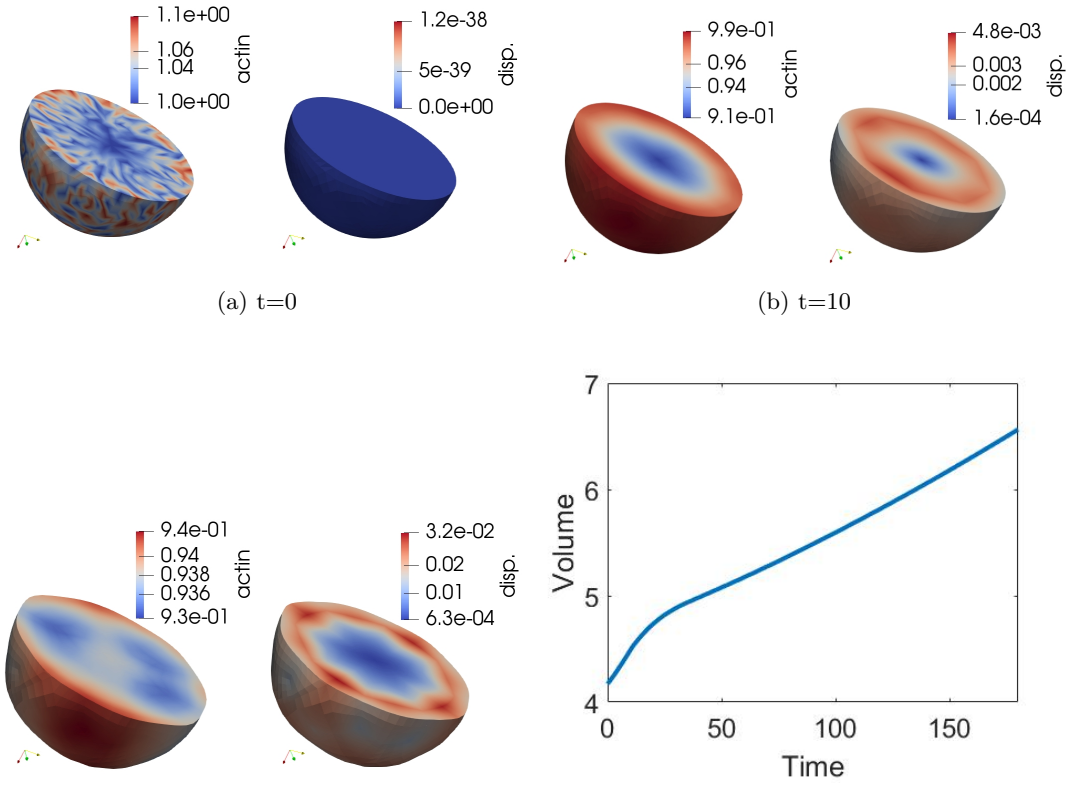

(a) t=0

(b) t=10

(c) t=180

(d) Change in volume

Figure 3.3: Selecting $k_{0,1}$. We cut the sphere in half so that at first we see the mode is excited and then the volume steadily increases over time. Actin concentration and displacement are higher in the vicinity of the membrane.

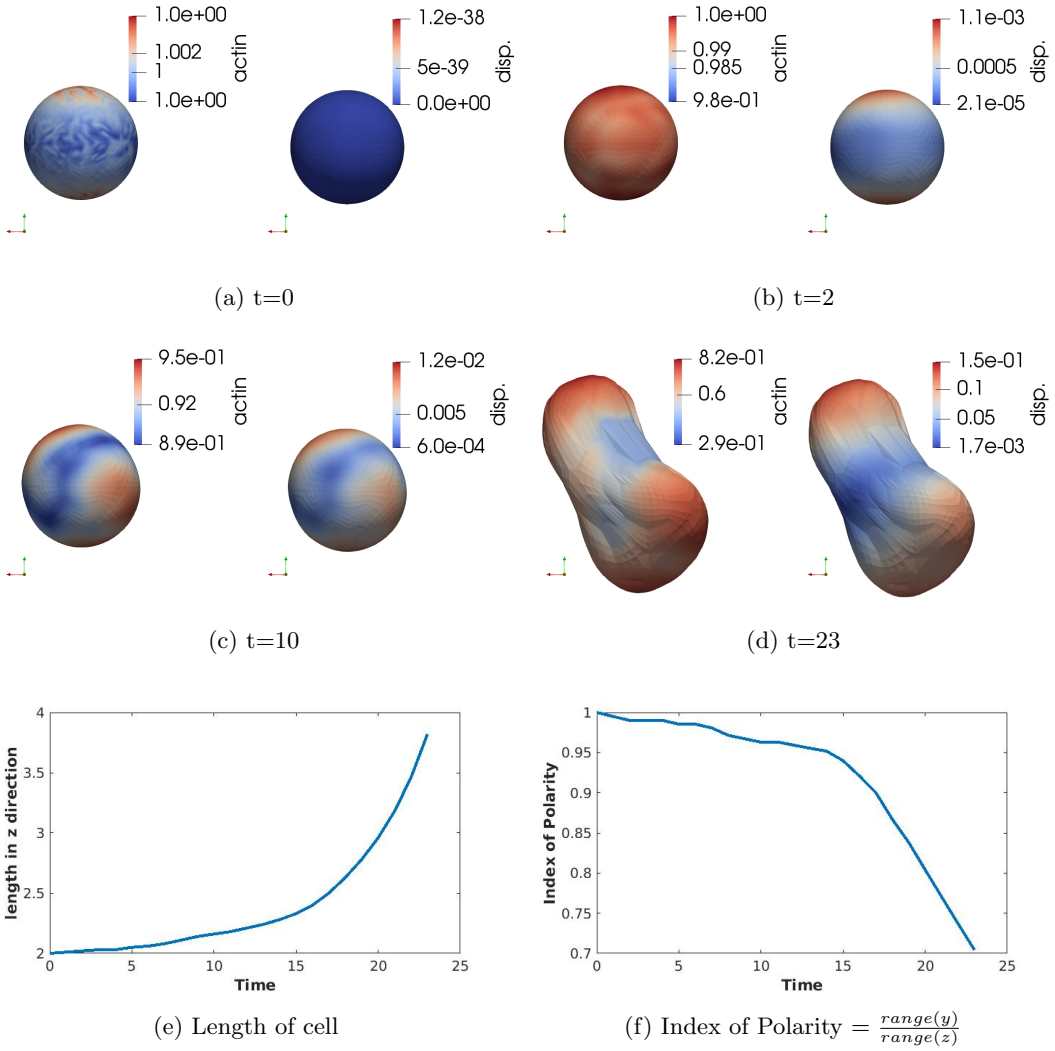

(a) t=0

(b) t=2

(c) t=10

(d) t=23

(e) Length of cell

(f) Index of Polarity = $\frac{range(y)}{range(z)}$

Figure 3.4: Selecting $w^0_{2,1}$. We see a significant elongation of the cell, predominantly in the z-direction, with actin concentration highest at the protruding ends.

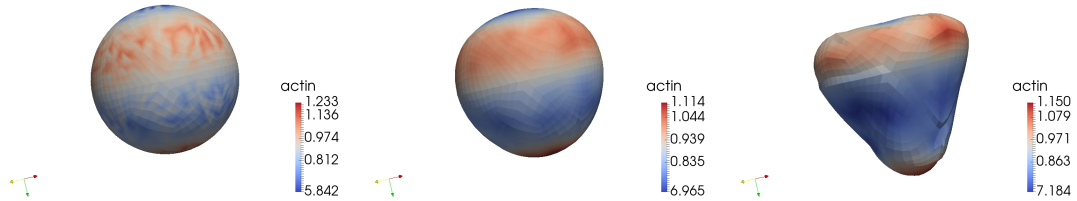

(a) t=0 (b) t=0.2 (c) t=1.2

Figure 3.5: Selecting $w^0_{3,1}$. The eigenfunction is shown in Figure 3.2(c).

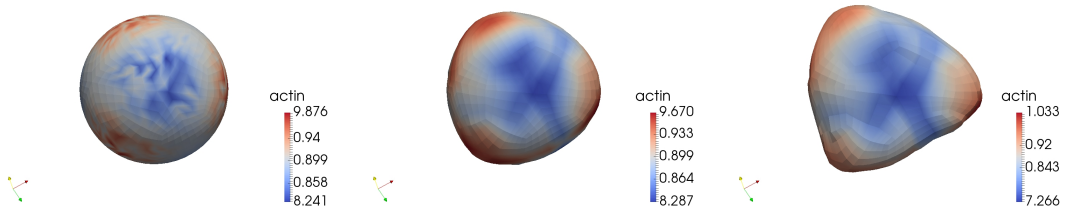

(a) t=0 (b) t=2 (c) t=4

Figure 3.6: Selecting $w^2_{3,1}$. The eigenfunction is shown in Figure 3.2(d).

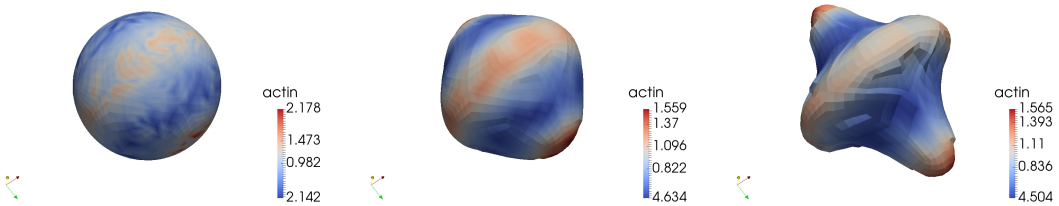

(a) t=0 (b) t=0.2 (c) t=0.8

Figure 3.7: Selecting $w^0_{4,1}$. The eigenfunction is shown in Figure 3.2(e).

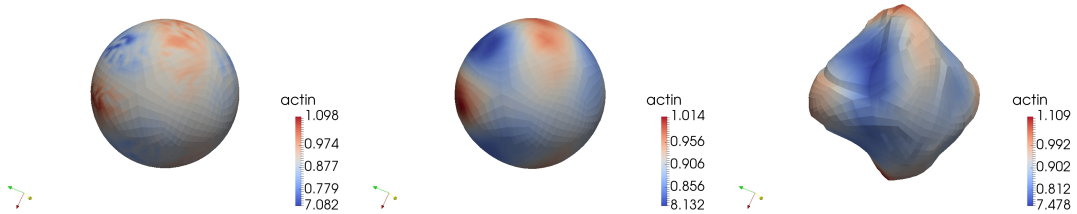

(a) t=0 (b) t=0.2 (c) t=3.2

Figure 3.8: Selecting $w^1_{4,1}$. The eigenfunction is shown in Figure 3.2(f).

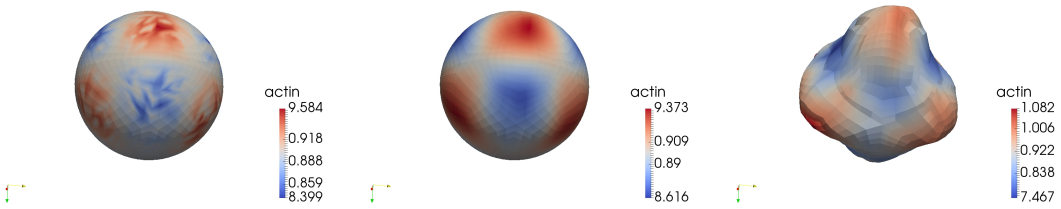

(a) t=0 (b) t=1 (c) t=7

Figure 3.9: Selecting $w^3_{4,1}$. The eigenfunction is shown in Figure 3.2(g).

The cell protrudes in areas of high actin concentration (shown in red) and contracts areas of low concentration (shown in blue). Figure 3.5(c) looks similar to some images of amoeboidal movement in literature (Petrie et al., 2012; Cao et al., 2016). Figure 3.7(c) displays two protrusions with high actin concentration and looks similar to lobopodia exploring before choosing a direction through an extracellular matrix (Chen et al., 2014).

Contraction

As a numerical experiment we can take pressure to be negative, $p = -0.5$ and $\psi = 70$. In this case the cell contracts as shown in Figure 3.10. Initial conditions for actin are $a = 1 + rand$, then as the cell contracts the actin concentration is highest in the centre and decreases towards the boundary. The decrease in volume is shown in Figure 3.10(d).

3.7 Summary

We have introduced the mechanobiochemical model in three dimensions. It is assumed that cell movement is a consequence of the protrusive and contractile properties of the actomyosin network, and the viscoelastic nature of the cytoplasm. The model consists of a reaction-diffusion equation for the concentration of actin and a force balance equation. The solution of the force balance equation gives the displacement of the cell. The displacement affects the reaction-diffusion equation due to a flow term and the changing domain shape, while the concentration of actin affects the contractile and pressure tensors in the force balance equation.

We considered linear stability analysis and identified the contractility coefficient ψ and the pressure p as key parameters whose value determines which wavenumbers will become unstable (George et al., 2013).

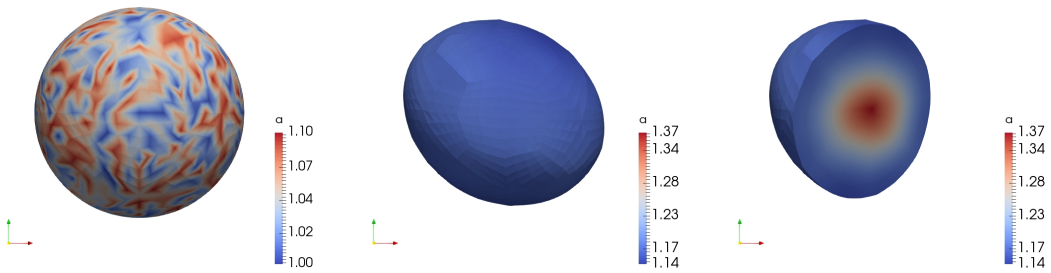

(a) t=0 (b) t=32 (c) t=32 cut through

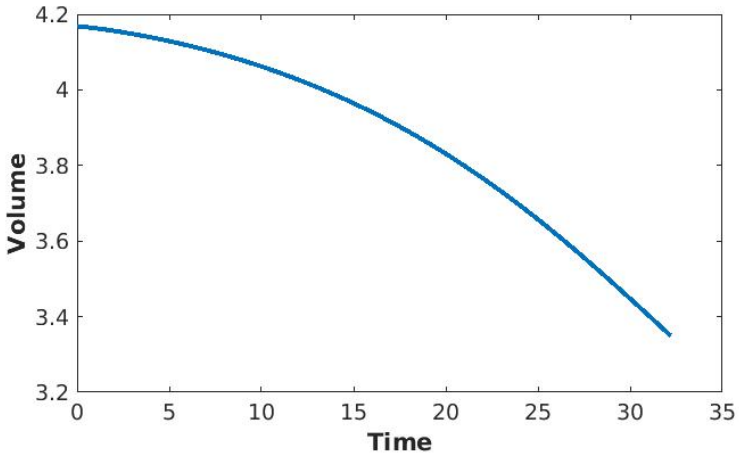

(d) Change in volume

Figure 3.10: Allowing pressure to be negative leads to contraction of the cell with the highest concentration of actin at the centre.

The numerical simulations are consistent with the predictions from linear stability theory in the early stages of movement. This validates the numerical scheme which is outlined and described in Appendix A. Subsequently we see significant deformations, some of which are consistent with shapes found in 3D experiments. In particular, we see expansion, contraction and changes in the index of polarity. The outward movement is most significant in areas with high actin concentration, in addition where there is higher curvature, higher actin concentration is observed.

We use the same parameter values as George (2012), in order to confirm that the mathematical and computational model works in three dimensions. A future work would likely benefit from finding relevant parameter values for 3D cells.

Although these results are promising, contraction is such a pivotal element of the system, and contraction is reliant on myosin. Hence, it is a logical next step to wish to model the concentration of myosin, and include this in the force balance equation. Since the myosin and actin have an effect on each other's concentration, and both "effectively" diffuse (see Section 4.2), we next propose a plausible reaction-diffusion system for actin and myosin, then couple this system to an updated force balance equation.

Chapter 4

Model 2: A 3D mechanobiochemical model with actin and myosin reaction-diffusion models

4.1 Introduction

In the previous chapter we saw that a mechanobiochemical model, with a single actin reaction-diffusion equation, for single cell migration could be extended into three dimensions. In this chapter we further extend the model to include the effect of the concentration of myosin. This involves adding a further reaction-diffusion equation for myosin, and subsequently the reaction kinetics between actin and myosin. Additionally, contraction due to myosin is represented by a new term in the force balance equation.

The reaction kinetics between actin and myosin are not rigorously known and F-actin and bound myosin do not diffuse in the way that free particles do. Nonetheless, many have modelled their spatially varying quantities with reaction-diffusion equations (Camley et al., 2017; Hawkins et al., 2011; Wolgemuth et al., 2011; Hodge and Papadopoulos, 2012; Gracheva and Othmer, 2004; Mogilner, 2009; Rubinstein et al., 2009). We have described some of their ideas in Section 1.4.2.

In this chapter, we describe the additions to the model of Chapter 3 and analyse stability of steady states. Before doing this for the full system we first consider the linear stability analysis on the stationary sphere for just the reaction-diffusion equations. This may allow us to identify diffusion-driven instability. Since we have a two component

system, and the domain is stationary, it can be nondimensionalised to the form we discuss in Chapter 2. This means we can investigate the standard conditions for diffusion-driven instability. We will discuss whether a Turing instability is necessary in the full system. We then explore linear stability in the full mechanobiochemical model. We present numerical simulations for both the reaction-diffusion system and the full system.

We first introduce the new equation and investigate plausible reaction-diffusion models describing the interactions between actin and myosin in 3D geometries.

4.2 Acto-myosin reaction-diffusion model

As in Chapter 3, we consider $\mathbf{\Omega}_t \subset \mathbb{R}^3$. For $t \in I = [0, T_f]$, $T_f > 0$, $\boldsymbol{x} = (x(t), y(t), z(t))$ describes a point in and $\mathbf{\Omega}_t$ and $a = a(\boldsymbol{x}(t), t)$ is the concentration of F-actin, at that point. We now introduce $m = m(\boldsymbol{x}(t), t)$ to be the concentration of bound myosin. The interactions between actin and myosin are described by the reaction terms $f(a, m)$ and $g(a, m)$ respectively. They describe the net formation of actin filaments or bound myosin due to the current concentrations of both F-actin or bound myosin. To define the equation we use the same method as in Section 3.2 but replacing $k_a(a_c - a)$ by the new reaction term $f(a, m)$. This gives us

$$\frac{\partial a}{\partial t} + \nabla \cdot (a\boldsymbol{\beta}) - D_a \Delta a = f(a, m). \tag{4.1}$$

We argue in the same way for the equation for myosin to obtain

$$\frac{\partial m}{\partial t} + \nabla \cdot (m\boldsymbol{\beta}) - D_m \Delta m = g(a, m), \tag{4.2}$$

where D_m is the diffusion coefficient for myosin. The boundary conditions are again zero-flux. It is worth noting that actin filaments do not diffuse significantly but globular actin does and since actin is continuously polymerising and depolymerising, the effect can be considered to be diffusive. Similarly, myosin is frequently binding and unbinding; when it is bound to actin, it simply moves with the filament, however "free" myosin diffuses very fast. Thus we consider this binding and unbinding effect to also be equivalent to diffusion. For simplicity, from now on we will simply refer to the variables as actin and myosin.

4.2.1 Hypothetical reaction kinetics

In order to define the functions $f(a, m)$ and $g(a, m)$ which represent reaction kinetics, we take into account the biological considerations discussed in Section 1.4.2. In particular, we propose that when the concentration of myosin is above equilibrium, this will cause the

concentration of actin to decrease, and the concentration of myosin to increase. Additionally when actin concentration is higher than equilibrium, this will cause actin to decrease and myosin to increase.

We investigated several plausible reaction kinetics. The implementation of this model means that these can easily be interchanged to consider different models. Kinetics which we will use for demonstration in this chapter are

$$f(a,m) = k_a(a_c - a) + k_{am}\frac{a^2(m_c - m)}{1 + Ka^2}, \tag{4.3a}$$

$$g(a,m) = -k_{ma}(a_c - a) - k_{am}\frac{a^2(m_c - m)}{1 + Ka^2}, \tag{4.3b}$$

where we begin with the same reaction term, $k_a(a_c - a)$, which we used in Chapter 3. G-actin polymerises at rate k_a into F-actin until the concentration of F-actin a reaches equilibrium concentration a_c and if the concentration is above this F-actin will depolymerise at the same rate. This formulation ensures that, if we set $m = 1$ everywhere in the domain, set $c = 0$, and neglect (4.2) we get model 1. Next, since myosin binds to actin the amount of myosin will increase due to higher concentration of actin, hence the term $-k_{ma}(a_c - a)$ where k_{ma} is the rate of binding/unbinding of myosin. Defining m_c as the unstable equilibrium concentration of m, the last term in the actin equation represents that actin will depolymerise with higher concentrations of myosin and is subject to a saturation coefficient K, for a. The negation is true for myosin, since myosin often accumulates.

4.3 Modelling myosin in the force balance equation

The main mechanical effect of myosin in a cell is contraction. Concentration of myosin is generally assumed to linearly affect the contractile force (Gracheva and Othmer, 2004; Wolgemuth et al., 2011; Rubinstein et al., 2009; Hodge and Papadopoulos, 2012; Shao et al., 2012; Murrell et al., 2015; Bendix et al., 2008). Thus we adjust the contractile tensor in the force balance equation to be

$$\boldsymbol{\sigma}_c = (\psi a^2 e^{-a/a_{sat}} + cm)\mathbf{I}. \tag{4.4}$$

We now have the full system,

$$\nabla \cdot (\boldsymbol{\sigma}_v + \boldsymbol{\sigma}_e + \boldsymbol{\sigma}_c + \boldsymbol{\sigma}_p) = \mathbf{0} \qquad \text{in } \boldsymbol{\Omega}_t, t \in I, \tag{4.5a}$$

$$\frac{\partial a}{\partial t} + \nabla \cdot (a\boldsymbol{\beta}) - D_a \Delta a - f(a,m) = 0 \qquad \text{in } \boldsymbol{\Omega}_t, t \in I, \tag{4.5b}$$

$$\frac{\partial m}{\partial t} + \nabla \cdot (m\boldsymbol{\beta}) - D_m \Delta m - g(a,m) = 0 \qquad \text{in } \boldsymbol{\Omega}_t, t \in I, \tag{4.5c}$$

$$a(\boldsymbol{x}(t),t) = a_0, \quad \mathbf{u}(\boldsymbol{x}(t),t) = \mathbf{0} \qquad \text{for } \boldsymbol{x} \in \boldsymbol{\Omega}_0, \tag{4.5d}$$

$$\boldsymbol{\beta} = \boldsymbol{\omega}_n \qquad \text{for } \boldsymbol{x} \in \partial\boldsymbol{\Omega}_t, t \in I, \tag{4.5e}$$

$$\boldsymbol{\sigma}_v \cdot \mathbf{n} = \boldsymbol{\sigma}_e \cdot \mathbf{n} = \mathbf{n} \cdot \nabla a = \mathbf{n} \cdot \nabla m = 0 \qquad \text{for } \boldsymbol{x} \in \partial\boldsymbol{\Omega}_t, t \in I, \tag{4.5f}$$

Thus the three equations are connected: the solutions to (4.5b) (actin concentration) and (4.5c) (myosin concentration) affect the contractile and pressure parts of the force balance equation and the solution to (4.5a) (displacement) affects the reaction-diffusion equations through the convection terms and the changing shape of the domain.

Similarly to Model 1, the initial domain is the unit sphere and initial conditions for actin and myosin densities are small perturbations from the homogeneous steady states (when $a = a_c = m = m_c = 1$). The boundary conditions are zero flux for the reaction-diffusion equations and stress free for the force balance equation (4.5f). We will now non-dimensionalise before considering linear stability for small perturbations from the steady state.

4.4 Non-dimensionalisation

We perform non-dimensionalisation to reduce parameters and simplify calculations. It also allows the reaction-diffusion equations to take the form necessary to use the standard conditions for diffusion-driven instability. We choose the example kinetics (4.3) and the nondimensionalised parameters:

$$\begin{cases} \tilde{t} = \dfrac{L^2}{D_a}t, \quad \tilde{a} = \dfrac{a}{a_c} = a, \quad \tilde{m} = \dfrac{m}{m_c} = m, \quad d = \dfrac{D_m}{D_a}, \quad \tilde{K} = \dfrac{K}{a_c}, \\ \gamma = \dfrac{L^2 k_a}{D_a}, \quad \tilde{k_{ma}} = \dfrac{k_{ma}}{k_a}, \quad \tilde{k_{am}} = \dfrac{k_{am}}{k_a}, \quad \tilde{k_m} = \dfrac{k_m}{k_a}, \quad \tilde{\Delta} = L^2\Delta, \\ \tilde{\nabla} = L\nabla, \quad \tilde{\mathbf{u}} = \dfrac{\mathbf{u}}{L}, \quad \tilde{\phi} = \phi, \quad \tilde{\boldsymbol{\varepsilon}} = \boldsymbol{\varepsilon}, \quad \tilde{p} = p\dfrac{1+\nu}{E}, \\ \tilde{\boldsymbol{\beta}} = \dfrac{\boldsymbol{\beta}L}{D_a}, \quad \tilde{a}_{sat} = \dfrac{a_{sat}}{a_c}, \quad \tilde{\psi} = \psi a_c^2 \dfrac{1+\nu}{E} \quad \tilde{\mu}_i = \dfrac{\mu_i D_a (1+\nu)}{EL^2}. \end{cases} \tag{4.6}$$

In the above, L is the typical radius of a cell. Substituting appropriately and carrying out algebraic manipulations leads to the following non-dimensionalised system

$$\tilde{\nabla}\cdot\Bigg[(\tilde{\mu}_1\tilde{\boldsymbol{\varepsilon}}_t+\mu_2\tilde{\phi}_t\mathbf{I})+(\tilde{\boldsymbol{\varepsilon}}+\frac{\nu}{1-2\nu}\tilde{\phi}\mathbf{I})+(\tilde{\psi}\tilde{a}^2e^{-\tilde{a}/\tilde{a}_{sat}}\mathbf{I})+\tilde{c}\tilde{m}\mathbf{I}+ \tag{4.7a}$$

$$\left(\frac{\tilde{p}}{1+\tilde{\phi}}\big(1+\frac{2}{\pi}\delta(l)\arctan\tilde{a}\big)\mathbf{I}\right)\Bigg]=0, \tag{4.7b}$$

$$\frac{\partial\tilde{a}}{\partial\tilde{t}}+\tilde{\nabla}\cdot(\tilde{a}\tilde{\boldsymbol{\beta}})-\tilde{\Delta}\tilde{a}-\gamma\left((1-\tilde{a})+\tilde{k_{am}}\frac{\tilde{a}^2(1-\tilde{m})}{1+\tilde{K}\tilde{a}^2}\right)=0, \tag{4.7c}$$

$$\frac{\partial\tilde{m}}{\partial\tilde{t}}+\tilde{\nabla}\cdot(\tilde{m}\tilde{\boldsymbol{\beta}})-d\tilde{\Delta}\tilde{m}-\gamma\left(-\tilde{k_{ma}}(1-\tilde{a})-\tilde{k_{am}}\frac{\tilde{a}^2(1-\tilde{m})}{1+\tilde{K}\tilde{a}^2}\right)=0. \tag{4.7d}$$

We are interested in what may cause instability and self-organisation of actin and myosin. To this end, we temporarily drop the force balance equation, leaving the coupled reaction-diffusion equations for actin and myosin.

4.5 Linear stability analysis of reaction-diffusion system

In the model of George (2012), the reaction-diffusion equation alone could not cause patterning. Without the flow term, the prescribed reactions meant the concentration of actin would always return to the homogeneous steady state of $a = a_c$. In our case we have two coupled reaction-diffusion equations which are well known to induce patterning in certain cases.

Without the force balance equation, we have a system of coupled reaction-diffusion equations on a stationary volume and $\tilde{\boldsymbol{\beta}} = 0$, so the equations are written in the standard form, (see Chapter 2 and, for example, Murray (2003)), i.e.:

$$a_t=\gamma f(a,m)+\Delta m,\quad m_t=\gamma g(a,m)+d\Delta m. \tag{4.8}$$

This means we can investigate the necessary conditions for diffusion-driven instability in the same way as in Section 2.4. In summary, (see (2.43)), we need

$$f_a+g_m<0,\qquad f_ag_m-f_mg_a>0, \tag{4.9a}$$

$$df_a+g_m>0,\qquad (df_a+g_m)^2-4d(f_ag_m-f_mg_a)>0, \tag{4.9b}$$

and k^2 in the range $k_-^2<k^2<k_+^2$ where

$$k_\pm^2=\gamma\frac{(df_a+g_m)\pm\sqrt{(df_a+g_m)^2-4d(f_ag_m-f_mg_a)}}{2d}. \tag{4.10}$$

We exploit this range to isolate particular patterns/modes. The unstable modes will correspond to the eigenfunctions of the Laplacian on the sphere and k^2 the associated eigenvalues.

We have non-dimensionalised equations

$$\frac{\partial \tilde{a}}{\partial \tilde{t}} - \tilde{\Delta}\tilde{a} = \gamma\left((1-\tilde{a}) + \tilde{k_{am}}\frac{\tilde{a}^2(1-\tilde{m})}{1+\tilde{K}\tilde{a}^2}\right), \tag{4.11a}$$

$$\frac{\partial \tilde{m}}{\partial \tilde{t}} - d\tilde{\Delta}\tilde{m} = \gamma\left(-\tilde{k_{ma}}(1-\tilde{a}) - \tilde{k_{am}}\frac{\tilde{a}(1-\tilde{m})}{1+\tilde{K}\tilde{a}^2}\right). \tag{4.11b}$$

There is a steady state when $\tilde{a} = \tilde{m} = 1$. In the reaction kinetics we have chosen, we have that $f_a = -1$, $f_m = -\frac{\tilde{k_{am}}}{1+\tilde{K}}$, $g_a = \tilde{k_{ma}}$ and $g_m = \frac{\tilde{k_{am}}}{1+\tilde{K}}$. Inputting these values into (4.9a) and (4.9b) gives the following conditions for diffusion-driven instability

$$d(1+\tilde{K}) < \tilde{k_{am}} < 1+\tilde{K}, \tag{4.12a}$$

$$1 < \tilde{k_{ma}} < \frac{(\frac{\tilde{k_{am}}}{1+\tilde{K}} + d)^2(1+\tilde{K})}{4d\tilde{k_{am}}}. \tag{4.12b}$$

Since we would like particular patterns to occur we isolate them using the dispersal relation (2.34), as in Chapter 2, using the appropriate $k^2_{l,n}$ which we found on the sphere.

4.5.1 Parameter selection

In Section 2.4, equation (2.34), we defined a dispersal relation $\lambda^2 + b(k^2)\lambda + c(k^2) = 0$, where $b(k^2) = k^2(1+d) - \gamma(f_a + g_m)$ and $c(k^2) = dk^4 - \gamma(df_a + g_m)k^2 + \gamma^2(f_a g_m - f_m g_a)$. There is instability if $\mathrm{Re}(\lambda > 0)$, where λ is the maximum root of this equation, therefore we can vary parameters in order to allow particular wavenumbers k^2 to be unstable.

In Figure 4.1, we use MATLAB to plot the maximum real part of λ against the wave number k^2. Since $\mathrm{Re}(\lambda > 0)$ means instability, these graphs can help us chose parameters: If the coloured line is above the x-axis for a particular wavenumber (labelled $k^2_{*,*}$ in Figure 4.1(a)), that wavenumber will be unstable when the varying parameter has the corresponding value. For example, in Figure 4.1(a), the saturation coefficient K is varied and we can see that $k^2_{1,1} = 2.0816$ will be unstable when $K = 4$ but no other wavenumbers will be. Similarly in 4.1(b) reaction constant k_{am} is varied, we see that $k_{am} = 0.08$ or 0.1 will allow just $k^2_{1,1}$ to be unstable but letting $k_{am} = 0.16$ leads to wavenumbers $k^2_{0,1}$, $k^2_{1,1}$, $k^2_{2,1}$ and $k^2_{3,1}$ all being unstable.

Next, in Figure 4.2 we fix $k^2 = k^2_{1,1} = 2.0816$ and vary k_{am}, K and d and plot in red when $Re(\lambda) > 0$. This shows the values which may cause a pattern similar to $w^1_{1,1}$ to grow. Unless otherwise stated, in these plots other parameter are fixed as: $d = 0.1, k_a = 0.04, k_{ma} = 0.05, k_{am} = 0.8, K = 2$.

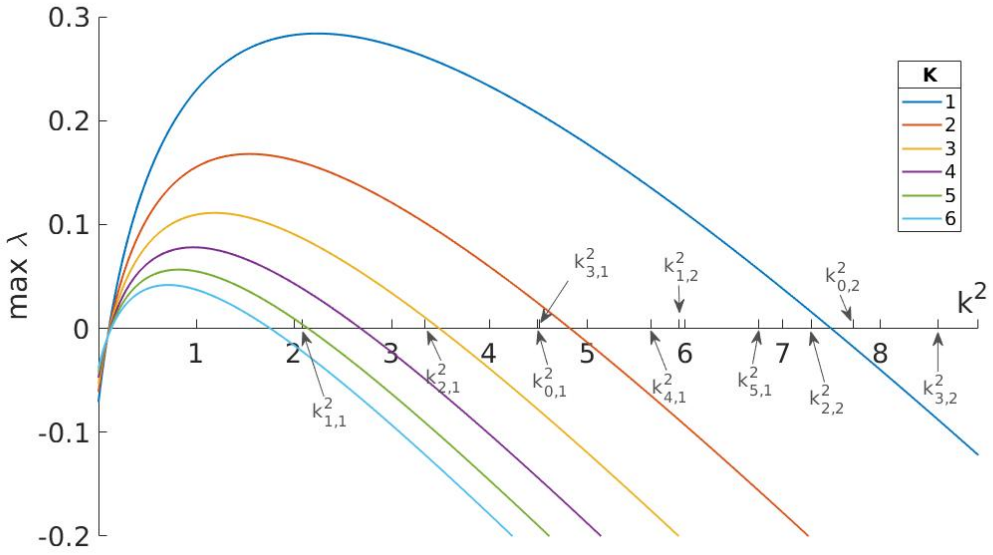

(a) The effect of varying K on max(Re(λ))

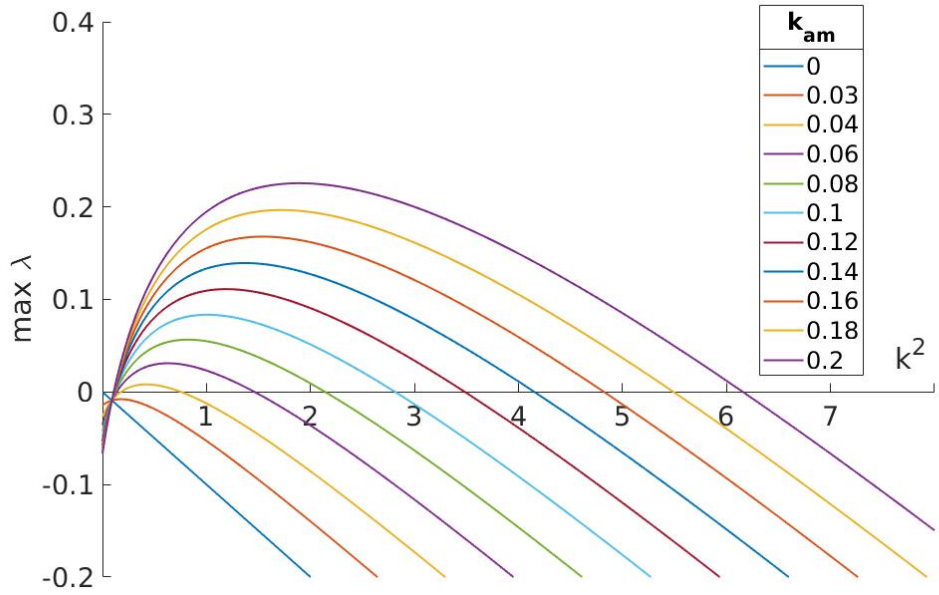

(b) The effect of varying k_{am} on max(Re(λ))

Figure 4.1: Plots of the maximum real part of the solutions to the dispersal relation against the wavenumber k^2. If $\mathrm{Re}(\lambda(k^2_{m,n})) > 0$, we have instability of the wavenumber $k^2_{m,n}$.

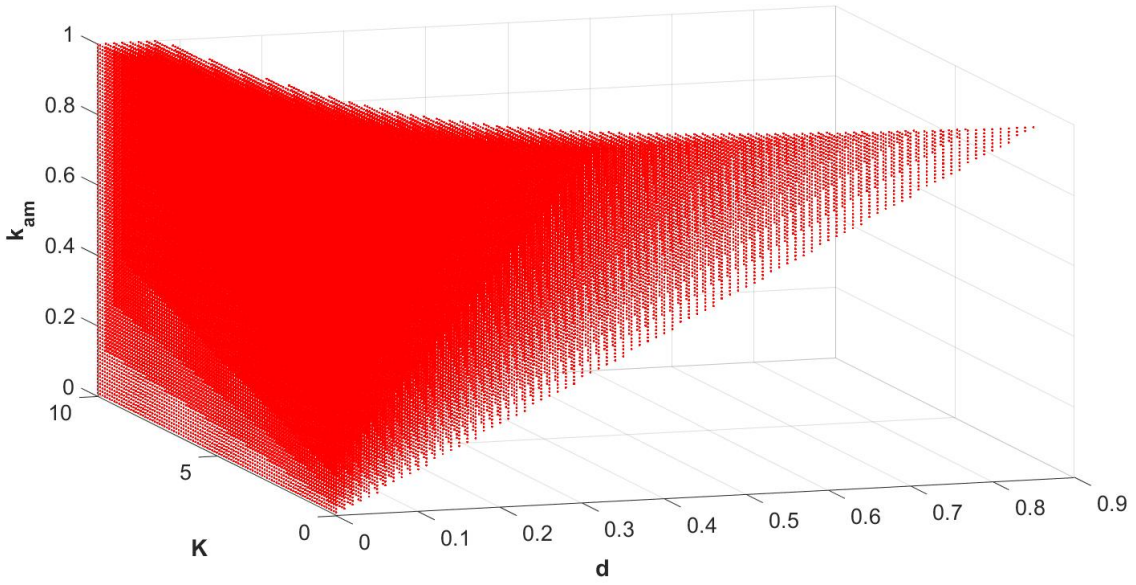

Figure 4.2: Plot to show the points in the parameter space (k_{am}, K, d) where $k^2_{1,1}$ is unstable.

4.6 Numerical simulations of the reaction-diffusion system

In Section 4.5.1 we saw that it was possible to choose parameters to isolate modes. Here we numerically solve the two equations on the fixed domain and observe modes growing. All modes can potentially be selected to grow by choosing appropriate conditions. The small initial perturbations always include a random component and are varied to encourage different modes to be dominant. Since for each eigenvalue $k^2_{l,n}$ there are $m = 2l + 1$ eigenfunctions, any one or a combination of two or more of these eigenfunctions may grow. If necessary, we can force a particular pattern to grow by multiplying the random component by that eigenfunction or something similar to it.

4.6.1 Excitation of mode $w^1_{1,1}$

In this example, the actin and myosin concentration solutions will be the negation of each other with actin concentration highest on one side and myosin concentration highest on the opposite side. This mode is the first eigenfunction that one might hope to see for the organisation of actin and myosin in a cell because it is similar to what is often observed in a moving cell. $k^2_{1,1} = 2.0816$ is also the lowest eigenvalue. We can see the growth of this eigenmode on the left hand side of Figure 4.3. We plot the concentrations of actin a and myosin m at times $t = 0, 1, 175$. The initial conditions are a small random perturbation from $a(\boldsymbol{x}) = m(\boldsymbol{x}) = 1$. Parameter values are $k_a = 0.04$, $k_{ma} = 0.05$ and $k_{am} = 0.12$.

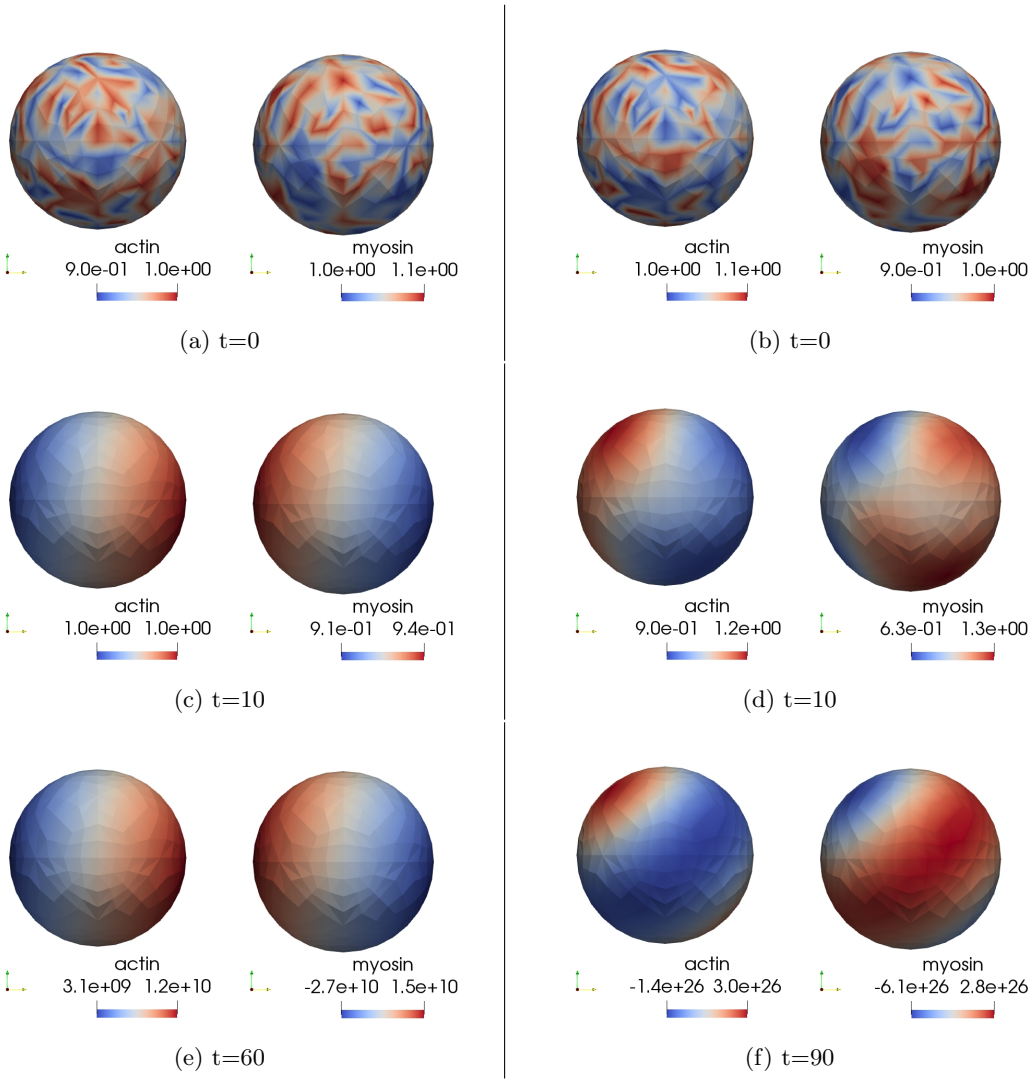

(a) t=0 (b) t=0

(c) t=10 (d) t=10

(e) t=60 (f) t=90

Figure 4.3: Graphical displays of the actin and myosin concentrations i.e. numerical solutions to the reaction-diffusion system. The same parameter values are used but with different initial conditions, as described in Table 4.1. On the left $w^1_{1,1}$ grows while on the right, $w^0_{2,1}$ grows.

Subsection	4.6.1	4.6.2	4.6.2	4.6.3
Figure	4.3	4.3	4.4	4.4
$a(\boldsymbol{x}, 0)$	$1 - ran$	$1 + ran$	$1 + w_{2,0}(\boldsymbol{x}) \times ran$	$1 - w_{2,0}(\boldsymbol{x}) \times ran$
$m(\boldsymbol{x}, 0)$	$1 + ran$	$1 - ran$	$1 + w_{2,0}(\boldsymbol{x}) \times ran$	$1 - w_{2,0}(\boldsymbol{x}) \times ran$
k_a	0.04	0.04	0.05	0.06
k_{ma}	0.05	0.05	0.06	0.09
k_{am}	0.12	0.12	0.07	0.15

Table 4.1: Initial conditions and parameters for simulations in this section.

The simple first mode is not the only organisation which makes sense or shows similarities to organisation seen in cells. The cell can protrude in more than one direction because of actin accumulation at both ends, or deform in many other ways. Alternatively, myosin could accumulate and "squeeze" on both sides. Therefore we continue by isolating other modes. We see that both the parameters and the initial conditions have an effect on which mode will grow.

4.6.2 Excitation of mode $w^0_{2,1}$

We see that it is possible to excite the mode $w^0_{2,1}$, in two different cases, shown in Figures 4.3 and 4.4. In Figure 4.3 the same parameters are used for both simulations but with different initial conditions. Conversely, in 4.4, the same initial conditions but different parameter values are used.

4.6.3 Excitation of mode $w^0_{3,1}$

On the right hand side of Figure 4.4 we see the isolation of $w^0_{3,1}$. The same initial conditions are used in Figures 4.4a and 4.4b but reaction constants are different as described in Table 4.1. If random initial conditions are used, for the parameters in the final column, the resultant pattern is a linear combination of the modes $w^n_{3,1}$ such that $n \in \{-3 : 1 : 3\}$ and the growth is highly asymmetrical.

4.6.4 Contrast to Chapter 2

One of the key features of the simulations in Chapter 2 is that a pattern quickly grows but this growth slows to a stop due to the bounding effects of the nonlinear terms, and we have a spatially inhomogeneous steady state known as a Turing pattern. We do not observe this slowing down with the kinetics we have chosen, this is likely because the

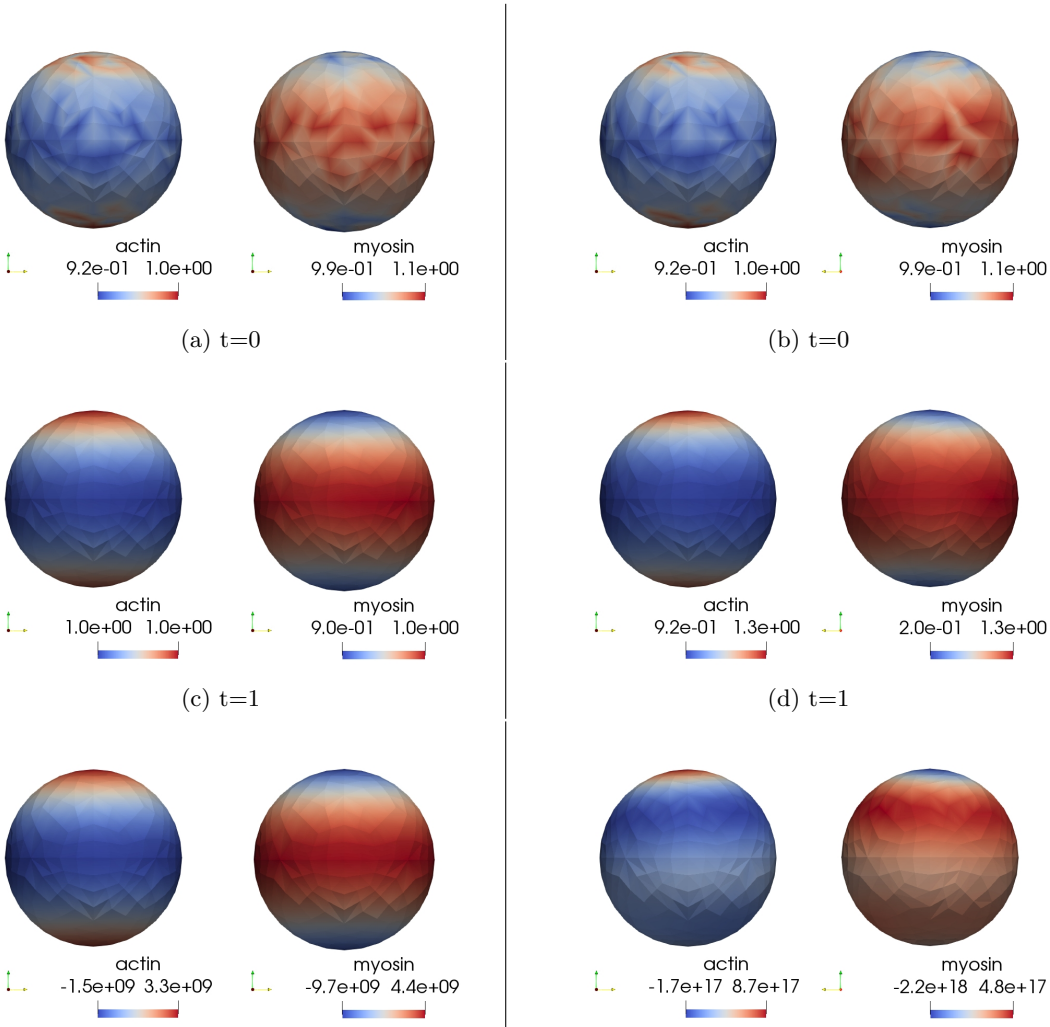

(a) t=0 (b) t=0

(c) t=1 (d) t=1

(e) t=10 (f) t=6

Figure 4.4: Graphical displays of the actin and myosin concentrations. Both simulations have the same initial conditions but on the left reaction constants are chosen to excite the mode $w^0_{2,1}$ and one the right for $w^0_{3,1}$.

nonlinear terms are not of the appropriate form. Because of this unbounded growth, we cannot call these Turing patterns as before. The modes are growing towards plus and minus infinity until the solver can no longer cope with the large numbers. We plot the L_2 norm of the difference between time steps in Figure A.1 (page 116) for the Example 4.6.2. In this, (and other examples in Section 4.6), the difference between successive solutions grows exponentially. The situation of unbounded growth of a mode is not realistic because concentrations become negative. Further work into nonlinear analysis of this, and similar systems, could give insight into biologically plausible kinetics which could produce spatially inhomogeneous steady states. However when coupled with the force balance equation, the full system does not give rise to negative concentrations so the full system may still be realistic.

4.7 Linear stability analysis of full system

So we now can predict when patterns will occur due to diffusion when the domain is stationary but what movements does this produce? And what effect does this movement have on the concentrations and distribution of actin and myosin? To address this we need to analyse the full system (4.5). The full nondimensionalised system, (with general kinetics), is

$$\frac{\partial \tilde{a}}{\partial \tilde{t}} + \tilde{\nabla}\cdot(\tilde{a}\tilde{\boldsymbol{\beta}}) - \tilde{\Delta}\tilde{a} - \gamma f(\tilde{a},\tilde{m}) = 0, \tag{4.13a}$$

$$\frac{\partial \tilde{m}}{\partial \tilde{t}} + \tilde{\nabla}\cdot(\tilde{m}\tilde{\boldsymbol{\beta}}) - d\tilde{\Delta}\tilde{m} - \gamma g(\tilde{a},\tilde{m}) = 0, \tag{4.13b}$$

$$\tilde{\nabla}\cdot\left[(\tilde{\mu}_1\tilde{\boldsymbol{\varepsilon}}_t + \mu_2\tilde{\phi}_t\mathbf{I}) + (\tilde{\boldsymbol{\varepsilon}} + \nu'\tilde{\phi}\mathbf{I}) + \sigma(\tilde{a})\mathbf{I} + \tilde{c}\tilde{m}\mathbf{I} + \frac{\tilde{p}(\tilde{a})}{1+\tilde{\phi}}\mathbf{I}\right] = 0, \tag{4.13c}$$

where $\sigma(\tilde{a}) = \tilde{\psi}\tilde{a}^2 e^{-\tilde{a}/\tilde{a}_{sat}}$, $\nu' = \frac{\nu}{1-2\nu}$ and $\tilde{p}(\tilde{a}) = \tilde{p}\big(1 + \frac{2}{\pi}\delta(l)\arctan\tilde{a}\big)$. We choose only f and g such that system has a steady state at $a_s = 1$, $m_s = 1$, $\mathbf{u}_s = \mathbf{0}$. Given small variations $\hat{a}, \hat{m}$ and $\hat{\mathbf{u}}$, consider the perturbation from the steady state $\tilde{a} = a_s + \hat{a} = 1 + \hat{a}$, $\tilde{m} = m_s + \hat{m} = 1 + \hat{m}$, $\tilde{\mathbf{u}} = \mathbf{u}_s + \hat{\mathbf{u}} = \hat{\mathbf{u}}$. This results in the linear system

$$\frac{\partial \hat{a}}{\partial \tilde{t}} + \tilde{\nabla}\cdot(\hat{\beta}) - \tilde{\Delta}\hat{a} - \gamma f_a\hat{a} - f_m\hat{m} = 0, \tag{4.14a}$$

$$\frac{\partial \hat{m}}{\partial \tilde{t}} + \tilde{\nabla}\cdot(\hat{\beta}) - d\tilde{\Delta}\hat{m} - \gamma g_a\hat{a} - g_m\hat{m} = 0, \tag{4.14b}$$

$$\tilde{\nabla}\cdot\left[(\tilde{\mu}_1\hat{\boldsymbol{\varepsilon}}_t + \tilde{\mu_2}\hat{\phi}_t\mathbf{I}) + (\hat{\boldsymbol{\varepsilon}} + \nu'\hat{\phi}\mathbf{I}) + \hat{a}\sigma'(1)\mathbf{I} + c\hat{m}\mathbf{I} + \tilde{p}(1-\hat{\phi})\mathbf{I} + \tilde{p}\frac{2}{\pi}\delta(l)\hat{a}\mathbf{I}\right] = \mathbf{0}. \tag{4.14c}$$

We now look for solutions of the form

$$\hat{a}(\boldsymbol{x},t) = a^* e^{\lambda t + \mathrm{i}\mathbf{k}\cdot\boldsymbol{x}},\ \hat{m}(\boldsymbol{x},t) = m^* e^{\lambda t + \mathrm{i}\mathbf{k}\cdot\boldsymbol{x}} \text{ and } \hat{\mathbf{u}}(\boldsymbol{x},t) = \mathbf{u}^* e^{\lambda t + \mathrm{i}\mathbf{k}\cdot\boldsymbol{x}}, \tag{4.15}$$

where λ is the growth rate, $\mathbf{k}$ is the wave vector, and a^*, m^* and $\mathbf{u}^*$ are small amplitudes. $e^{\lambda t + \mathrm{i}\mathbf{k}\cdot\boldsymbol{x}}$ will cancel and the equations become

$$\begin{aligned}
\lambda a^* + \lambda \mathrm{i} k \mathbf{u}^* + k^2 a^* - \gamma f_a a^* - \gamma f_m m^* &= 0, \\
\lambda m^* + \lambda \mathrm{i} k \mathbf{u}^* + d k^2 m^* - \gamma g_a a^* - \gamma g_m m^* &= 0, \\
-\tilde{\mu} k^2 \lambda \mathbf{u}^* - k^2(1-\nu')\mathbf{u}^* + \mathrm{i} k \sigma'(1) a^* + c\mathrm{i} k m^* + \tilde{p} k^2 \mathbf{u}^* + \mathrm{i} k \tilde{p} \frac{2}{\pi} \delta(l) a^* &= 0,
\end{aligned}$$

where $k = |\mathbf{k}|$ and $\tilde{\mu} = \tilde{\mu_1} + \tilde{\mu_2}$. We require solutions to be non-trivial and so we obtain the stability matrix

$$\begin{vmatrix}
\lambda + k^2 - \gamma f_a & -\gamma f_m & \lambda \mathrm{i} k \\
-\gamma g_a & \lambda + d k^2 - \gamma g_m & \lambda \mathrm{i} k \\
-\mathrm{i} k \sigma'(1) - \mathrm{i} k \tilde{p} \frac{2}{\pi} \delta(l) & -c\mathrm{i} k & \tilde{\mu} k^2 \lambda + k^2(1+\nu') - \tilde{p} k^2
\end{vmatrix} = 0, \tag{4.17a}$$

$$\implies (f(\lambda) :=) \mu \lambda^3 + a(k^2)\lambda^2 + b(k^2)\lambda + c(k^2) = 0, \tag{4.17b}$$

$$\text{where } a(k^2) = k^2(1+d) - \gamma(f_a + g_m) + 1 + \nu' - p - c - (\sigma'(1) + \tilde{p}\frac{2}{\pi}\delta(l)), \tag{4.17c}$$

$$b(k^2) = \tilde{\mu}(k^2 - \gamma f_a)(d k^2 - \gamma g_m) + (1 + \nu' + p)(k^2(1+d) - \gamma(f_a + g_m)) \tag{4.17d}$$

$$-c(k^2 + \gamma(-f_a + g_a)) + (\sigma'(1) + \tilde{p}\frac{2}{\pi}\delta(l))(\gamma(f_m + g_m) - d k^2) - \gamma^2 \tilde{\mu} f_m g_a, \tag{4.17e}$$

$$\text{and } c(k^2) = (1 + \nu' + p)\left((k^2 - \gamma f_a)(d k^2 - \gamma g_m) - \gamma^2 f_m g_a\right). \tag{4.17f}$$

Thus $f(\lambda) = 0$ (4.17b) is our new dispersal relation and we are concerned with the solutions $\lambda_{1,2,3}$. The sign of the real parts, and the existence of the imaginary parts, of $\lambda_{1,2,3}$ determine whether patterns occur, and if they are oscillatory in time and/or space.

4.7.1 Choosing parameters for instability

We can classify instabilities using the real and imaginary parts of the roots of the dispersal relation (Cross and Hohenberg, 1993; Yang et al., 2002). In Section 4.5, when considering the two component reaction-diffusion system, we showed the conditions necessary for Turing instability. Conditions given in equation (4.9b) ensure that we had $\mathrm{Im}(\lambda(k) = 0)\ \forall k$ and then it was possible to investigate for which k, $\mathrm{Re}(\lambda(k) > 0)$. In summary, Turing instability occurs when all $\lambda_i \in \mathbb{R}$ and at least one is positive. This produces stationary patterns which are inhomogeneous in space.

If we now allow solutions to be complex, we can also encounter patterns which vary in time. Hopf instability occurs when a pair of solutions, say $\lambda_{1,2}$, are contained in $\mathbb{C} \setminus \mathbb{R}$ and $\mathrm{Re}(\lambda_{1,2}) > 0$, in this case we can see patterns in time and space.

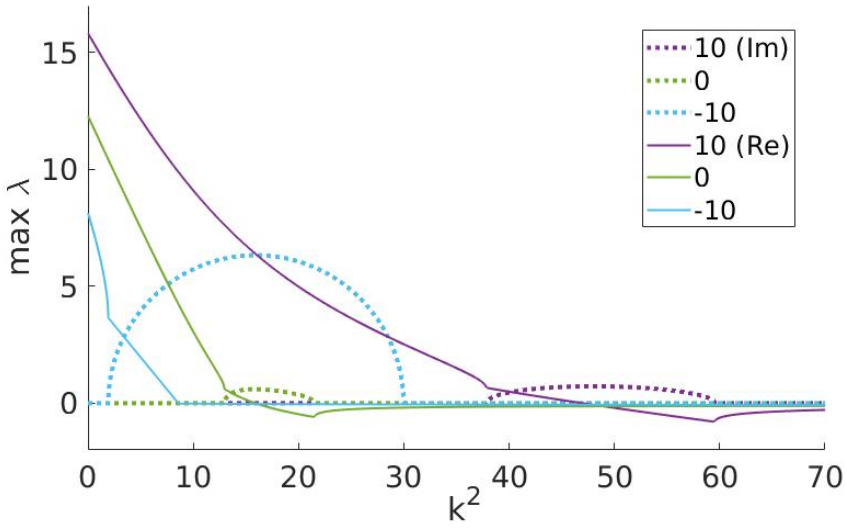

Figure 4.5: Plot to show maximum real (solid line) and imaginary (dotted line) parts of the solution to the dispersal relation. The three colours are denote three different values of c.

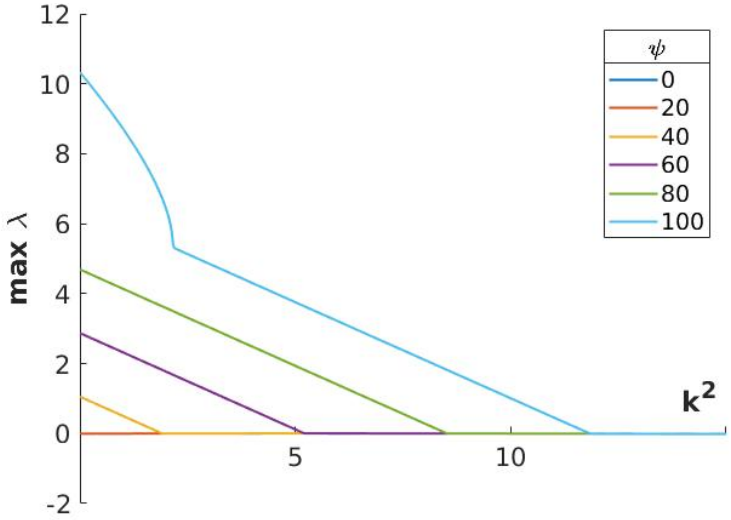

Figure 4.6: Plot to show maximum real part of λ as ψ is varied.

When we consider the full system, the conditions on the positivity of the roots are numerous and the coefficients of the polynomial are burdensome. Therefore, we numerically find these roots and observe the real and imaginary parts. We found that contractility due to myosin (c), and due to actin (ψ) are particularly significant for finding unstable wavenumbers. In Figure 4.5 we plot the real and imaginary parts of the solution against k^2 for three different values of c. We can see that when wavenumbers k^2 are less than ~ 8.5, $max\big(\mathrm{Re}(\lambda)\big) > 0$ for all three values of c, therefore the wavenumbers will be unstable. Additionally these wavenumbers will be have time oscillations when $c = 10$. There are also intervals of k^2 with Hopf instability for all three values of c. In Figure 4.6 we fix other parameters and vary ψ to see that, just like in Chapter 3 higher values of ψ mean higher wavenumbers can be excited.

4.7.2 Is diffusion-driven instability necessary for single cell migration?

In the model of George (2012) there is no instability without the force balance equation. The reaction term used means that, on a stationary domain, the solutions always return to the equilibrium concentration. Once the force balance equation is incorporated, the movement of the grid causes instability. In this section we have seen that it is possible to meet the conditions for diffusion-driven instability, however, in Section 3.6 we observe that the patterns which occur do not become stationary patterns (in fact they grow without bound) so are not Turing instabilities. Choosing appropriate kinetics for actin and myosin, it will be possible to find stationary Turing patterns.

We do not believe it is necessary to have stationary patterns in our biological modelling because although some steadily moving cells appear to have reasonably constant concentrations, this is not always the case. Further, it may be preferable to have conditions such that there is no instability on stationary domain and that instability comes from the force balance equation. This would mean that, on a stationary domain the concentrations of actin and myosin always return to a stable homogeneous equilibrium state rather than self-organise into patterns.

4.8 Numerical simulations for Model 2

We now present simulations of our full mechanobiochemical model. The aim is to find organisation of proteins into regions which will cause the cell to move. This organisation may be caused by diffusion-driven instability, or due to the movement of the cell combined with the reaction-diffusion equations. The linear stability analysis of Section 4.7 holds true

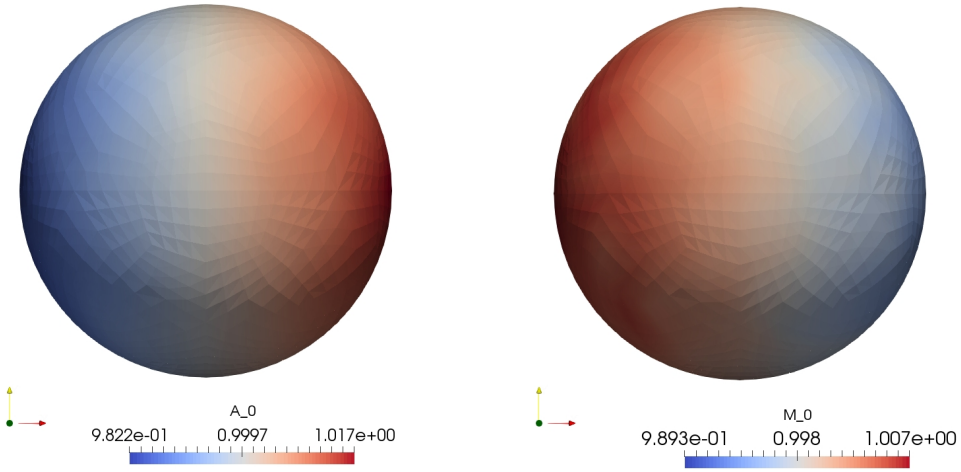

Figure 4.7: Graphical displays of the actin and myosin concentrations at time $t = 1$. These are numerical solutions to the full system (4.5) using the finite element formulation (A.35), as described in Section 4.8.1.

close to critical bifurcation points, these include parameters as well as the geometrical deformation of the cell. As we observed in Section 4.7 the conditions for stability are more numerous than when simply considering reaction-diffusion equations. In Section 4.7.1 we described that instability can affect patterns in time, space or both. We attempt to choose parameters so that particular modes will be selected. When we consider longer time, and therefore far away from equilibrium, linear stability theory no longer holds but we see significant protrusions and contractions which deform the mesh into many different shapes. Parameters used are in Table 4.2.

4.8.1 Excitation of mode $w^1_{1,1}$

We begin with the simplest mode. Choosing parameters $\psi = 20$, $c = -80$, $k_a = 0.04$, $k_{ma} = 0.05$ and $k_{am} = 0.06$ and initial conditions

$$a(\boldsymbol{x}, 0) = 1 + w^1_{1,1}(\boldsymbol{x}) \times ran, \quad m(\boldsymbol{x}, 0) = 1 - w^1_{1,1}(\boldsymbol{x}) \times ran,$$

we observe that the mode $w^1_{1,1}$ is selected for actin and myosin. In Figure 4.7 we plot the concentrations of actin and myosin at time $t = 1$. Blue indicates where the concentration is low, while red indicates that concentration is high. In this case very little deformation is seen.

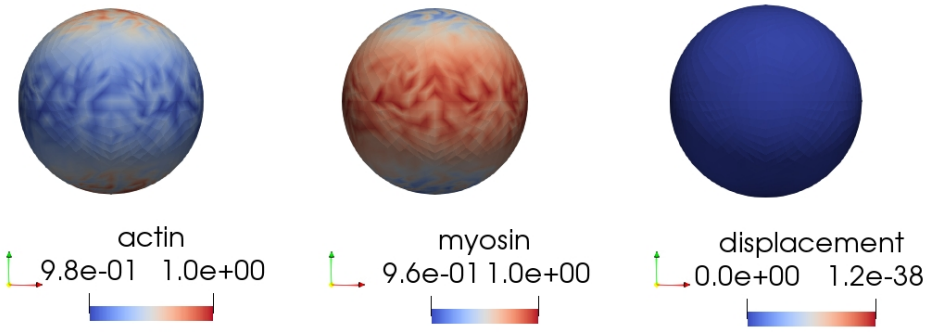

(a) t=0

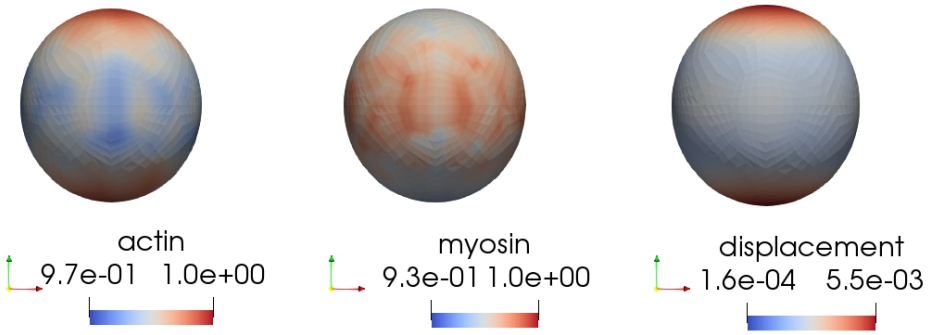

(b) t=1

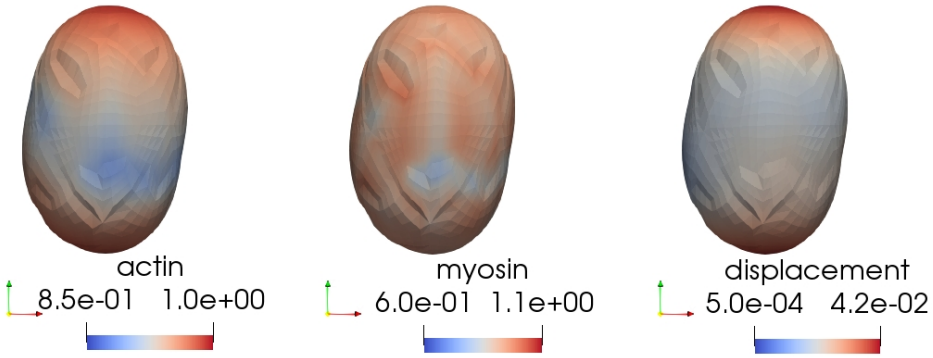

(c) t=6.3

Figure 4.8: Graphical displays of the actin and myosin concentrations, and the displacement at increasing time t, for the conditions described in Section 4.8.2. There is high actin at two ends, and high myosin in the middle. We then see in (c) that the cell squeezes in the middle stretches in the two directions of higher actin.

4.8.2 Cell deformation when $w^0_{2,1}$ is excited initially

The first large deformation is seen when choosing initial conditions

$$a(\boldsymbol{x}, 0) = 1 + w^0_{2,1}(\boldsymbol{x}) \times ran, \quad m(\boldsymbol{x}, 0) = 1 - w^0_{2,1}(\boldsymbol{x}) \times ran.$$

In Figure 4.9 we plot the concentrations of actin and myosin and the norm of the displacement ($|\mathbf{u}| = \sqrt{u^2 + v^2 + w^2}$). The cell expands at the two ends where actin concentration is high and contracts in the middle where myosin concentration is high. So far the results are visually similar to Model 1, one difference is that there is only a very small volume increase because the cell is contracting in the middle as well as protruding. The similarity is because the excited mode for myosin is the inverse of the mode for actin. Other results when this is the case, (not shown), are very similar to Model 1. Therefore, we investigate whether more interesting dynamics may occur if we try to excite differing modes for the two concentrations.

4.8.3 Cell deformation when $w^1_{1,1}$ and $w^0_{2,1}$ are excited for actin and myosin, respectively

While the idea that actin and myosin accumulate in opposite sides is quite well founded, their concentrations gradients are rarely exactly opposite. Therefore here we investigate if differing modes can be excited for actin and myosin. Choosing appropriate conditions we see the effects of actin and myosin in a different way. In Figure 4.9 we plot the concentrations of actin and myosin and the norm of the displacement when the initial conditions are

$$a(\boldsymbol{x}, 0) = 1 + w^1_{1,1}(\boldsymbol{x}) \times ran, \quad m(\boldsymbol{x}, 0) = 1 + w^0_{2,1}(\boldsymbol{x}) \times ran.$$

The cell squeezes where there is high myosin concentration and there is a protrusion in the direction of higher actin. The minimum and maximum in each spatial direction are shown in Figure 4.10.

4.8.4 Cell deformation when $w^0_{2,1}$ and $w^0_{1,1}$ are excited for actin and myosin, respectively

In Figure 4.11, the initial conditions

$$a(\boldsymbol{x}, 0) = 1 + w^0_{2,1} \times ran, \quad m(\boldsymbol{x}, 0) = 1 + w^0_{1,1}(\boldsymbol{x}) \times ran,$$

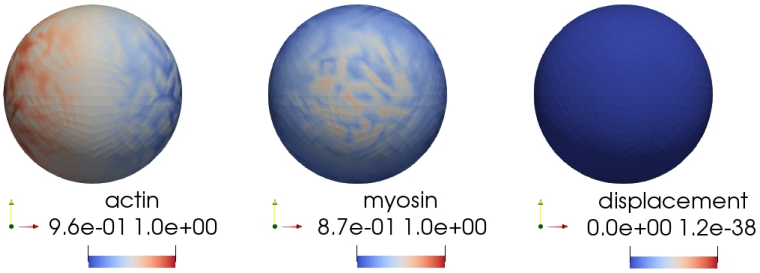

(a) t=0

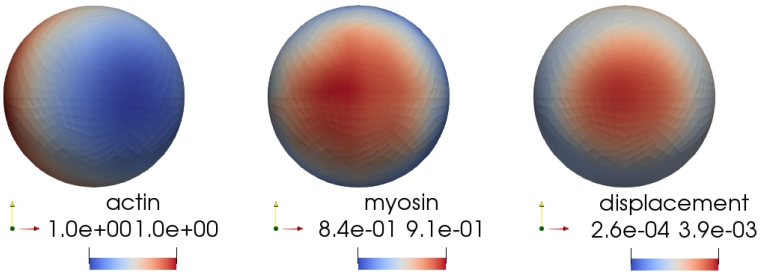

(b) t=1

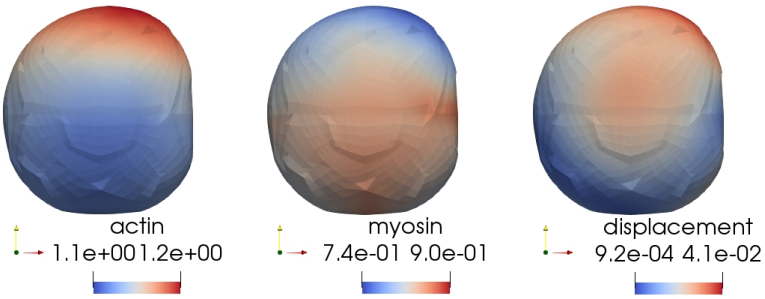

(c) t=9

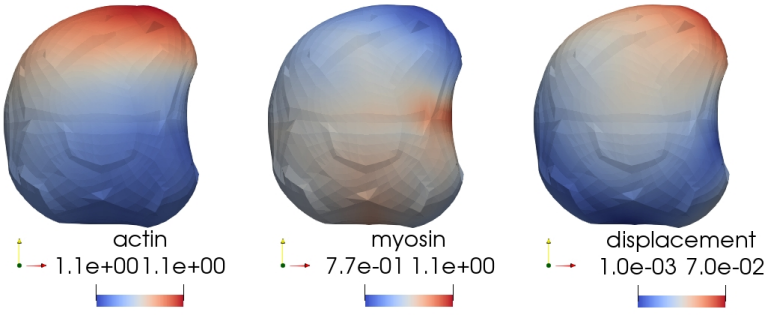

(d) t=13

Figure 4.9: Graphical displays of the actin and myosin concentrations, and the displacement at increasing time t, for the conditions described in Section 4.8.3. The sphere is squeezed where there is high myosin and then there is a protrusion in the area of high actin.

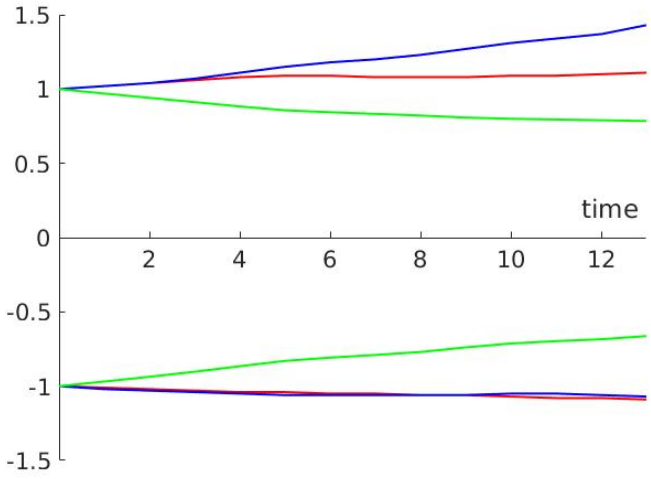

Figure 4.10: Plot to show the minimum and maximum of x (red), y (blue) and z (green) for the example in Section 4.8.3 and Figure 4.9. The cell is contracting in the y direction, expanding slightly in the x direction but significantly in the positive z-direction.

contain same two eigenfunctions as the last example but with different orientations, ($w^0_{1,1}$ is a rotation of $w^1_{1,1}$), we observe a quite different deformation. There is high actin concentration at the top and bottom of the sphere. Without the effect of myosin one would expect it to extend in both directions in the same way as in Section 4.8.2, however there is high myosin at the bottom so the cell only protrudes upwards. Then at $t = 5$ the protrusion slows and there is a contraction at the bottom where myosin concentration is high. There is another subsequent expansion and contraction with the actin and myosin concentrations reorganising to be is higher nearer the surface except when the cell is contracting, when the opposite is true, this is displayed in Figure 4.12. Figure 4.13b shows the translation of the cell and Figure 4.13a shows the change in length.

4.8.5 Cell deformation when $w^0_{1,1}$ and $w^0_{3,1}$ are excited for actin and myosin, respectively

Next, we begin with initial conditions

$$a(\boldsymbol{x}, 0) = 1 + w^1_{1,1}(\boldsymbol{x}) \times ran, \quad m(\boldsymbol{x}, 0) = 1 + w^0_{3,1}(\boldsymbol{x}) \times ran,$$

which leads to a protrusion in the area with highest actin which is pulling the cell in the negative z-direction. At the same time there is inward movement in areas of high myosin. The cell has translated in the negative z-direction and this is plotted in Figure 4.14, and the change in volume is illustrated in Figure 4.15.

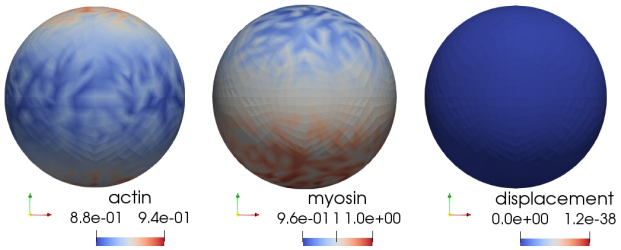

(a) t=0

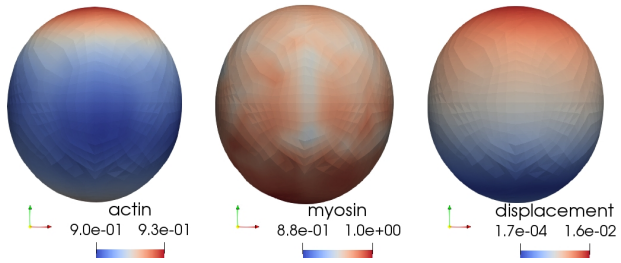

(b) t=5

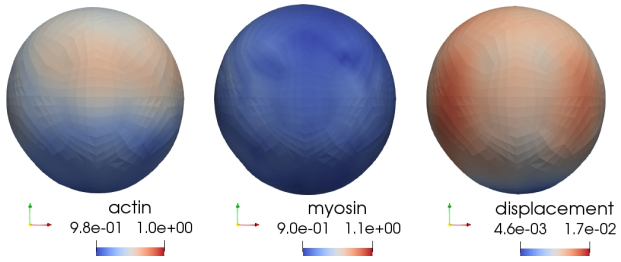

(c) t=20

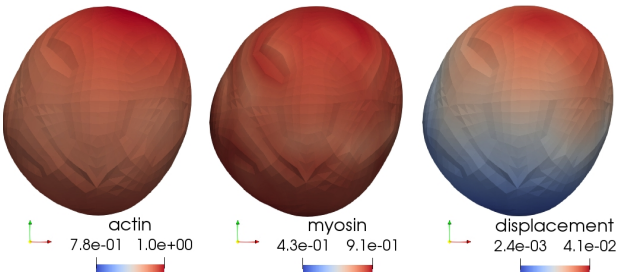

(d) t=29

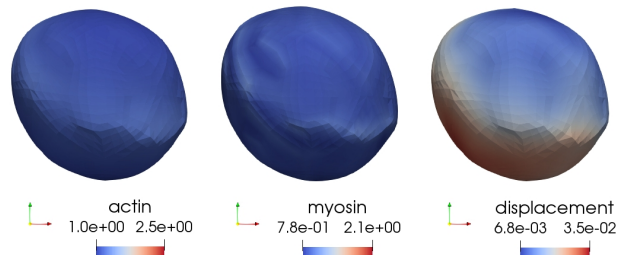

(e) t=36

Figure 4.11: Graphical descriptions of the solutions to simulations as described in Section 4.8.4. The cell expands and contracts twice, this can be seen more clearly in Figure 4.13. The concentration of myosin inside the sphere is shown in Figure 4.12.

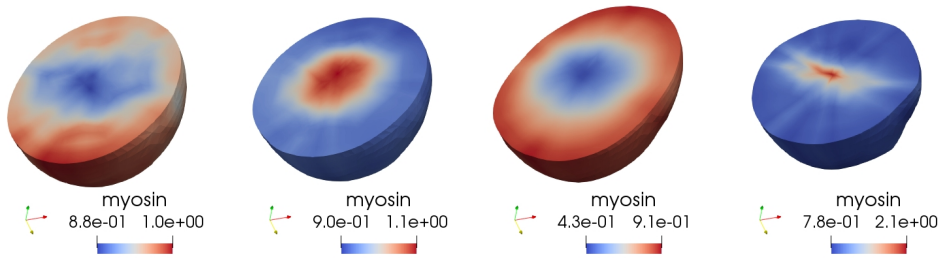

(a) t=5 (b) t=20 (c) t=29 (d) t=36

Figure 4.12: Graphical representations of solutions for myosin shown in Figure 4.11 with a cut-through to see the behaviour in the bulk. When the cell is expanded the concentration is highest and the edge and later when it is contracted it is highest at the centre. This is also seen in a similar, slightly less pronounced way in the actin concentration.

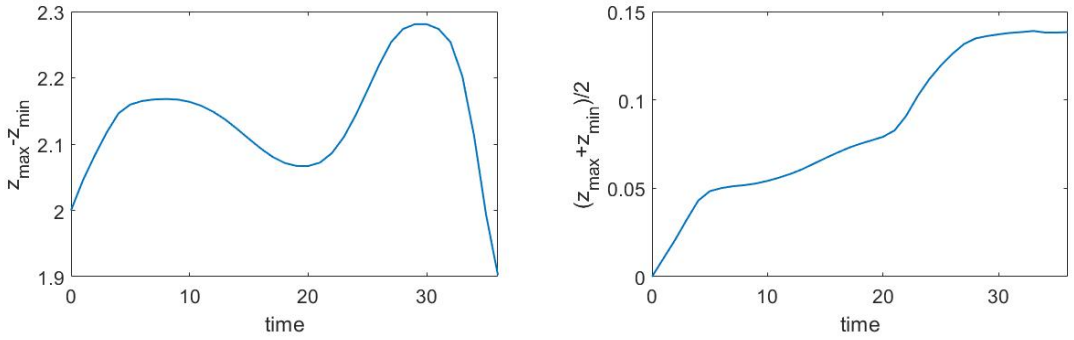

(a) Length of cell in z-direction (b) Translation the centre of the cell in z-direction

Figure 4.13: Plots to illustrate how the cell expands, contracts and translates in Figure 4.11. (Example 4.8.4).

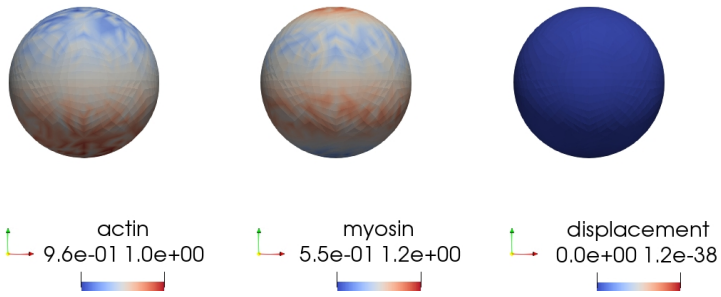

(a) t=0

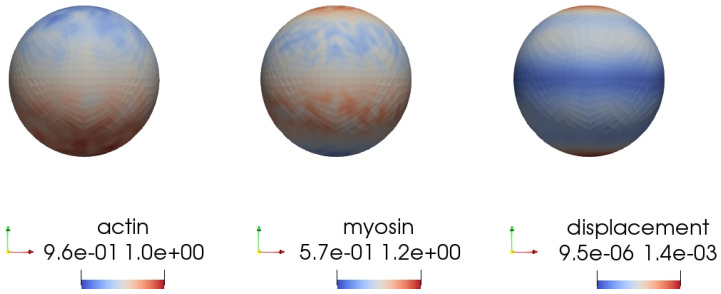

(b) t=0.1

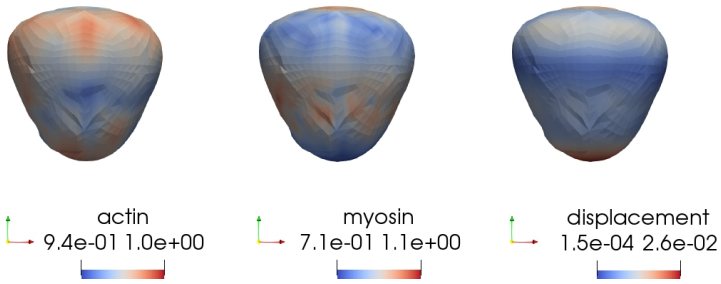

(c) t=2

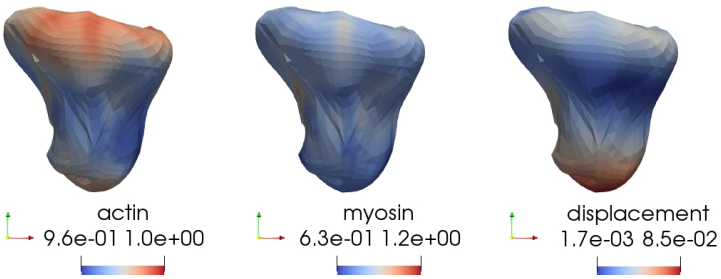

(d) t=7.1

Figure 4.14: Graphical displays of the solutions with conditions as described in Section 4.8.5. There is contraction in areas of high myosin, actin accumulates in areas of high curvature and the cell protrudes where there is high actin.

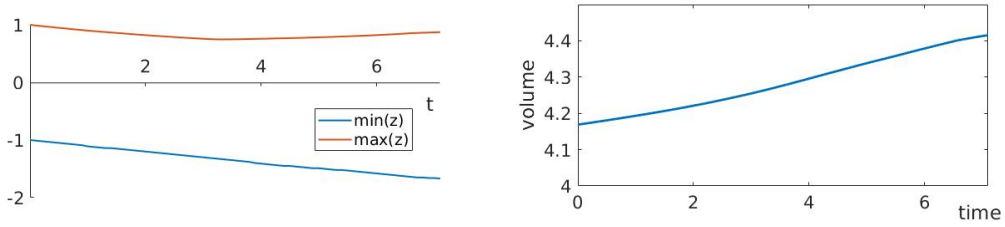

(a) Bounds on z

(b) Volume of the cell

Figure 4.15: Plotting of the range demonstrates that there is a translation followed an expansion in the z-direction. The cell is also being squeezed in the x- and y-direction so we do not observe a significant volume increase. (Example 4.8.5 and Figure 4.14).

4.8.6 Cell deformation when $w^1_{1,1}$ and $w^0_{4,1}$ are excited for actin and myosin, respectively

In another example of mixed modes, we start with

$$a(\boldsymbol{x},0) = 1 + w^1_{1,1}(\boldsymbol{x}) \times ran, \quad m(\boldsymbol{x},0) = 1 + w^0_{4,1}(\boldsymbol{x}) \times ran.$$

This leads to the expansion in Figure 4.16. The cell contracts inwards at areas of high myosin concentration and protrudes in the remaining areas, there are large protrusions in two opposing directions, the largest being the direction where actin was initially highest, subsequently, actin concentrates in areas of high curvature and protrudes further.

Section	4.8.2	4.8.3	4.8.4	4.8.5	4.8.6
Figure	4.8	4.9	4.11	4.14	4.16
ψ	200	20	150	100	100
c	-40	-80	-40	-80	-100
k_a	0.04	0.4	0.04	0.4	0.09
k_{ma}	0.05	0.5	0.05	0.05	0.09
k_{am}	0.06	0.12	0.06	0.07	0.15

Table 4.2: Parameters for simulations in this section.

4.9 Summary

Our model revolves around an equation which balances elasticity, viscosity, contractility and pressure. Connected to this are two reaction-diffusion equations for the concentrations of F-actin and bound myosin.

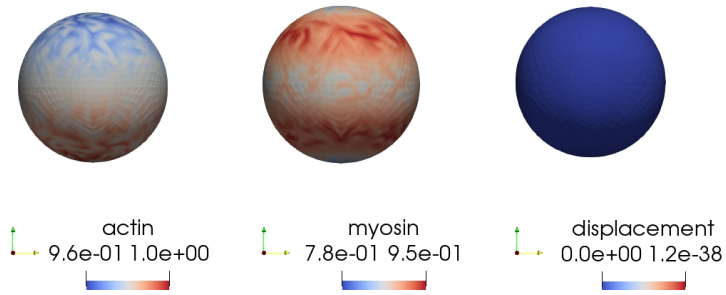

(a) t=0

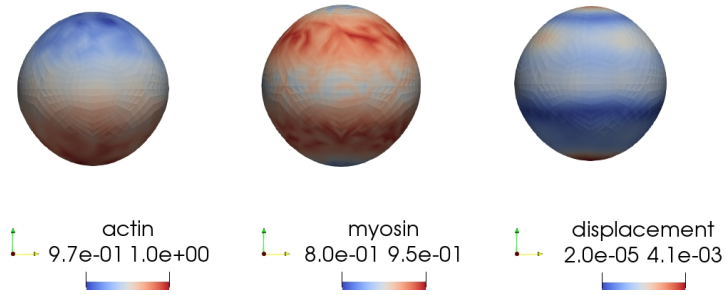

(b) t=1

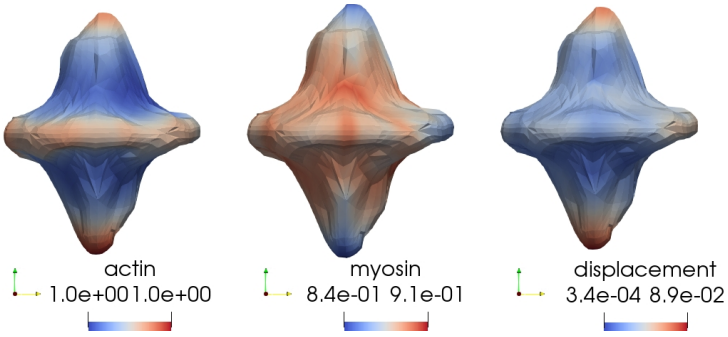

(c) t=67

Figure 4.16: Graphical displays of the solutions with conditions as described in Section 4.8.6. We see protrusions in a similar way to in Figure 4.14 but in two directions.

In this chapter we have presented a mathematical analysis of this model using linear stability theory. The process shows us which parameters we may choose in order for particular patterns to emerge. We outlined conditions on the parameters that will allow for instability and predicted the growth of modes which are defined as the eigenfunctions of the Laplacian on the domain.

This allows us to validate the numerical methods, outlined in Appendix A, we used produce the simulations. This is done by checking the numerical results are in agreement with linear stability theory, close to bifurcation points.

Our linear stability analysis is only valid when the shape is close to the sphere and will not tell us what will happen far away from this. Therefore we must construct a numerical method to provide more insight into the behaviour of the system.

In this chapter we have presented two collections of simulations. In the first, we solve the acto-myosin reaction-diffusion system on the stationary sphere, in the absence of mechanical properties. This verified the existence of diffusion-driven instability as predicted in Section 4.5. In the second we solve the full system, Model 2, which includes both biomechanical properties and biochemical reactions. Again, we see instability. Initally the results appear very similar to Model 1, however when differing modes are prompted for myosin and actin, respectively, the simulations have new attributes and details which were not possible to produce with the previous model.

4.9.1 Main observations from numerical results

Our numerical simulations showed that the new mechanobiochemical model extends naturally to three-dimensions and the addition of myosin allows some symmetries to be broken and more striking deformations are seen. In summary the main observations are:

- In the same way as in previous models of this nature, we see outward movement in areas of high actin concentration. Also, where there is higher curvature, higher actin concentration is observed.

- Outward movement due to high actin concentration is halted in areas with high myosin concentration.

- If there is low actin and high myosin, we can see negative curvature.

- With the addition of an equation for myosin, identifying bifurcation parameters becomes more complicated than in the previous model. The contractility due to myosin, c, strongly effects the speed of the deformation while the reaction constants

k_a, k_{ma} and k_{am}, and the diffusion coefficients D_a and D_m play a part in which mode the actin and myosin concentrations will arrange into. It is not as possible to isolate single modes just by picking parameter values, however, choosing appropriate initial conditions enhances the possibility of selecting the desired modes.

- In all our modelling framework, volume conservation is not modelled and numerical simulations exhibit cases where slight volume increase or decrease occurs. This suggests that a model for volume conservation or constraint would be necessary and this forms part of our future studies.

- Initial conditions are one of the most significant factors for the progression of the solutions.

Chapter 5

Conclusion and future directions

5.1 Thesis Summary

Ever since scientists discovered that all living things are made of cells, they have puzzled over the mechanisms of cell movement. By studying this movement we can help explain such diverse concepts as embryogenesis, wound healing and cancer metastasis. In this thesis we have discussed the mechanisms involved and plausible mathematical models of a single cell moving.

Most models consider only two dimensions because of computational constraints and, until recently, two dimensions was all that could be observed under a microscope. Because of advances in technology it is now possible to observe cells moving in three dimensions over time (Petrie et al., 2012; Friedl et al., 2012). The movements that are seen are much more varied and complex, therefore, the new challenge is understanding three dimensional movement. Laboratory experiments are still costly and time consuming, therefore, if computer programs are sufficiently developed they may be able to work alongside these experiments to accelerate advances and reduce costs.

The model we employ includes an equation which balances viscoelastic, contractile and pressure forces within the cell. Actin and myosin are key factors in the contractile and pressure forces so we also model these with reaction-diffusion equations. Since these equations are such a large part of our model we have discussed our novel method for parameter identification through mode isolation for such reaction-diffusion systems on 3-D geometries.

We begin our extension of the cytomechanical model (George, 2012; George et al., 2013; Madzvamuse and George, 2013) by extending it from two to three dimensions. This model consists of a force balance equation and a single reaction-diffusion equation for

actin. We subsequently add a second reaction-diffusion equation for myosin.

All these systems of partial differential equations are too complex to solve analytically. We perform linear stability analysis to analyse some behaviour of the systems and identify important parameters. This of course only holds close to bifurcation points therefore we need a numerical method to give further insight. The linear stability analysis allows us to verify the numerical method. We use the finite element method to solve our systems of equations numerically. For our purposes, it is the most efficient numerical method because of its ease in dealing with complex and evolving domains.

5.2 Key contributions

Unlike the previous study of George (2012) we used the software library deal.II (Bangerth et al., 2016) to implement the finite element method. The key difference between this software and the previously used ALBERTA (Schmidt et al., 2007) is that the elements are quadrilaterals rather than triangles. The implementation is therefore different but we were able to appropriately replicate the previous results of cytomechanical model on a unit disk. Once this new implementation was verified we extended the model substantially in several ways:

- The two-dimensional formulation was extended to three dimensions.
- Unlike previous studies of this modelling framework, for the first time, we considered a second reaction-diffusion model to describe how myosin interacts with actin and how it contributes cell contraction during cell migration. To take into account contraction, an additional linear tensor term was added to the viscoelastic model. In the absence of experimental observations, we postulated hypothetical reaction kinetics describing the interaction between actin and myosin.
- As a first step in understanding solution behaviour in three dimensions of the full model, linear stability analysis close to bifurcation points was carried out and appropriate key parameter values were identified.
- An evolving finite element method was implemented in multi-dimensions.

5.2.1 Biological applicability

Three dimensional cells deform into many unusual and irregular shapes, the addition of myosin to the model led to more irregular deformations. In addition, in one example

we saw a repeated expansion and contraction which can sometimes be seen in migrating cells (Friedl, 2004; Noguchi et al., 2015; Zhu and Mogilner, 2016). Collaborations with experimentalists will be important to determine key parameter values and to see if the model performs in a quantitatively and qualitatively similar way to experimental data.

5.3 Future directions

Our research suggests various research questions which are still to be addressed and could be incorporated into extensions of the model:

- New experimentally driven reaction kinetics between actin and myosin can readily be included into the modelling and computational framework. Furthermore, interactions between three or more molecular species can also be included into the modelling and computational framework, however, analysis of such models becomes very difficult. Example of interactions between multi-molecular species include actin, myosin, GEF, Rho, Rac and CDC42 (Simon et al., 2013; Nobes and Hall, 1995; Hall, 1998; Holmes et al., 2016).

- In our simulations we have significant shape deformations which often lead to distorted cells. Therefore using or formulating re-meshing strategies would lead to more accurate, stable and longer running simulations.

- In all the current and previous models, cell volume conservation is not maintained. The introduction of a mechanism for volume conservation would help rule out unrealistic large volume increases or decreases (Elliott et al., 2012).

- Many models theorise that adhesions are key for cell movement; in this framework it is possible to model adhesions to allow the cell to interact with either other cells (hence cell-to-cell interactions or cell-obstacle interactions) or to the extracellular matrix (in both two and three dimensions). Since adhesions occur at the cell cortex or membrane/surface, a bulk-surface modelling framework would be a natural candidate approach (MacDonald et al., 2016; Elliott and Ranner, 2013; Madzvamuse and Chung, 2016; Rätz and Röger, 2014; Cusseddu et al., 2018). Within this coupled bulk-surface approach the role of curvature, geometry, and surface tension can be easily studied both theoretically and computationally.

Appendix A

Finite element formulation

We introduced the finite element in Section 1.6 and in this appendix we outline exactly the formulations used for the numerical simulations presented in this thesis. The finite element formulation is obtained by first deriving a weak formulation, and then discretising in space and time. This transforms the continuous and complex model into a system of algebraic equations which can by solved computationally to give approximate solutions.

A.1 Finite element formulation for the reaction-diffusion equations in Chapter 2

A.1.1 Weak formulation

In general, a weak formulation does not hold absolutely but allows us to find a weak solution with respect to a test function. To find the weak formulation, we take the usual route and multiply by test functions $\phi \in H^1(\Omega)$, where $H^1(\Omega)$ is a Hilbert space, as defined in Section 2.2.2, and integrate over the domain. Hence, we write the weak formulation of (2.20) as follows: Find $a, m \in L^2(0,T;H^1(\Omega))$ such that for all $\phi, \psi \in H^1(\Omega)$ we have

$$\begin{cases} \int_\Omega a_t\phi + \int_\Omega \nabla a \cdot \nabla\phi = \gamma \int_\Omega f(a,m)\phi, \\ \int_\Omega m_t\psi + d\int_\Omega \nabla m \cdot \nabla\psi = \gamma \int_\Omega g(a,m)\psi, \end{cases} \qquad \boldsymbol{x} \in \Omega,\ t > 0. \tag{A.1}$$

We assume the well posedness of the weak formulation above.

A.1.2 Spatial discretisation

We now wish to define the problem at discrete points in space. We define the computational domain Ω_h by requiring that Ω_h is a polyhedral approximation to Ω. Furthermore, we define T_h to be a triangulation of Ω_h made up of non-degenerate elements κ_i,

i.e., $T_h = \bigcup_i \{\kappa_i\}$. Finally, we define the finite element space $V_h := \{v_h \in C^0(\Omega_h) : v_h|_\kappa \text{ is linear}\}$. The semidiscrete (space discrete) finite element approximation to (A.1) seeks a pair $(a_h, m_h) \in V_h^2$ such that

$$\int_{\Omega_h} \frac{\partial a_h}{\partial t}\phi + \int_{\Omega_h} \nabla a_h \cdot \nabla \phi = \gamma \int_{\Omega_h} I_h\left[f(a_h, m_h)\right]\phi, \tag{A.2a}$$

$$\int_{\Omega_h} \frac{\partial m_h}{\partial t}\psi + d\int_{\Omega_h} \nabla m_h \cdot \nabla \psi = \gamma \int_{\Omega_h} I_h\left[g(a_h, m_h)\right]\psi, \tag{A.2b}$$

$\forall \phi, \psi \in V_h$, where we use the Lagrange interpolant I_h of the initial data into V_h as initial conditions for the scheme. Letting N_h be the total number of degrees of freedom of the nodes for the finite element discretisation, we can write

$$a_h = \sum_{i=1}^{N_h} \alpha_i \phi_i, \quad m_h = \sum_{i=1}^{N_h} \mu_i \phi_i, \text{ where } \phi_i(\boldsymbol{x}_j, t) \in V_h : \phi_i = \begin{cases} 1 \text{ if } i = j, \\ 0 \text{ if } i \neq j. \end{cases} \tag{A.3}$$

In order to illustrate a concrete example of the scheme, we focus on the reaction-diffusion system with Schnakenberg kinetics (2.45). The finite element approximation (A.2a) with the Schnakenberg kinetics can be written in matrix-vector form as follows

$$\mathbf{M}\boldsymbol{\alpha}_t + \mathbf{A}\boldsymbol{\alpha} = \gamma\left[a\mathbf{H} - \mathbf{M}\boldsymbol{\alpha} + \mathbf{M}\boldsymbol{\alpha}^2\boldsymbol{\mu}\right], \tag{A.4a}$$

$$\mathbf{M}\boldsymbol{\mu}_t + d\mathbf{A}\boldsymbol{\mu} = \gamma\left[b\mathbf{H} - \mathbf{M}\boldsymbol{\alpha}^2\boldsymbol{\mu}\right], \tag{A.4b}$$

where $\boldsymbol{\alpha} = (\alpha_1, ..., \alpha_{N_h})$ and $\boldsymbol{\mu}(\mu_1, ..., \mu_{N_h})$ are the coefficient vectors of the finite element functions a_h and m_h respectively, $\boldsymbol{\alpha}^2\boldsymbol{\mu}$ is a pointwise product, and $\mathbf{M}$ and $\mathbf{A}$ are mass and stiffness matrices and $\mathbf{H}$ is a load vector with entries given by

$$M_{i,j} = \int_{\Omega_h} \phi_i\phi_j, \quad A_{i,j} = \int_{\Omega_h} \nabla\phi_i \cdot \nabla\phi_j, \qquad H_j = \int_{\Omega_h} \phi_j, \quad i = 1, ..., N_h. \tag{A.5}$$

A.1.3 Temporal discretisation

For the temporal discretisation we employ an IMEX method (Lakkis et al., 2013; Madzvamuse, 2006; Ruuth, 1995) in which the diffusive term is treated implicitly and the reaction terms are treated explicitly, for simplicity we employ a uniform time step τ. Introducing the shorthand for a time discrete sequence of functions, $f^n = f(t_n)$, the fully discrete scheme we employ reads, for $n = 0, 1, \ldots$, given $(a_h^n, m_h^n) \in V_h^2$ find $(a_h^{n+1}, m_h^{n+1}) \in V_h^2$ such that, $\forall \phi, \psi \in V_h$,

$$\begin{cases} \int_{\Omega_h} \frac{1}{\tau}\left(a_h^{n+1} - a_h^n\right)\phi + \int_{\Omega_h} \nabla a_h^{n+1} \cdot \nabla\phi = \gamma \int_{\Omega_h} I_h\left[f(a_h^n, m_h^n)\right]\phi, \\ \int_{\Omega_h} \frac{1}{\tau}\left(m_h^{n+1} - m_h^n\right)\psi + d\int_{\Omega_h} \nabla m_h^{n+1} \cdot \nabla\psi = \gamma \int_{\Omega_h} I_h\left[g(a_h^n, m_h^n)\right]\psi, \end{cases} \tag{A.6}$$

where we use Lagrange interpolant of the initial data into V_h as initial conditions for the scheme. This leads us to the following matrix vector form

$$\left(\frac{1}{\tau}\mathbf{M}+\mathbf{A}\right)\boldsymbol{\alpha}^{n+1}=\gamma\left[a\mathbf{H}-\mathbf{M}\boldsymbol{\alpha}^{n}+\mathbf{M}(\boldsymbol{\alpha}^{n})^{2}\boldsymbol{\mu}^{n}\right]+\frac{1}{\tau}\mathbf{M}\boldsymbol{\alpha}^{n}, \tag{A.7a}$$

$$\left(\frac{1}{\tau}\mathbf{M}+d\mathbf{A}\right)\boldsymbol{\mu}^{n+1}=\gamma\left[b\mathbf{H}-\mathbf{M}(\boldsymbol{\alpha}^{n})^{2}\boldsymbol{\mu}^{n}\right]+\frac{1}{\tau}\mathbf{M}\boldsymbol{\mu}^{n}. \tag{A.7b}$$

Since we are interested in convergence to a spatially inhomogeneous steady state, for the stopping criteria we use the L_2 norm of the approximate time-derivative of the discrete solution, stopping the computation if this decreases below a tolerance, usually 10^{-9} (see Figure 2.3 on page 45).

We use a very similar formulation for the reaction-diffusion equations in Chapters 3 and 4 but there are differences due to including a flow term. The full formulation is discussed in the next section.

A.2 Finite element formulation for the full system

A.2.1 Derivation of the weak formulation

To begin, the force balance is separated into a system of three partial differential equations representing the three space dimensions. This clarifies the derivation of the weak formulation. Since $\boldsymbol{\sigma}_v, \boldsymbol{\sigma}_e, \boldsymbol{\sigma}_c$ and $\boldsymbol{\sigma}_p$ are all stress tensors (defined in section 3.3) we can write them in matrix form. As a reminder they are:

$$\boldsymbol{\sigma}_v=\mu_1\frac{\partial\boldsymbol{\varepsilon}}{\partial t}+\mu_2\frac{\partial\phi}{\partial t}\mathbf{I}, \qquad \boldsymbol{\sigma}_e=\frac{E}{1+\nu}(\boldsymbol{\varepsilon}+\frac{\nu}{1-2\nu}\phi\mathbf{I}),$$

$$\boldsymbol{\sigma}_c=(\psi a^2e^{-a/a_{sat}}+cm)\mathbf{I}, \qquad \boldsymbol{\sigma}_p=\frac{p}{1+\phi}\big(1+\frac{2}{\pi}\delta(l)\arctan a\big)\mathbf{I}.$$

In three dimensions, strain and dilation are given by

$$\epsilon(\mathbf{u}):=\frac{1}{2}(\nabla\mathbf{u}+(\nabla\mathbf{u})^T)=\begin{pmatrix}\frac{\partial u}{\partial x} & \frac{1}{2}(\frac{\partial v}{\partial x}+\frac{\partial u}{\partial y}) & \frac{1}{2}(\frac{\partial u}{\partial z}+\frac{\partial w}{\partial x})\\ \frac{1}{2}(\frac{\partial v}{\partial x}+\frac{\partial u}{\partial y}) & \frac{\partial v}{\partial y} & \frac{1}{2}(\frac{\partial v}{\partial z}+\frac{\partial w}{\partial y})\\ \frac{1}{2}(\frac{\partial v}{\partial x}+\frac{\partial u}{\partial y}) & \frac{1}{2}(\frac{\partial w}{\partial y}+\frac{\partial v}{\partial z}) & \frac{\partial w}{\partial z}\end{pmatrix}$$

$$\text{and } \phi(\mathbf{u}):=\frac{\partial u}{\partial x}+\frac{\partial v}{\partial y}+\frac{\partial w}{\partial z}.$$

It follows then that we can write the stress tensors in three-dimensional tensor-matrix form:

$$\boldsymbol{\sigma}_v = \begin{pmatrix} (\mu_1+\mu_2)\frac{\partial \dot{u}}{\partial x} + \mu_2(\frac{\partial \dot{v}}{\partial y} + \frac{\partial \dot{w}}{\partial z}) & \frac{\mu_1}{2}(\frac{\partial \dot{v}}{\partial x} + \frac{\partial \dot{u}}{\partial y}) & \frac{\mu_1}{2}(\frac{\partial \dot{w}}{\partial x} + \frac{\partial \dot{u}}{\partial z}) \\ \frac{\mu_1}{2}(\frac{\partial \dot{v}}{\partial x} + \frac{\partial \dot{u}}{\partial y}) & \mu_2(\frac{\partial \dot{u}}{\partial x} + \frac{\partial \dot{w}}{\partial z}) + (\mu_1+\mu_2)\frac{\partial \dot{v}}{\partial y} & \frac{\mu_1}{2}(\frac{\partial \dot{v}}{\partial z} + \frac{\partial \dot{w}}{\partial y}) \\ \frac{\mu_1}{2}(\frac{\partial \dot{w}}{\partial x} + \frac{\partial \dot{u}}{\partial z}) & \frac{\mu_1}{2}(\frac{\partial \dot{v}}{\partial z} + \frac{\partial \dot{w}}{\partial y}) & (\mu_1+\mu_2)\frac{\partial \dot{w}}{\partial z} + \mu_2(\frac{\partial \dot{u}}{\partial x} + \frac{\partial \dot{v}}{\partial y}) \end{pmatrix},$$

$$\boldsymbol{\sigma}_e = \frac{E}{1-\nu}\begin{pmatrix} \frac{\partial u}{\partial x} + \nu'(\frac{\partial u}{\partial x} + \frac{\partial v}{\partial y} + \frac{\partial w}{\partial z}) & \frac{1}{2}(\frac{\partial v}{\partial x} + \frac{\partial u}{\partial y}) & \frac{1}{2}(\frac{\partial u}{\partial z} + \frac{\partial w}{\partial x}) \\ \frac{1}{2}(\frac{\partial v}{\partial x} + \frac{\partial u}{\partial y}) & \frac{\partial v}{\partial y} + \nu'(\frac{\partial u}{\partial x} + \frac{\partial v}{\partial y} + \frac{\partial w}{\partial z}) & \frac{1}{2}(\frac{\partial v}{\partial z} + \frac{\partial w}{\partial y}) \\ \frac{1}{2}(\frac{\partial w}{\partial x} + \frac{\partial u}{\partial z}) & \frac{1}{2}(\frac{\partial v}{\partial z} + \frac{\partial w}{\partial y}) & \frac{\partial w}{\partial z} + \nu'(\frac{\partial u}{\partial x} + \frac{\partial v}{\partial y} + \frac{\partial w}{\partial z}) \end{pmatrix},$$

$$\boldsymbol{\sigma}_c = \begin{pmatrix} \psi a^2 e^{-a/a_{sat}} & 0 & 0 \\ 0 & \psi a^2 e^{-a/a_{sat}} & 0 \\ 0 & 0 & \psi a^2 e^{-a/a_{sat}} \end{pmatrix},$$

$$\boldsymbol{\sigma}_p = \begin{pmatrix} \frac{p}{1+\phi}\left(1 + \frac{2}{\pi}\delta(l)\arctan a\right) & 0 & 0 \\ 0 & \frac{p}{1+\phi}\left(1 + \frac{2}{\pi}\delta(l)\arctan a\right) & 0 \\ 0 & 0 & \frac{p}{1+\phi}\left(1 + \frac{2}{\pi}\delta(l)\arctan a\right) \end{pmatrix}.$$

Substituting these values into $\nabla \cdot (\boldsymbol{\sigma}_v + \boldsymbol{\sigma}_e + \boldsymbol{\sigma}_c + \boldsymbol{\sigma}_p) = \mathbf{0}$ gives us three equations

$$\frac{\partial}{\partial x}\left(\mathbf{D}_{11}\frac{\partial \dot{u}}{\partial x} + \mathbf{D}_{12}(\frac{\partial \dot{v}}{\partial y} + \frac{\partial \dot{w}}{\partial z}) + \mathbf{C}_{11}\frac{\partial u}{\partial x} + \mathbf{C}_{12}\left(\frac{\partial v}{\partial y} + \frac{\partial w}{\partial z}\right)\right)$$
$$+\frac{\partial}{\partial y}\left(\mathbf{D}_{33}(\frac{\partial \dot{v}}{\partial x} + \frac{\partial \dot{u}}{\partial y}) + \mathbf{C}_{33}(\frac{\partial v}{\partial x} + \frac{\partial u}{\partial y})\right) + \frac{\partial}{\partial z}\left(\mathbf{D}_{33}(\frac{\partial \dot{w}}{\partial x} + \frac{\partial \dot{u}}{\partial z}) + \mathbf{C}_{33}(\frac{\partial w}{\partial x} + \frac{\partial u}{\partial z})\right) = -\frac{\partial f}{\partial x},$$

$$\frac{\partial}{\partial x}\left(\mathbf{D}_{33}(\frac{\partial \dot{v}}{\partial x} + \frac{\partial \dot{u}}{\partial y}) + \mathbf{C}_{33}(\frac{\partial v}{\partial x} + \frac{\partial u}{\partial y})\right) + \frac{\partial}{\partial y}\left(\mathbf{D}_{11}\frac{\partial \dot{v}}{\partial y} + \mathbf{D}_{12}(\frac{\partial \dot{u}}{\partial x} + \frac{\partial \dot{w}}{\partial z})\right.$$
$$\left.+\mathbf{C}_{11}\frac{\partial v}{\partial y} + \mathbf{C}_{12}(\frac{\partial u}{\partial x} + \frac{\partial w}{\partial z})\right) + \frac{\partial}{\partial z}\left(\mathbf{D}_{33}(\frac{\partial \dot{w}}{\partial y} + \frac{\partial \dot{w}}{\partial z}) + \mathbf{C}_{33}(\frac{\partial w}{\partial z} + \frac{\partial v}{\partial z})\right) = -\frac{\partial f}{\partial y},$$

$$\frac{\partial}{\partial x}\left(\mathbf{D}_{33}(\frac{\partial \dot{w}}{\partial x} + \frac{\partial \dot{u}}{\partial z}) + \mathbf{C}_{33}(\frac{\partial w}{\partial x} + \frac{\partial u}{\partial z})\right) + \frac{\partial}{\partial y}\left(\mathbf{D}_{33}(\frac{\partial \dot{v}}{\partial z} + \frac{\partial \dot{w}}{\partial y}) + \mathbf{C}_{33}(\frac{\partial v}{\partial z} + \frac{\partial w}{\partial y})\right)$$
$$+\frac{\partial}{\partial z}\left(\mathbf{D}_{11}\frac{\partial \dot{w}}{\partial z} + \mathbf{D}_{12}(\frac{\partial \dot{v}}{\partial y} + \frac{\partial \dot{u}}{\partial x}) + \mathbf{C}_{11}\frac{\partial w}{\partial z} + \mathbf{C}_{12}(\frac{\partial u}{\partial x} + \frac{\partial v}{\partial y})\right) = -\frac{\partial f}{\partial z},$$

where

$$f = \left[\frac{p}{1+\phi}\left(1+\frac{2}{\pi}\delta(l)\arctan a\right)+\psi a^2 e^{-a/a_{sat}}\right], \tag{A.13a}$$

$$\mathbf{D}_{11} = \mu_1+\mu_2, \quad \mathbf{D}_{12} = \mu_2, \quad \mathbf{D}_{33} = \frac{\mu_1}{2}, \tag{A.13b}$$

$$\mathbf{C}_{11} = \frac{E(1-\nu)}{(1+\nu)(1-2\nu)}, \quad \mathbf{C}_{12} = \frac{E\nu}{(1+\nu)(1-2\nu)} \text{ and } \mathbf{C}_{33} = \frac{E}{2(1+\nu)}. \tag{A.13c}$$

To find the weak formulation like in Section A.1, we multiply by a test function $\hat{\phi}(\boldsymbol{x},t) \in H^1(\boldsymbol{\Omega}_t)$, and integrate over the domain. This takes into account Green's formula and the boundary conditions. The boundary condition $\boldsymbol{\sigma}_v \cdot \mathbf{n} = \boldsymbol{\sigma}_e \cdot \mathbf{n} = 0$ means that boundary term disappears during integration. The weak formulation is a $u(\boldsymbol{x},t)$, $v(\boldsymbol{x},t)$ and $w(\boldsymbol{x},t) \in H^1(\boldsymbol{\Omega}_t)$, $t \in I$ such that

$$\begin{aligned}\int_{\boldsymbol{\Omega}_t} &\frac{\partial\hat{\phi}}{\partial x}\left(\mathbf{D}_{11}\frac{\partial\dot{u}}{\partial x}+\mathbf{D}_{12}(\frac{\partial\dot{v}}{\partial y}+\frac{\partial\dot{w}}{\partial z})+\mathbf{C}_{11}\frac{\partial u}{\partial x}+\mathbf{C}_{12}\left(\frac{\partial v}{\partial y}+\frac{\partial w}{\partial z}\right)\right)+\\ &\frac{\partial\hat{\phi}}{\partial y}\left(\mathbf{D}_{33}(\frac{\partial\dot{v}}{\partial x}+\frac{\partial\dot{u}}{\partial y})+\mathbf{C}_{33}(\frac{\partial v}{\partial x}+\frac{\partial u}{\partial y})\right)+\frac{\partial\hat{\phi}}{\partial z}\left(\mathbf{D}_{33}(\frac{\partial\dot{w}}{\partial x}+\frac{\partial\dot{u}}{\partial z})+\mathbf{C}_{33}(\frac{\partial w}{\partial x}+\frac{\partial u}{\partial z})\right)d\boldsymbol{\Omega}_t\\ &= -\int_{\boldsymbol{\Omega}_t}\frac{\partial\hat{\phi}}{\partial x}f d\boldsymbol{\Omega}_t+\int_{\partial\boldsymbol{\Omega}_t}\hat{\phi}f n_1 ds,\end{aligned}$$

$$\begin{aligned}\int_{\boldsymbol{\Omega}_t} &\frac{\partial\hat{\phi}}{\partial x}\left(\mathbf{D}_{33}(\frac{\partial\dot{v}}{\partial x}+\frac{\partial\dot{u}}{\partial y})+\mathbf{C}_{33}(\frac{\partial v}{\partial x}+\frac{\partial u}{\partial y})\right)+\frac{\partial\hat{\phi}}{\partial y}\left(\mathbf{D}_{11}\frac{\partial\dot{v}}{\partial y}+\mathbf{D}_{12}(\frac{\partial\dot{u}}{\partial x}+\frac{\partial\dot{w}}{\partial z})+\right.\\ &\left.\mathbf{C}_{11}\frac{\partial v}{\partial y}+\mathbf{C}_{12}(\frac{\partial u}{\partial x}+\frac{\partial w}{\partial z})\right)+\frac{\partial\hat{\phi}}{\partial z}\left(\mathbf{D}_{33}(\frac{\partial\dot{w}}{\partial y}+\frac{\partial\dot{w}}{\partial z})+\mathbf{C}_{33}(\frac{\partial w}{\partial z}+\frac{\partial v}{\partial z})\right)d\boldsymbol{\Omega}_t\\ &= -\int_{\boldsymbol{\Omega}_t}\frac{\partial\hat{\phi}}{\partial y}f d\boldsymbol{\Omega}_t+\int_{\partial\boldsymbol{\Omega}_t}\hat{\phi}f n_2 ds,\end{aligned}$$

$$\begin{aligned}\int_{\boldsymbol{\Omega}_t} &\frac{\partial\hat{\phi}}{\partial x}\left(\mathbf{D}_{33}(\frac{\partial\dot{w}}{\partial x}+\frac{\partial\dot{u}}{\partial z})+\mathbf{C}_{33}(\frac{\partial w}{\partial x}+\frac{\partial u}{\partial z})\right)+\frac{\partial\hat{\phi}}{\partial y}\left(\mathbf{D}_{33}(\frac{\partial\dot{v}}{\partial z}+\frac{\partial\dot{w}}{\partial y})+\mathbf{C}_{33}(\frac{\partial v}{\partial z}+\frac{\partial w}{\partial y})\right)+\\ &\frac{\partial\hat{\phi}}{\partial z}\left(\mathbf{D}_{11}\frac{\partial\dot{w}}{\partial z}+\mathbf{D}_{12}(\frac{\partial\dot{v}}{\partial y}+\frac{\partial\dot{u}}{\partial x})+\mathbf{C}_{11}\frac{\partial w}{\partial z}+\mathbf{C}_{12}(\frac{\partial u}{\partial x}+\frac{\partial v}{\partial y})\right)d\boldsymbol{\Omega}_t\\ &= -\int_{\boldsymbol{\Omega}_t}\frac{\partial\hat{\phi}}{\partial z}f d\boldsymbol{\Omega}_t+\int_{\partial\boldsymbol{\Omega}_t}\hat{\phi}f n_3 ds.\end{aligned}$$

Since $\frac{\partial f}{\partial x}$, $\frac{\partial f}{\partial y}$ and $\frac{\partial f}{\partial z}$ are difficult to evaluate, we have used identities derived from the gradient theorem to write the weak form as above. In other words we have used that

$$\int_{\boldsymbol{\Omega}_t}\frac{\partial f_j}{\partial x}\hat{\phi}d\boldsymbol{\Omega}_t = -\int_{\boldsymbol{\Omega}_t}\frac{\partial\hat{\phi}}{\partial x}f_j d\boldsymbol{\Omega}_t+\int_{\partial\boldsymbol{\Omega}_t}\hat{\phi}f_j n_j ds, \tag{A.15}$$

for $j = 1,2,3$, where x can also be substituted by y and z. n_1, n_2, n_3 are the direction components of the outward unit vector $\mathbf{n}$ normal to $\partial\boldsymbol{\Omega}_t$.

Next we want to find the weak formulation of the reaction-diffusion equations which are given as

$$\frac{\partial a}{\partial t}+\nabla\cdot(a\boldsymbol{\beta})-D_a\Delta a = f(a,m), \quad \frac{\partial m}{\partial t}+\nabla\cdot(m\boldsymbol{\beta})-D_m\Delta m = g(a,m). \tag{A.16}$$

We apply the product rule and convert to the material derivative (defined as $\frac{Da}{Dt} = \frac{\partial a}{\partial t} + a(\nabla \cdot \boldsymbol{\beta})$, in Reddy (1993)). This gives

$$\frac{Da}{Dt} - D_a \Delta a + a(\nabla \cdot \boldsymbol{\beta}) = f(a, m),$$
$$\frac{Dm}{Dt} - D_m \Delta m + m(\nabla \cdot \boldsymbol{\beta}) = g(a, m).$$

Now continuing as with the force balance equation, we multiply by a test function $\hat{\psi}(\boldsymbol{x}, t) \in H^1(\boldsymbol{\Omega}_t)$ and integrate over the domain

$$\int_{\boldsymbol{\Omega}_t} \left(\frac{Da}{Dt} + a(\nabla \cdot \boldsymbol{\beta}) \right) \hat{\psi} - (D_a \Delta a)\hat{\psi} \, d\boldsymbol{\Omega}_t = \int_{\boldsymbol{\Omega}_t} f(a, m)\hat{\psi} \, d\boldsymbol{\Omega}_t,$$
$$\int_{\boldsymbol{\Omega}_t} \left(\frac{Dm}{Dt} + m(\nabla \cdot \boldsymbol{\beta}) \right) \hat{\psi} - (D_m \Delta m)\hat{\psi} \, d\boldsymbol{\Omega}_t = \int_{\boldsymbol{\Omega}_t} g(a, m)\hat{\psi} \, d\boldsymbol{\Omega}_t.$$

The terms $(D_a \Delta a)\hat{\psi}$ and $(D_m \Delta m)\hat{\psi}$ can integrated by parts (applying the boundary condition $\mathbf{n} \cdot \nabla a = \mathbf{n} \cdot \nabla m = 0$) and for the remaining part of the left hand side we can use Reynolds transport theorem which is given by:

Theorem 2. (*Reynolds Transport Theorem*) Let $g(\boldsymbol{x}, t)$ be a scalar function defined on $\boldsymbol{\Omega}_t$ and $\boldsymbol{\beta}$ be a flow velocity field then

$$\frac{\partial}{\partial t} \int_{\boldsymbol{\Omega}_t} g d\boldsymbol{\Omega}_t = \int_{\boldsymbol{\Omega}_t} \left(\frac{Dg}{Dt} + g \nabla \cdot \boldsymbol{\beta} \right). \tag{A.19}$$

A proof of this theorem can be found in Madzvamuse (2000)

This means the weak formulation can be written as: Find $a(\boldsymbol{x}, t),\ m(\boldsymbol{x}, t) \in H^1(\boldsymbol{\Omega}_t), t \in I$ such that

$$\frac{\partial}{\partial t} \int_{\boldsymbol{\Omega}_t} a\hat{\psi} d\boldsymbol{\Omega}_t + \int_{\boldsymbol{\Omega}_t} (D_a \nabla a \cdot \nabla \hat{\psi}) d\boldsymbol{\Omega}_t = \int_{\boldsymbol{\Omega}_t} (f(a, m)\hat{\psi} + a\frac{D\hat{\psi}}{Dt}) \, d\boldsymbol{\Omega}_t, \tag{A.20a}$$
$$\frac{\partial}{\partial t} \int_{\boldsymbol{\Omega}_t} m\hat{\psi} d\boldsymbol{\Omega}_t + \int_{\boldsymbol{\Omega}_t} (D_m \nabla m \cdot \nabla \hat{\psi}) d\boldsymbol{\Omega}_t = \int_{\boldsymbol{\Omega}_t} (g(a, m)\hat{\psi} + m\frac{D\hat{\psi}}{Dt}) \, d\boldsymbol{\Omega}_t, \tag{A.20b}$$

for all $\hat{\psi}(\boldsymbol{x}, t) \in H^1(\boldsymbol{\Omega}_t)$.

A.2.2 Space discretisation

To discretise in space, we define the computational domain $\Omega_{h,t}$ as a polyhedral approximation to $\boldsymbol{\Omega}_t$, $T_{h,t}$ the discretisation of $\Omega_{h,t}$ made up of non-degenerate elements κ_i and the finite element space $V_h(t) := \{v_h \in C^0(\boldsymbol{\Omega}_t) : v_h|_\kappa \text{ is linear}\}$. Thus the space-discrete

problem is to find $u_h(\boldsymbol{x},t)$, $v_h(\boldsymbol{x},t)$, $w_h(\boldsymbol{x},t)$, $a_h(\boldsymbol{x},t)$, $m_h(\boldsymbol{x},t) \in V_h(t),\ t \in I$, such that

$$\int_{\boldsymbol{\Omega}_{h,t}} \frac{\partial\hat{\phi}}{\partial x}\left(\mathbf{D}_{11}\frac{\partial\dot{u}_h}{\partial x}+\mathbf{D}_{12}(\frac{\partial\dot{v}_h}{\partial y}+\frac{\partial\dot{w}_h}{\partial z})+\mathbf{C}_{11}\frac{\partial u_h}{\partial x}+\mathbf{C}_{12}\left(\frac{\partial v_h}{\partial y}+\frac{\partial w_h}{\partial z}\right)\right)+\frac{\partial\hat{\phi}}{\partial y}\Bigg(\mathbf{D}_{33}(\frac{\partial\dot{v}_h}{\partial x}+\frac{\partial\dot{u}_h}{\partial y})$$
$$+\mathbf{C}_{33}(\frac{\partial v_h}{\partial x}+\frac{\partial u_h}{\partial y})\Bigg)+\frac{\partial\hat{\phi}}{\partial z}\left(\mathbf{D}_{33}(\frac{\partial\dot{w}_h}{\partial x}+\frac{\partial\dot{u}_h}{\partial z})+\mathbf{C}_{33}(\frac{\partial w_h}{\partial x}+\frac{\partial u_h}{\partial z})\right)d\boldsymbol{\Omega}_t$$
$$=-\int_{\boldsymbol{\Omega}_{h,t}}\frac{\partial\hat{\phi}}{\partial x}f d\boldsymbol{\Omega}_{h,t}+\int_{\partial\boldsymbol{\Omega}_{h,t}}\hat{\phi}f n_1 ds,$$

$$\int_{\boldsymbol{\Omega}_{h,t}} \frac{\partial\hat{\phi}}{\partial x}\left(\mathbf{D}_{33}(\frac{\partial\dot{v}_h}{\partial x}+\frac{\partial\dot{u}_h}{\partial y})+\mathbf{C}_{33}(\frac{\partial v_h}{\partial x}+\frac{\partial u_h}{\partial y})\right)+\frac{\partial\hat{\phi}}{\partial y}\Bigg(\mathbf{D}_{11}\frac{\partial\dot{v}_h}{\partial y}+\mathbf{D}_{12}(\frac{\partial\dot{u}_h}{\partial x}+\frac{\partial\dot{w}_h}{\partial z})$$
$$+\mathbf{C}_{11}\frac{\partial v_h}{\partial y}+\mathbf{C}_{12}(\frac{\partial u_h}{\partial x}+\frac{\partial w_h}{\partial z})\Bigg)+\frac{\partial\hat{\phi}}{\partial z}\left(\mathbf{D}_{33}(\frac{\partial\dot{w}_h}{\partial y}+\frac{\partial\dot{v}_h}{\partial z})+\mathbf{C}_{33}(\frac{\partial w_h}{\partial z}+\frac{\partial v_h}{\partial z})\right)d\boldsymbol{\Omega}_{h,t}$$
$$=-\int_{\boldsymbol{\Omega}_{h,t}}\frac{\partial\hat{\phi}}{\partial y}f d\boldsymbol{\Omega}_{h,t}+\int_{\partial\boldsymbol{\Omega}_{h,t}}\hat{\phi}f n_2 ds,$$

$$\int_{\boldsymbol{\Omega}_{h,t}} \frac{\partial\hat{\phi}}{\partial x}\left(\mathbf{D}_{33}(\frac{\partial\dot{w}_h}{\partial x}+\frac{\partial\dot{u}_h}{\partial z})+\mathbf{C}_{33}(\frac{\partial w_h}{\partial x}+\frac{\partial u_h}{\partial z})\right)+\frac{\partial\hat{\phi}}{\partial y}\left(\mathbf{D}_{33}(\frac{\partial\dot{v}_h}{\partial z}+\frac{\partial\dot{w}_h}{\partial y})+\mathbf{C}_{33}(\frac{\partial v_h}{\partial z}+\frac{\partial w_h}{\partial y})\right)$$
$$+\frac{\partial\hat{\phi}}{\partial z}\left(\mathbf{D}_{11}\frac{\partial\dot{w}_h}{\partial z}+\mathbf{D}_{12}(\frac{\partial\dot{v}_h}{\partial y}+\frac{\partial\dot{u}_h}{\partial x})+\mathbf{C}_{11}\frac{\partial w_h}{\partial z}+\mathbf{C}_{12}(\frac{\partial u_h}{\partial x}+\frac{\partial v_h}{\partial y})\right)d\boldsymbol{\Omega}_{h,t}$$
$$=-\int\boldsymbol{\Omega}_{h,t}\frac{\partial\hat{\phi}}{\partial z}f d\boldsymbol{\Omega}_{h,t}+\int_{\partial\boldsymbol{\Omega}_{h,t}}\hat{\phi}f n_3 ds,$$

for all $\hat{\phi} \in V_h(t)$, and

$$\frac{\partial}{\partial t}\int_{\Omega_{h,t}} a_h\hat{\psi}d\Omega_{h,t}+\int_{\Omega_{h,t}}(D_a\nabla a_h\cdot\nabla\hat{\psi})d\Omega_{h,t}=\int_{\Omega_{h,t}}(I_h(f(a_h,m_h))\hat{\psi}+a_h\frac{D\hat{\psi}}{Dt})\,d\Omega_{h,t},$$
$$\frac{\partial}{\partial t}\int_{\Omega_{h,t}} m_h\hat{\psi}d\Omega_{h,t}+\int_{\Omega_{h,t}}(D_m\nabla m_h\cdot\nabla\hat{\psi})d\Omega_{h,t}=\int_{\Omega_{h,t}}(I_h(g(a_h,m_h))\hat{\psi}+m_h\frac{D\hat{\psi}}{Dt})\,d\Omega_{h,t}.$$

for all $\hat{\psi} \in V_h(t)$. We can then express u_h, v_h, w_h, a_h and m_h in terms of the linear basis functions:

$$u_h=\sum_{j=1}^{nde}U_j\phi_j,\ v_h=\sum_{j=1}^{nde}V_j\phi_j,\ w_h=\sum_{j=1}^{nde}W_j\phi_j,\ a_h=\sum_{j=1}^{nde}\alpha_j\phi_j \text{ and } m_h=\sum_{j=1}^{nde}\mu_j\phi_j. \tag{A.23}$$

This means that we are left with equations which contain only simple functions and their derivatives and point values for our variables and these are of the form

$$\int_{\mathbf{\Omega}_{h,t}} \Bigg(\mathbf{D}_{11} \frac{\partial \hat{\phi}}{\partial x} \frac{\partial \phi_j}{\partial x} \frac{dU_j}{dt} + \mathbf{D}_{12} \Big(\frac{\partial \hat{\phi}}{\partial x} \frac{\partial \phi_j}{\partial y} \frac{dV_j}{dt} + \frac{\partial \hat{\phi}}{\partial x} \frac{\partial \phi_j}{\partial z} \frac{dW_j}{dt} \Big) + \mathbf{C}_{11} \frac{\partial \hat{\phi}}{\partial x} \frac{\partial \phi_j}{\partial x} U_j + \mathbf{C}_{12} \Big(\frac{\partial \hat{\phi}}{\partial x} \frac{\partial \phi_j}{\partial y} V_j$$
$$+ \frac{\partial \hat{\phi}}{\partial x} \frac{\partial \phi_j}{\partial z} W_j \Big) + \mathbf{D}_{33} \Big(\frac{\partial \hat{\phi}}{\partial y} \frac{\partial \phi_j}{\partial x} \frac{dV_j}{dt} + \frac{\partial \hat{\phi}}{\partial y} \frac{\partial \phi_j}{\partial y} \frac{dU_j}{dt} \Big) + \mathbf{C}_{33} \Big(\frac{\partial \hat{\phi}}{\partial y} \frac{\partial \phi_j}{\partial x} V_j + \frac{\partial \hat{\phi}}{\partial y} \frac{\partial \phi_j}{\partial y} U_j \Big) + \mathbf{D}_{33} \Big(\frac{\partial \hat{\phi}}{\partial z} \frac{\partial \phi_j}{\partial x} \frac{dW_j}{dt}$$
$$+ \frac{\partial \hat{\phi}}{\partial z} \frac{\partial \phi_j}{\partial z} \frac{dU_j}{dt} \Big) + \mathbf{C}_{33} \Big(\frac{\partial \hat{\phi}}{\partial z} \frac{\partial \phi_j}{\partial x} W_j + \frac{\partial \hat{\phi}}{\partial z} \frac{\partial \phi_j}{\partial z} U_j \Big) \Bigg) d\mathbf{\Omega}_t = - \int_{\mathbf{\Omega}_{h,t}} \frac{\partial \hat{\phi}}{\partial x} f d\mathbf{\Omega}_{h,t} + \int_{\partial \mathbf{\Omega}_{h,t}} \hat{\phi} f_i n_1 ds,$$

$$\int_{\mathbf{\Omega}_{h,t}} \Bigg(\mathbf{D}_{33} \Big(\frac{\partial \hat{\phi}}{\partial x} \frac{\partial \phi_j}{\partial x} \frac{dV_j}{dt} + \frac{\partial \hat{\phi}}{\partial x} \frac{\partial \phi_j}{\partial y} \frac{dU_j}{dt} \Big) + \mathbf{C}_{33} \Big(\frac{\partial \hat{\phi}}{\partial x} \frac{\partial \phi_j}{\partial x} V_j + \frac{\partial \hat{\phi}}{\partial x} \frac{\partial \phi_j}{\partial y} U_j \Big) + \mathbf{D}_{11} \frac{\partial \hat{\phi}}{\partial y} \frac{\partial \phi_j}{\partial y} \frac{dV_j}{dt} +$$
$$\mathbf{D}_{12} \Big(\frac{\partial \hat{\phi}}{\partial y} \frac{\partial \phi_j}{\partial x} \frac{dU_j}{dt} + \frac{\partial \hat{\phi}}{\partial y} \frac{\partial \phi_j}{\partial z} \frac{dW_j}{dt} \Big) + \mathbf{C}_{11} \frac{\partial \hat{\phi}}{\partial y} \frac{\partial \phi_j}{\partial y} V_j + \mathbf{C}_{12} \Big(\frac{\partial \hat{\phi}}{\partial y} \frac{\partial \phi_j}{\partial x} U_j + \frac{\partial \hat{\phi}}{\partial y} \frac{\partial \phi_j}{\partial z} W_j \Big) + \mathbf{D}_{33} \Big(\frac{\partial \hat{\phi}}{\partial z} \frac{\partial \phi_j}{\partial y} \frac{dW_j}{dt}$$
$$+ \frac{\partial \hat{\phi}}{\partial z} \frac{\partial \phi_j}{\partial z} \frac{dW_j}{dt} \Big) + \mathbf{C}_{33} \Big(\frac{\partial \hat{\phi}}{\partial z} \frac{\partial \phi_j}{\partial z} W_j + \frac{\partial \hat{\phi}}{\partial z} \frac{\partial \phi_j}{\partial z} V_j \Big) \Bigg) d\mathbf{\Omega}_{h,t} = - \int_{\mathbf{\Omega}_{h,t}} \frac{\partial \hat{\phi}}{\partial y} f d\mathbf{\Omega}_{h,t} + \int_{\partial \mathbf{\Omega}_{h,t}} \hat{\phi} f_i n_2 ds,$$

$$\int_{\mathbf{\Omega}_{h,t}} \Bigg(\mathbf{D}_{33} \Big(\frac{\partial \hat{\phi}}{\partial x} \frac{\partial \phi_j}{\partial x} \frac{dW_j}{dt} + \frac{\partial \hat{\phi}}{\partial x} \frac{\partial \phi_j}{\partial t} \frac{dU_j}{dt} \Big) + \mathbf{C}_{33} \Big(\frac{\partial \hat{\phi}}{\partial x} \frac{\partial \phi_j}{\partial x} W_j + \frac{\partial \hat{\phi}}{\partial x} \frac{\partial \phi_j}{\partial z} U_j \Big) + \mathbf{D}_{33} \Big(\frac{\partial \hat{\phi}}{\partial y} \frac{\partial \phi_j}{\partial z} \frac{dV_j}{dt}$$
$$+ \frac{\partial \hat{\phi}}{\partial y} \frac{\partial \phi_j}{\partial y} \frac{dW_j}{dt} \Big) + \mathbf{C}_{33} \Big(\frac{\partial \hat{\phi}}{\partial y} \frac{\partial \phi_j}{\partial z} V_j + \frac{\partial \hat{\phi}}{\partial y} \frac{\partial \phi_j}{\partial y} W_j \Big) + \mathbf{D}_{11} \frac{\partial \hat{\phi}}{\partial z} \frac{\partial \phi_j}{\partial z} \frac{dW_j}{dt} + \mathbf{D}_{12} \Big(\frac{\partial \hat{\phi}}{\partial z} \frac{\partial \phi_j}{\partial y} \frac{dV_j}{dt} + \frac{\partial \hat{\phi}}{\partial z} \frac{\partial \phi_j}{\partial x} \frac{dU_j}{dt} \Big)$$
$$+ \mathbf{C}_{11} \frac{\partial \hat{\phi}}{\partial z} \frac{\partial \phi_j}{\partial z} W_j + \mathbf{C}_{12} \Big(\frac{\partial \hat{\phi}}{\partial z} \frac{\partial \phi_j}{\partial x} U_j + \frac{\partial \hat{\phi}}{\partial z} \frac{\partial \phi_j}{\partial y} V_j \Big) d\mathbf{\Omega}_{h,t} = - \int \mathbf{\Omega}_{h,t} \frac{\partial \hat{\phi}}{\partial z} f \Bigg) d\mathbf{\Omega}_{h,t} + \int_{\partial \mathbf{\Omega}_{h,t}} \hat{\phi} f_i n_3 ds.$$

The same is done in the reaction-diffusion equations, and we additionally use the transport property of basis functions, $\left(\frac{D\hat{\psi}}{Dt} = 0 \right)$ which is demonstrated in Dziuk and Elliott (2007) and George (2012), to obtain

$$\frac{\partial}{\partial t} \int_{\Omega_{h,t}} \alpha_j \phi_j \hat{\psi} d\Omega_{h,t} + \int_{\Omega_{h,t}} (D_a \alpha_j \nabla \phi_j \cdot \nabla \hat{\psi}) d\Omega_{h,t} = \int_{\Omega_{h,t}} I_h(f(\alpha_j, \mu_j)) \phi_j \hat{\psi} \, d\Omega_{h,t},$$
$$\frac{\partial}{\partial t} \int_{\Omega_{h,t}} \mu_j \phi_j \hat{\psi} d\Omega_{h,t} + \int_{\Omega_{h,t}} (D_m \mu_j \nabla \phi_j \cdot \nabla \hat{\psi}) d\Omega_{h,t} = \int_{\Omega_{h,t}} I_h(g(\alpha_j, \mu_j)) \phi_j \hat{\psi} \, d\Omega_{h,t}.$$

Hence, the force balance equations can be written in block matrix-vector form

$$\begin{bmatrix} \mathbf{A}^{11} & \mathbf{A}^{12} & \mathbf{A}^{13} \\ [\mathbf{A}^{12}]^T & \mathbf{A}^{22} & \mathbf{A}^{23} \\ [\mathbf{A}^{13}]^T & [\mathbf{A}^{23}]^T & \mathbf{A}^{33} \end{bmatrix} \begin{Bmatrix} \frac{\partial \mathbf{U}}{\partial t} \\ \frac{\partial \mathbf{V}}{\partial t} \\ \frac{\partial \mathbf{W}}{\partial t} \end{Bmatrix} + \begin{bmatrix} \mathbf{B}^{11} & \mathbf{B}^{12} & \mathbf{B}^{13} \\ [\mathbf{B}^{12}]^T & \mathbf{B}^{22} & \mathbf{B}^{23} \\ [\mathbf{B}^{13}]^T & [\mathbf{B}^{23}]^T & \mathbf{B}^{33} \end{bmatrix} \begin{Bmatrix} \mathbf{U} \\ \mathbf{V} \\ \mathbf{W} \end{Bmatrix} = \begin{Bmatrix} \mathbf{F}^1 \\ \mathbf{F}^2 \\ \mathbf{F}^3 \end{Bmatrix}, \quad \text{(A.26)}$$

where $\{\mathbf{U}(t)\} = (\mathbf{U}_1(t), ...\mathbf{U}_{nde})$, $\{\mathbf{V}(t)\} = (\mathbf{V}_1(t), ...\mathbf{V}_{nde})$ and:

$$\mathbf{A}_{ij}^{11}(t) := \int_{\mathbf{\Omega}_{h,t}} \mathbf{D}_{11}\frac{\partial\phi_i}{\partial x}\frac{\partial\phi_j}{\partial x} + \mathbf{D}_{33}\left(\frac{\partial\phi_i}{\partial y}\frac{\partial\phi_j}{\partial y} + \frac{\partial\phi_i}{\partial z}\frac{\partial\phi_j}{\partial z}\right) d\mathbf{\Omega}_{h,t},$$

$$\mathbf{A}_{ij}^{22}(t) := \int_{\mathbf{\Omega}_{h,t}} \mathbf{D}_{33}\left(\frac{\partial\phi_i}{\partial x}\frac{\partial\phi_j}{\partial x} + \frac{\partial\phi_i}{\partial z}\frac{\partial\phi_j}{\partial z}\right) + \mathbf{D}_{11}\frac{\partial\phi_i}{\partial y}\frac{\partial\phi_j}{\partial y} d\mathbf{\Omega}_{h,t},$$

$$\mathbf{A}_{ij}^{33}(t) := \int_{\mathbf{\Omega}_{h,t}} \mathbf{D}_{33}\left(\frac{\partial\phi_i}{\partial x}\frac{\partial\phi_j}{\partial x} + \frac{\partial\phi_i}{\partial y}\frac{\partial\phi_j}{\partial y}\right) + \mathbf{D}_{11}\frac{\partial\phi_i}{\partial z}\frac{\partial\phi_j}{\partial z} d\mathbf{\Omega}_{h,t},$$

$$\mathbf{B}_{ij}^{11}(t) := \int_{\mathbf{\Omega}_{h,t}} \mathbf{C}_{11}\frac{\partial\phi_i}{\partial x}\frac{\partial\phi_j}{\partial x} + \mathbf{C}_{33}\left(\frac{\partial\phi_i}{\partial y}\frac{\partial\phi_j}{\partial y} + \frac{\partial\phi_i}{\partial z}\frac{\partial\phi_j}{\partial z}\right) d\mathbf{\Omega}_{h,t},$$

$$\mathbf{B}_{ij}^{22}(t) := \int_{\mathbf{\Omega}_{h,t}} \mathbf{C}_{33}\left(\frac{\partial\phi_i}{\partial x}\frac{\partial\phi_j}{\partial x} + \frac{\partial\phi_i}{\partial z}\frac{\partial\phi_j}{\partial z}\right) + \mathbf{C}_{11}\frac{\partial\phi_i}{\partial y}\frac{\partial\phi_j}{\partial y} d\mathbf{\Omega}_{h,t},$$

$$\mathbf{B}_{ij}^{33}(t) := \int_{\mathbf{\Omega}_{h,t}} \mathbf{C}_{33}\left(\frac{\partial\phi_i}{\partial x}\frac{\partial\phi_j}{\partial x} + \frac{\partial\phi_i}{\partial y}\frac{\partial\phi_j}{\partial y}\right) + \mathbf{C}_{11}\frac{\partial\phi_i}{\partial z}\frac{\partial\phi_j}{\partial z} d\mathbf{\Omega}_{h,t},$$

$$\mathbf{A}_{ij}^{12}(t) := \int_{\mathbf{\Omega}_{h,t}} \mathbf{D}_{12}\frac{\partial\phi_i}{\partial x}\frac{\partial\phi_j}{\partial y} + \mathbf{D}_{33}\frac{\partial\phi_i}{\partial y}\frac{\partial\phi_j}{\partial x} d\mathbf{\Omega}_{h,t}, \quad \mathbf{A}_{ij}^{13}(t) := \int_{\mathbf{\Omega}_{h,t}} \mathbf{D}_{12}\frac{\partial\phi_i}{\partial x}\frac{\partial\phi_j}{\partial z} + \mathbf{D}_{33}\frac{\partial\phi_i}{\partial z}\frac{\partial\phi_j}{\partial x} d\mathbf{\Omega}_{h,t},$$

$$\mathbf{A}_{ij}^{23}(t) := \int_{\mathbf{\Omega}_{h,t}} \mathbf{D}_{12}\frac{\partial\phi_i}{\partial y}\frac{\partial\phi_j}{\partial z} + \mathbf{D}_{33}\frac{\partial\phi_i}{\partial z}\frac{\partial\phi_j}{\partial y} d\mathbf{\Omega}_{h,t}, \quad \mathbf{B}_{ij}^{12}(t) := \int_{\mathbf{\Omega}_{h,t}} \mathbf{C}_{12}\frac{\partial\phi_i}{\partial x}\frac{\partial\phi_j}{\partial y} + \mathbf{C}_{33}\frac{\partial\phi_i}{\partial y}\frac{\partial\phi_j}{\partial x} d\mathbf{\Omega}_{h,t},$$

$$\mathbf{B}_{ij}^{13}(t) := \int_{\mathbf{\Omega}_{h,t}} \mathbf{C}_{12}\frac{\partial\phi_i}{\partial x}\frac{\partial\phi_j}{\partial z} + \mathbf{C}_{33}\frac{\partial\phi_i}{\partial z}\frac{\partial\phi_j}{\partial x} d\mathbf{\Omega}_{h,t}, \quad \mathbf{B}_{ij}^{23}(t) := \int_{\mathbf{\Omega}_{h,t}} \mathbf{C}_{12}\frac{\partial\phi_i}{\partial y}\frac{\partial\phi_j}{\partial z} + \mathbf{C}_{33}\frac{\partial\phi_i}{\partial z}\frac{\partial\phi_j}{\partial y} d\mathbf{\Omega}_{h,t},$$

$$\mathbf{F}_i^1(t) := -\int_{\Omega_{h,t}} f\frac{\partial\phi_i}{\partial x} d\Omega_{h,t} + \int_{\partial\Omega_{h,t}} n_1 f_i\phi_i ds, \qquad \mathbf{F}_i^2(t) := -\int_{\Omega_{h,t}} f\frac{\partial\phi_i}{\partial y} d\Omega_{h,t} + \int_{\partial\Omega_{h,t}} n_2 f_i\phi_i ds,$$

$$\mathbf{F}_i^3(t) := -\int_{\Omega_{h,t}} f\frac{\partial\phi_i}{\partial z} d\Omega_{h,t} + \int_{\partial\Omega_{h,t}} n_3 f_i\phi_i ds.$$

For convenience in notation and computation we have the block matrices and vectors

$$[\mathbf{A}] := \begin{bmatrix} \mathbf{A}^{11} & \mathbf{A}^{12} & \mathbf{A}^{13} \\ [\mathbf{A}^{12}]^T & \mathbf{A}^{22} & \mathbf{A}^{23} \\ [\mathbf{A}^{13}]^T & [\mathbf{A}^{23}]^T & \mathbf{A}^{33} \end{bmatrix}, \; [\mathbf{B}] := \begin{bmatrix} \mathbf{B}^{11} & \mathbf{B}^{12} & \mathbf{B}^{13} \\ [\mathbf{B}^{12}]^T & \mathbf{B}^{22} & \mathbf{B}^{23} \\ [\mathbf{B}^{13}]^T & [\mathbf{B}^{23}]^T & \mathbf{B}^{33} \end{bmatrix}, \tag{A.28a}$$

$$\{\mathbf{U}\} := \begin{Bmatrix} \mathbf{U} \\ \mathbf{V} \\ \mathbf{W} \end{Bmatrix} \text{ and } \{\mathbf{F}\} := \begin{Bmatrix} \mathbf{F}^1 \\ \mathbf{F}^2 \\ \mathbf{F}^3 \end{Bmatrix}. \tag{A.28b}$$

Therefore the force balance equation's semi-discrete finite element formation can be written compactly as

$$[\mathbf{A}]\frac{\partial\{\mathbf{U}\}}{\partial t} + [\mathbf{B}]\{\mathbf{U}\} = \{\mathbf{F}\}. \tag{A.29}$$

Now considering the reaction kinetics to be as in Section 4.2.1 we can similarly write the reaction-diffusion equations in semi-discrete form

$$\frac{\partial}{\partial t}(\mathbf{M}\boldsymbol{\alpha}) + D_a\mathbf{K}\boldsymbol{\alpha} = k_a a_c\mathbf{H} - k_a\mathbf{M}\boldsymbol{\alpha} + k_{am}\frac{\boldsymbol{\alpha}(1-\boldsymbol{\mu})}{1+K\boldsymbol{\alpha}^2}\mathbf{M}, \tag{A.30a}$$

$$\frac{\partial}{\partial t}(\mathbf{M}\boldsymbol{\mu}) + D_m\mathbf{K}\boldsymbol{\mu} = -k_{ma}a_c\mathbf{H} + k_{ma}\mathbf{M}\boldsymbol{\alpha} - k_{am}\frac{\boldsymbol{\alpha}(1-\boldsymbol{\mu})}{1+K\boldsymbol{\alpha}^2}\mathbf{M}, \tag{A.30b}$$

where

$$M_{i,j} = \int_{\Omega_{h,t}} \phi_i\phi_j, \quad K_{i,j} = \int_{\Omega_{h,t}} \nabla\phi_i\cdot\nabla\phi_j \quad \text{and} \quad H_j = \int_{\Omega_{h,t}} \phi_j. \tag{A.31}$$

To compute these integrals we use Gauss numerical quadrature (Press et al., 2007). This is done as follows. First we can consider the integrals elementwise,

$$M_{i,j} = \sum_{\Delta_k} \int_{\Delta_k} \phi_i \phi_j, \quad K_{i,j} = \sum_{\Delta_k} \int_{\Delta_k} \nabla\phi_i \cdot \nabla\phi_j \quad \text{and} \quad H_j = \sum_{\Delta_k} \int_{\Delta_k} \phi_j. \tag{A.32}$$

Then choose a numerical quadrature, this is a set of points and weights. This can be written as a formula for the integral of a function ξ

$$\int \xi(\boldsymbol{x}) \approx \sum_q \xi(\bar{\boldsymbol{x}}_q) w_q, \tag{A.33}$$

where $\bar{\boldsymbol{x}}_q$ and w_q are the qth quadrature points and weights respectively. Therefore the integrals can be approximated by

$$\begin{aligned} M_{i,j} \approx \sum_{\Delta_k} \sum_q \phi_i(\bar{\boldsymbol{x}}_q)\phi_j(\bar{\boldsymbol{x}}_q) w_q, \quad K_{i,j} \approx \sum_{\Delta_k} \sum_q \nabla\phi_i(\bar{\boldsymbol{x}}_q) \cdot \nabla\phi_j(\bar{\boldsymbol{x}}_q) w_q \\ \text{and} \quad H_j \approx \sum_{\Delta_k} \sum_q \phi_j(\bar{\boldsymbol{x}}_q) w_q. \end{aligned} \tag{A.34}$$

A.2.3 Time discretisation

Next we carry out the temporal discretisation of the system of ordinary differential equations arising from the finite element discretisation. To proceed, we split the interval into a finite number of subintervals $[t^n, t^{n+1}]$ use a uniform time step $\Delta t := t^{n+1} - t^n$. We can then use a modified implicit finite differentiation formula (forward Euler) (Lakkis et al., 2013; Madzvamuse, 2006; Ruuth, 1995). Thus the fully discrete problem is now

$$\left([\mathbf{A}]^n + \Delta t [\mathbf{B}]^n\right) \mathbf{U}^{n+1} = [\mathbf{A}]^n \{\mathbf{U}\}^n + \Delta t \{\mathbf{F}\}^n, \tag{A.35a}$$

$$\left[\mathbf{M}^{n+1} + \Delta t D_a \mathbf{K}^{n+1}\right] \boldsymbol{\alpha}^{n+1} = \mathbf{M}^n \boldsymbol{\alpha}^n + \Delta t \left(k_a (a_c \mathbf{H}^n - \mathbf{M}^n \boldsymbol{\alpha}^n) + k_{am} \frac{\boldsymbol{\alpha}^n (1 - \boldsymbol{\mu}^n)}{1 + K(\boldsymbol{\alpha}^n)^2} \mathbf{M}^n\right), \tag{A.35b}$$

$$\left[\mathbf{M}^{n+1} + \Delta t D_m \mathbf{K}^{n+1}\right] \boldsymbol{\mu}^{n+1} = \mathbf{M}^n \boldsymbol{\mu}^n + \Delta t \left(-k_{ma} (a_c \mathbf{H}^n - \mathbf{M}^n \boldsymbol{\alpha}^n) - k_{am} \frac{\boldsymbol{\alpha}^n (1 - \boldsymbol{\mu}^n)}{1 + K(\boldsymbol{\alpha}^n)^2} \mathbf{M}^n\right), \tag{A.35c}$$

where the superscripts ^{n} and $^{n+1}$ are the computed values on the mesh at times t^n and t^{n+1} respectively.

Hence we have three equations all with the same form. At each time-step we assemble the matrices to obtain a system of linear algebraic equations. When solving (A.35a) we see that the block matrix on the left hand side is not symmetric therefore we use the most effective solver for this which is GMRES (Saad and Schultz, 1986). The equations (A.35b) and (A.35c) are solved using the conjugate gradient method (Hestenes and Stiefel, 1952).

Nodal displacements

The displacement of the nodes of the mesh is chosen to be equal to the flow velocity therefore $\boldsymbol{\beta} := \frac{\partial \mathbf{U}}{\partial t}$. Letting $t^{n+1} = t^n + \Delta t$ and $\boldsymbol{x}(t^n) \in \boldsymbol{\Omega}_{t^n}, \boldsymbol{x}(t^{n+1}) \in \boldsymbol{\Omega}_{t^{n+1}}$ be points in the respective domains. We can define a first order linear approximation as:

$$\boldsymbol{\beta}(\boldsymbol{x}, t^n) = \frac{\boldsymbol{x}(t^{n+1}) - \boldsymbol{x}(t^n)}{\Delta t}. \tag{A.36}$$

This means we can define a new approximation to the domain $\boldsymbol{\Omega}_{t^{n+1}}$ such that

$$\boldsymbol{x}(t^{n+1}) = \boldsymbol{x}(t^n) + \Delta t \frac{\partial \mathbf{U}}{\partial t} = \boldsymbol{x}(t^n) + (\mathbf{U}^{t+1} - \mathbf{U}^t). \tag{A.37}$$

At each step we have a new mesh with new shape functions so we must assemble new matrices $\mathbf{M}^n, \mathbf{H}^n, \mathbf{A}^n, \mathbf{B}^n, \mathbf{F}^n$ to iteratively solve the discrete coupled problem.

Numerical algorithm

The fully discrete problem is solved iteratively with the following algorithm:

- Initialise $\mathbf{U}$, $\boldsymbol{\alpha}$ and fixed parameters
- WHILE $t < endtime$
  - Assemble $\mathbf{M}^n, \mathbf{H}^n, \mathbf{A}^n, \mathbf{B}^n, \mathbf{F}^n$
  - Solve for $\mathbf{U}^{n+1}$ using (A.35a)
  - Compute the new domain from $\mathbf{U}^{n+1}$
  - Solve for $\boldsymbol{\alpha}^{n+1}$ and $\boldsymbol{\mu}^{n+1}$ using (A.35b) and (A.35c)
  - $t = t + \Delta t$
- END

We create a mesh using Gmsh (Geuzaine and Remacle, 2009) and implement this algorithm using deal.II (Bangerth et al., 2016), a C++ software library which provides tools to solve partial differential equations which are discretised with finite element methods. Unlike the majority of other finite element software, deal.II uses hexahedral and quadrilateral elements rather than triangles and tetrahedra. The main advantage is that these shapes can provide better approximation quality with same number of degrees of freedom as triangular meshes. One disadvantage is that it is harder to find an adaptive finite element method without hanging nodes.

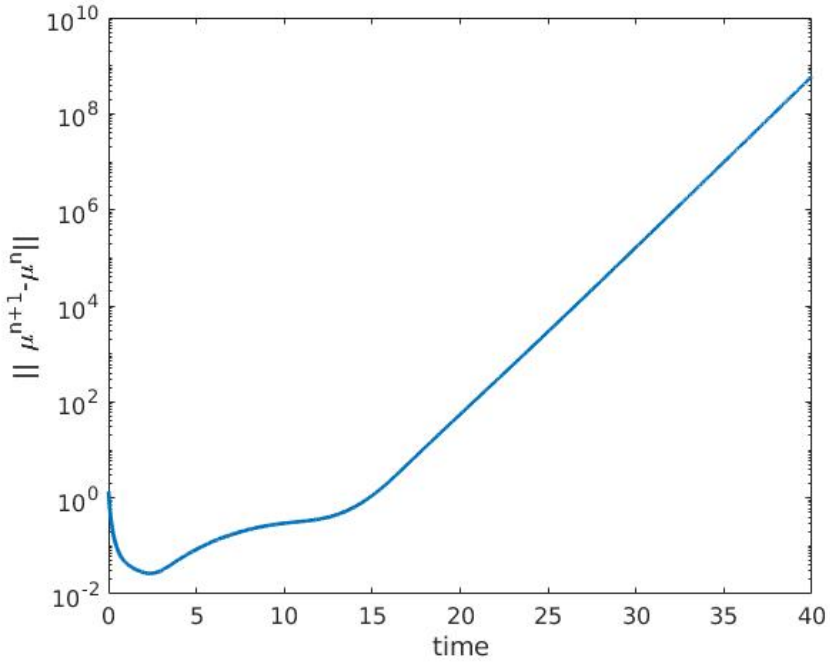

Figure A.1: Plot of the divergence of solutions for the example in Section 4.6.2. There is an initial decrease in difference between the solutions due to diffusion, then the mode grows exponentially.

A.2.4 L_2 norms

In Figure A.1 we plot the norm of the difference between successive solutions for the example in Section 4.6.2, where just the reaction-diffusion system is solved, and see that there is exponential growth. In Figure A.2 we plot the norm of differences between successive solutions in the case of the full system example in Section 4.8.4. We see an increase, or decrease, in the L_2 norm when the rate of deformation is accelerating, or decelerating, respectively. The qualitative changes in the L_2 norms are similar, but the changes in myosin and displacement appear slightly later than actin. This may suggest, in this example, that the change in actin triggers the change in the other variables.

A.3 Summary

In this chapter we have outlined a moving grid finite element method which we use to solve the equations of our mechanobiochemical cell motility model (Baines, 1994; Madzvamuse et al., 2003). The formulation is based on the construction of George (2012); Madzvamuse and George (2013). The block matrices which make up the discretised form of the force balance equation are now bigger and more complex than the case in two dimensions.

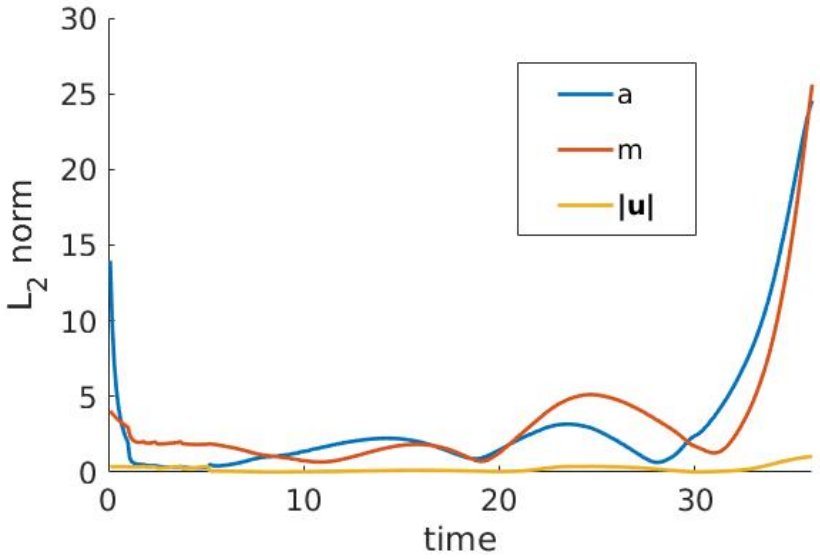

Figure A.2: Plot of the L_2 norm of difference between successive solutions for the example shown in Figure 4.11. There is an initial decrease due to diffusion, increases when the deformation is accelerating and decreases as deformation decelerates.

In most of the numerical solutions in Sections 3.6 and 4.8 the cell becomes deformed in such a way that means the mesh becomes unreliable and eventually breaks. In this case, re-meshing the deformed geometries with new elements of more regular shape would be very useful to obtain more accurate solutions and in order to see what may happen for larger time.

Bibliography

Abercrombie, M.

1980. The Croonian lecture, 1978 - the crawling movement of metazoan cells. *Proc. R. Soc. Lond. B*, 207(1167):129–147. 7

Acheson, D.

1990. *Elementary fluid dynamics: Oxford applied mathematics and computing science series*. Oxford: Oxford University Press. 61

Aguilar-Cuenca, R., A. Juanes-García, and M. Vicente-Manzanares

2014. Myosin II in mechanotransduction: master and commander of cell migration, morphogenesis, and cancer. *Cellular and molecular life sciences*, 71(3):479–492. 9, 17

Alberts, B., A. Johnson, J. Lewis, P. Walter, M. Raff, and K. Roberts

2002. *Molecular Biology of the Cell 4th Edition*. New York: Garland Science. 1, 4

Allen, R. D.

1981. Motility. *The Journal of Cell Biology*, 91(3):148s–155s. 3

Alt, W. and M. Dembo

1999. Cytoplasm dynamics and cell motion: two-phase flow models. *Mathematical biosciences*, 156(1):207–228. 6

Alt, W. and R. T. Tranquillo

1995. Basic morphogenetic system modeling shape changes of migrating cells: How to explain fluctuating lamellipodial dynamics. *Journal of Biological Systems*, 3(04):905–916. 12, 19, 59, 60

Ananthakrishnan, R. and A. Ehrlicher

2007. The forces behind cell movement. *International journal of biological sciences*, 3(5):303. 6

Arfken, G., H. Weber, and F. Harris

2013. *Mathematical methods for physicists*. Amsterdam: Elsevier. 28, 42, 46

Atilgan, E., D. Wirtz, and S. X. Sun

2005. Morphology of the lamellipodium and organization of actin filaments at the leading edge of crawling cells. *Biophysical journal*, 89(5):3589–3602. 11

Atilgan, E., D. Wirtz, and S. X. Sun

2006. Mechanics and dynamics of actin-driven thin membrane protrusions. *Biophysical journal*, 90(1):65–76. 7, 11

Baines, M. J.

1994. *Moving finite elements, Monographs on Numerical Analysis*. Oxford: Clarendon Press. 21, 22, 116

Bangerth, W., T. Heister, L. Heltai, G. Kanschat, M. Kronbichler, M. Maier, and B. Turcksin

2016. The deal.ii library, version 8.3. *Archive of Numerical Software*, 4(100):1–11. 42, 45, 67, 103, 115

Bard, J. and I. Lauder

1974. How well does Turing's theory of morphogenesis work? *J. Theor. Biol*, 45:501–531. 51

Barreira, R., C. Elliott, and A. Madzvamuse

2011. The surface finite element method for pattern formation on evolving biological surfaces. *J. Math. Biol.*, 63(6):1095–1119. 39, 53, 58

Barzilai, S., S. K. Yadav, S. Morrell, F. Roncato, E. Klein, L. Stoler-Barak, O. Golani, S. W. Feigelson, A. Zemel, S. Nourshargh, et al.

2017. Leukocytes breach endothelial barriers by insertion of nuclear lobes and disassembly of endothelial actin filaments. *Cell reports*, 18(3):685–699. 10

Bausch, A. R., F. Ziemann, A. A. Boulbitch, K. Jacobson, and E. Sackmann

1998. Local measurements of viscoelastic parameters of adherent cell surfaces by magnetic bead microrheometry. *Biophysical journal*, 75(4):2038–2049. 64

Beckett, G. and J. Mackenzie

2001. On a uniformly accurate finite difference approximation of a singularly perturbed

reaction-diffusion problem using grid equidistribution. *J Comput Appl Math*, 131(1-2):381–405. 39

Bendix, P. M., G. H. Koenderink, D. Cuvelier, Z. Dogic, B. N. Koeleman, W. M. Brieher, C. M. Field, L. Mahadevan, and D. A. Weitz

2008. A quantitative analysis of contractility in active cytoskeletal protein networks. *Biophysical journal*, 94(8):3126–3136. 17, 77

Benguria, R.

2015. Neumann eigenvalue - encyclopedia of mathematics. https://www.encyclopediaofmath.org/. Accessed: 2016-03-03. 40

Berg, J., J. Tymoczko, G. Gatto, and L. Stryer

2015. *Biochemistry (Eighth ed.)*. New York: W.H. Freeman & Company, a Macmillan Education Imprint. 1

Bershadsky, A., M. Kozlov, and B. Geiger

2006. Adhesion-mediated mechanosensitivity: a time to experiment, and a time to theorize. *Current opinion in cell biology*, 18(5):472–481. 7

Blazakis, K. N.

2015. *Computational methods for investigating cell motility with applications to neutrophil cell migration*. PhD thesis, University of Sussex. 12, 20

Bottino, D., A. Mogilner, T. Roberts, M. Stewart, and G. Oster

2002. How nematode sperm crawl. *Journal of cell science*, 115(2):367–384. 20

Bottino, D. C. and L. J. Fauci

1998. A computational model of ameboid deformation and locomotion. *European Biophysics Journal*, 27(5):532–539. 19, 20

Bozzini, B., D. Lacitignola, C. Mele, and I. Sgura

2012. Coupling of morphology and chemistry leads to morphogenesis in electrochemical metal growth: a review of the reaction-diffusion approach. *Acta applicandae mathematicae*, 122(1):53–68. 26

Bray, D.

2001. *Cell movements: from molecules to motility*. Garland Science. 1, 3, 5, 6, 7

Brinkmann, V., U. Reichard, C. Goosmann, B. Fauler, Y. Uhlemann, D. S. Weiss, Y. Weinrauch, and A. Zychlinsky

2004. Neutrophil extracellular traps kill bacteria. *science*, 303(5663):1532–1535. 1, 3

Caille, N., O. Thoumine, Y. Tardy, and J.-J. Meister

2002. Contribution of the nucleus to the mechanical properties of endothelial cells. *Journal of biomechanics*, 35(2):177–187. 12, 16

Calero-Cuenca, F. J., C. S. Janota, and E. R. Gomes

2018. Dealing with the nucleus during cell migration. *Current opinion in cell biology*, 50:35–41. 10

Camley, B. A., Y. Zhao, B. Li, H. Levine, and W.-J. Rappel

2017. Crawling and turning in a minimal reaction-diffusion cell motility model: coupling cell shape and biochemistry. *Physical Review E*, 95(1):012401. 12, 16, 17, 75

Campbell, E. J. and P. Bagchi

2018. A computational model of amoeboid cell motility in the presence of obstacles. *Soft matter*. 12, 15, 20

Cao, X., E. Moeendarbary, P. Isermann, P. M. Davidson, X. Wang, M. B. Chen, A. K. Burkart, J. Lammerding, R. D. Kamm, and V. B. Shenoy

2016. A chemomechanical model for nuclear morphology and stresses during cell transendothelial migration. *Biophysical Journal*, 111(7):1541–1552. 10, 12, 16, 72

Carlier, M.-F., J. Pernier, P. Montaville, S. Shekhar, S. Kühn, and Cytoskeleton Dynamics and Motility group

2015. Control of polarized assembly of actin filaments in cell motility. *Cellular and Molecular Life Sciences*, 72(16):3051–3067. x, 5, 6, 7

Carlin, L. M., E. G. Stamatiades, C. Auffray, R. N. Hanna, G. Glover, Leanne anaxisymmetricd Vizcay-Barrena, C. C. Hedrick, H. T. Cook, S. Diebold, and F. Geissmann

2013. Nr4a1-dependent Ly6C low monocytes monitor endothelial cells and orchestrate their disposal. *Cell*, 153(2):362–375. 7

Castets, V., E. Dulos, J. Boissonade, and P. De Kepper

1990. Experimental evidence of a sustained standing turing-type nonequilibrium chemical pattern. *Physical Review Letters*, 64(24):2953. 17

Chambers, A. F., A. C. Groom, and I. C. MacDonald

2002. Metastasis: dissemination and growth of cancer cells in metastatic sites. *Nature Reviews Cancer*, 2(8):563. 4

Chan, C. J., A. E. Ekpenyong, S. Golfier, W. Li, K. J. Chalut, O. Otto, J. Elgeti, J. Guck, and F. Lautenschläger

2015. Myosin II activity softens cells in suspension. *Biophysical journal*, 108(8):1856–1869. 8

Chaplain, M.

1995. Reaction-diffusion prepatterning and its potential role in tumor invasion. *J. Bio. Sys.*, 03(04):929–936. 26, 27

Chaplain, M., M. Ganesh, and I. Graham

2001. Spatio-temporal pattern formation on spherical surfaces: numerical simulation and application to solid tumour growth. *J Math Biol*, 42(5):387–423. 26, 32, 39, 53

Charras, G.

2008. A short history of blebbing. *Journal of microscopy*, 231(3):466–478. 10

Chen, B.-C., W. R. Legant, K. Wang, L. Shao, D. E. Milkie, M. W. Davidson, C. Janetopoulos, X. S. Wu, J. A. Hammer, Z. Liu, B. P. English, Y. Mimori-Kiyosue, D. P. Romero, A. T. Ritter, J. Lippincott-Schwartz, L. Fritz-Laylin, R. D. Mullins, D. M. Mitchell, J. N. Bembenek, A.-C. Reymann, R. Böhme, S. W. Grill, J. T. Wang, G. Seydoux, U. S. Tulu, D. P. Kiehart, and E. Betzig

2014. Lattice light-sheet microscopy: Imaging molecules to embryos at high spatiotemporal resolution. *Science*, 346(6208). 72

Chen, J., J. Irianto, S. Inamdar, P. Pravincumar, D. Lee, D. L. Bader, and M. Knight

2012. Cell mechanics, structure, and function are regulated by the stiffness of the three-dimensional microenvironment. *Biophysical journal*, 103(6):1188–1197. 12, 16, 20

Condeelis, J. and J. E. Segall

2003. Intravital imaging of cell movement in tumours. *Nature Reviews Cancer*, 3(12):921. 1, 4

Cooper, G.

2000. *The Cell: A Molecular Approach. 2nd edition.* Sunderland (MA): Sinauer Associates. 1, 3, 4, 5, 6

Courant, R.

1943. Variational methods for the solution of problems of equilibrium and vibrations. *Bulletin of the American mathematical Society*, 49(1):1–23. 21

Croft, W., C. Elliott, G. Ladds, B. Stinner, C. Venkataraman, and C. Weston

2014. Parameter identification problems in the modelling of cell motility. *J. Math. Biol.*, 71(2):399–436. 39

Cross, M. C. and P. C. Hohenberg

1993. Pattern formation outside of equilibrium. *Reviews of modern physics*, 65(3):851. 87

Cunningham, C. C.

1995. Actin polymerization and intracellular solvent flow in cell surface blebbing. *Journal of cell biology*, 129(6):1589–1600. 10

Cusseddu, D., L. Edelstein-Keshet, J. Mackenzie, S. Portet, and A. Madzvamuse

2018. A coupled bulk-surface model for cell polarisation. *Journal of Theoretical Biology*. 104

Dale, P. and P. Maini

1994. Mathematical modeling of corneal epithelial wound healing. *Mathematical Biosciences*, 124(2):127–147. 26

Darling, E. M., S. Zauscher, J. A. Block, and F. Guilak

2007. A thin-layer model for viscoelastic, stress-relaxation testing of cells using atomic force microscopy: do cell properties reflect metastatic potential? *Biophysical journal*, 92(5):1784–1791. 12, 16

Dhillon, D. S. J., M. C. Milinkovitch, and M. Zwicker

2017. Bifurcation analysis of reaction diffusion systems on arbitrary surfaces. *Bulletin of mathematical biology*, 79(4):788–827. 39

DiMilla, P., K. Barbee, and D. Lauffenburger

1991. Mathematical model for the effects of adhesion and mechanics on cell migration speed. *Biophysical journal*, 60(1):15–37. 11, 12, 16

Dreher, A., I. S. Aranson, and K. Kruse

2014. Spiral actin-polymerization waves can generate amoeboidal cell crawling. *New Journal of Physics*, 16(5):055007. 12, 16

Du, Q., C. Liu, and X. Wang

2006. Simulating the deformation of vesicle membranes under elastic bending energy in three dimensions. *Journal of Computational Physics*, 212(2):757–777. 12, 20

Dziuk, G.

1988. Finite elements for the beltrami operator on arbitrary surfaces. In *Partial Differential Equations and Calculus of Variations Vol. 1357 of Lecture Notes in Mathematics*, S. Hildebrandt and R. Leis, eds., Pp. 142–155. Springer. 53

Dziuk, G. and C. Elliott

2013. Finite element methods for surface PDEs. *Acta Numerica*, 22:289–396. 31, 53

Dziuk, G. and C. M. Elliott

2007. Finite elements on evolving surfaces. *IMA journal of numerical analysis*, 27(2):262–292. 112

Eisenbach, M.

2004. *Chemotaxis*. World Scientific Publishing Company. 3

Elliott, C. and T. Ranner

2014. A computational approach to an optimal partition problem on surfaces. *Interface Free Bound*, 17(3):353–379. 53

Elliott, C., B. Stinner, and C. Venkataraman

2012. Modelling cell motility and chemotaxis with evolving surface finite elements. *J. Roy. Soc. Interface*, 9(76):3027–3044. 12, 15, 20, 21, 39, 53, 58, 104

Elliott, C. M. and T. Ranner

2013. Finite element analysis for a coupled bulk–surface partial differential equation. *IMA Journal of Numerical Analysis*, 33(2):377–402. 104

Even-Ram, S. and K. M. Yamada

2005. Cell migration in 3D matrix. *Current opinion in cell biology*, 17(5):524–532. 10

Fackler, O. T. and R. Grosse

2008. Cell motility through plasma membrane blebbing. *The Journal of cell biology*, 181(6):879–884. 10

Friedl, P.

2004. Prespecification and plasticity: shifting mechanisms of cell migration. *Current opinion in cell biology*, 16(1):14–23. 104

Friedl, P., S. Borgmann, and E.-B. Bröcker

2001. Amoeboid leukocyte crawling through extracellular matrix: lessons from the dictyostelium paradigm of cell movement. *Journal of leukocyte biology*, 70(4):491–509. 10

Friedl, P. and D. Gilmour

2009. Collective cell migration in morphogenesis, regeneration and cancer. *Nature reviews Molecular cell biology*, 10(7):445–457. 1, 3, 10

Friedl, P., E. Sahai, S. Weiss, and K. M. Yamada

2012. New dimensions in cell migration. *Nature reviews Molecular cell biology*, 13(11):743. 102

Friedl, P. and K. Wolf

2009. Plasticity of cell migration: a multiscale tuning model. *The Journal of cell biology*, Pp. jcb–200909003. 3

Friedl, P., K. Wolf, and J. Lammerding

2011. Nuclear mechanics during cell migration. *Current opinion in cell biology*, 23(1):55–64. 10

Garvie, M., P. Maini, and C. Trenchea

2010. An efficient and robust numerical algorithm for estimating parameters in turing systems. *Journal of Computational Physics*, 229(19):7058–7071. 39

Gatenby, R. and E. Gawlinski

1996. A reaction-diffusion model of cancer invasion. *Cancer research*, 56(24):5745–5753. 26

George, U. Z.

2012. *A numerical approach to studying cell dynamics*. PhD thesis, University of Sussex. 6, 12, 17, 19, 20, 22, 26, 38, 40, 59, 60, 64, 74, 79, 89, 102, 103, 112, 116

George, U. Z., A. Stéphanou, and A. Madzvamuse

2013. Mathematical modelling and numerical simulations of actin dynamics in the eukaryotic cell. *Journal of mathematical biology*, Pp. 1–47. 19, 24, 64, 65, 67, 72, 102

Geuzaine, C. and J.-F. Remacle

2009. Gmsh: A 3-D finite element mesh generator with built-in pre-and post-processing

facilities. *International journal for numerical methods in engineering*, 79(11):1309–1331. 115

Gierer, A. and H. Meinhardt

1972. A theory of biological pattern formation. *Kybernetik*, 12(1):30–39. 17, 37

Gladilin, E., A. Micoulet, B. Hosseini, K. Rohr, J. Spatz, and R. Eils

2007. 3D finite element analysis of uniaxial cell stretching: from image to insight. *Physical biology*, 4(2):104. 12, 16, 20

Golub, G. and C. Van Loan

1993. *Matrix computations*. Baltimore: The John Hopkins University Press. 42

Gordon, C., D. Webb, and S. Wolpert

1992. Isospectral plane domains and surfaces via riemannian orbifolds. *Inventiones mathematicae*, 110(1):1–22. 32

Gracheva, M. E. and H. G. Othmer

2004. A continuum model of motility in ameboid cells. *Bulletin of mathematical biology*, 66(1):167–193. 11, 12, 17, 18, 75, 77

Haider, M. A. and F. Guilak

2002. An axisymmetric boundary integral model for assessing elastic cell properties in the micropipette aspiration contact problem. *Journal of Biomechanical Engineering*, 124(5):586–595. 20

Hall, A.

1998. Rho gtpases and the actin cytoskeleton. *Science*, 279(5350):509–514. 104

Hawkins, R. J., R. Poincloux, O. Bénichou, M. Piel, P. Chavrier, and R. Voituriez

2011. Spontaneous contractility-mediated cortical flow generates cell migration in three-dimensional environments. *Biophysical Journal*, 101(5):1041–1045. 12, 14, 17, 18, 75

Hestenes, M. R. and E. Stiefel

1952. Methods of conjugate gradients for solving linear systems. *J Res Nat Bur Stand*, 49(6):409–436. 42, 114

Hillen, T. and K. J. Painter

2009. A user's guide to PDE models for chemotaxis. *Journal of mathematical biology*, 58(1-2):183. 18

Hobson, E. W.

1931. *The theory of spherical and ellipsoidal harmonics*. CUP Archive. 49

Hodge, N. and P. Papadopoulos

2012. Continuum modeling and numerical simulation of cell motility. *Journal of mathematical biology*, 64(7):1253–1279. 17, 18, 75, 77

Holmes, W. R. and L. Edelstein-Keshet

2012. A comparison of computational models for eukaryotic cell shape and motility. *PLoS Comput Biol*, 8(12):e1002793. 14

Holmes, W. R., A. E. Golding, W. M. Bement, and L. Edelstein-Keshet

2016. A mathematical model of GTPase pattern formation during single-cell wound repair. *Interface focus*, 6(5):20160032. 104

Hunding, A.

1992. Pattern formation of reaction-diffusion systems in 3 space coordinates. supercomputer simulation of drosophila morphogenesis. *Physica A: Statistical Mechanics and its Applications*, 188(1-3):172–177. 26

Johnson, C.

1987. *Numerical Solution of Partial Differential Equations by the Finite Element Method*. Cambridge University Press. 25, 39

Kac, M.

1966. Can one hear the shape of a drum? *The american mathematical monthly*, 73(4):1–23. 32

Karcher, H., J. Lammerding, H. Huang, R. T. Lee, R. D. Kamm, and M. R. Kaazempur-Mofrad

2003. A three-dimensional viscoelastic model for cell deformation with experimental verification. *Biophysical journal*, 85(5):3336–3349. 12, 16

Katti, D. R. and K. S. Katti

2017. Cancer cell mechanics with altered cytoskeletal behavior and substrate effects: A 3D finite element modeling study. *Journal of the mechanical behavior of biomedical materials*, 76:125–134. 8, 12, 21

Kovács, M., J. Tóth, C. Hetényi, A. Málnási-Csizmadia, and J. R. Sellers

2004. Mechanism of blebbistatin inhibition of myosin II. *Journal of Biological Chemistry*, 279(34):35557–35563. 7

Kreyszig, E.

1978. *Introductory functional analysis with applications.* New York: Wiley. 40

Krinsky, V.

1983. Self-organization. autowaves and structures far from equilibrium. In *Proceedings of an International Sympusium Pushchino, USSR, July 18-23, 1983*. Springer-Verlag. 26

Lacitignola, D., B. Bozzini, M. Frittelli, and I. Sgura

2017. Turing pattern formation on the sphere for a morphochemical reaction-diffusion model for electrodeposition. *Communications in Nonlinear Science and Numerical Simulation*, 48:484–508. 54

Lakkis, O., A. Madzvamuse, and C. Venkataraman

2013. Implicit–explicit timestepping with finite element approximation of reaction–diffusion systems on evolving domains. *SIAM Journal on Numerical Analysis*, 51(4):2309–2330. 42, 58, 106, 114

Larripa, K. and A. Mogilner

2006. Transport of a 1D viscoelastic actin–myosin strip of gel as a model of a crawling cell. *Physica A: Statistical Mechanics and its Applications*, 372(1):113–123. 12, 16

Lee, J., A. Ishihara, J. A. Theriot, and K. Jacobson

1993. Principles of locomotion for simple-shaped cells. *Nature*, 362(6416):167. 12, 13

Levchenko, A. and P. A. Iglesias

2002. Models of eukaryotic gradient sensing: application to chemotaxis of amoebae and neutrophils. *Biophysical journal*, 82(1):50–63. 17

Lewis, M. and J. Murray

1991. Analysis of stable two-dimensional patterns in contractile cytogel. *Journal of Nonlinear Science*, 1(3):289–311. 12, 16, 59, 61

MacDonald, G., J. A. Mackenzie, M. Nolan, and R. Insall

2016. A computational method for the coupled solution of reaction–diffusion equations on evolving domains and manifolds: Application to a model of cell migration and chemotaxis. *Journal of computational physics*, 309:207–226. 12, 18, 20, 21, 104

Mackenzie, J., M. Nolan, and R. Insall

2016. Local modulation of chemoattractant concentrations by single cells: dissection using a bulk-surface computational model. *Interface focus*, 6(5):20160036. 18

Madzvamuse, A.

2000. *A numerical approach to the study of spatial pattern formation.* PhD thesis, University of Oxford. 27, 32, 38, 40, 42, 61, 110

Madzvamuse, A.

2006. Time-stepping schemes for moving grid finite elements applied to reaction–diffusion systems on fixed and growing domains. *J Comput Phys*, 214(1):239–263. 21, 42, 58, 106, 114

Madzvamuse, A. and A. Chung

2016. The bulk-surface finite element method for reaction–diffusion systems on stationary volumes. *Finite Elem Anal Des*, 108:9–21. 53, 104

Madzvamuse, A., E. Gaffney, and P. Maini

2010. Stability analysis of non-autonomous reaction-diffusion systems: the effects of growing domains. *J Math Biol*, 61(1):133–164. 37

Madzvamuse, A. and U. Z. George

2013. The moving grid finite element method applied to cell movement and deformation. *Finite Elements in Analysis and Design*, 74:76–92. 19, 21, 102, 116

Madzvamuse, A., H. Ndakwo, and R. Barreira

2015. Cross-diffusion-driven instability for reaction-diffusion systems: analysis and simulations. *J Math Biol*, 70(4):709–743. 37

Madzvamuse, A., A. Wathen, and P. Maini

2003. A moving grid finite element method applied to a model biological pattern generator. *J Comput Phys*, 190(2):478–500. 21, 22, 38, 116

Maini, P. and M. Solursh

1991. Cellular mechanisms of pattern formation in the developing limb. *International review of cytology*, 129:91–133. 26

Manhart, A., D. Oelz, C. Schmeiser, and N. Sfakianakis

2017. Numerical treatment of the filament-based lamellipodium model (FBLM). In *Modeling cellular systems*, Pp. 141–159. Springer. 20

Meinhardt, H.

1999. Orientation of chemotactic cells and growth cones: models and mechanisms. *J Cell Sci*, 112(17):2867–2874. 17

Mills, J. C., N. L. Stone, J. Erhardt, and R. N. Pittman

1998. Apoptotic membrane blebbing is regulated by myosin light chain phosphorylation. *The Journal of cell biology*, 140(3):627–636. 10

Mogilner, A.

2009. Mathematics of cell motility: have we got its number? *J Math Biol*, 58(1-2):105–134. 2, 5, 6, 7, 17, 18, 26, 75

Mogilner, A. and L. Edelstein-Keshet

2002a. Regulation of actin dynamics in rapidly moving cells: a quantitative analysis. *Biophysical journal*, 83(3):1237–1258. 7, 11

Mogilner, A. and L. Edelstein-Keshet

2002b. Regulation of actin dynamics in rapidly moving cells: a quantitative analysis. *Biophys J*, 83(3):1237–1258. 26

Mogilner, A. and B. Rubinstein

2005. The physics of filopodial protrusion. *Biophysical journal*, 89(2):782–795. 7, 11

Morimoto, M.

1998. *Analytic functionals on the sphere*. Providence, R.I.: American Mathematical Society. 46

Murphy, L., C. Venkataraman, and A. Madzvamuse

2018. Parameter identification through mode isolation for reaction–diffusion systems on arbitrary geometries. *International Journal of Biomathematics*, 11(04):1850053. 27

Murray, J.

1982. Parameter space for turing instability in reaction diffusion mechanisms: a comparison of models. *J Theor Biol*, 98(1):143–163. 38

Murray, J.

2003. *Mathematical Biology II: Spatial models and biomedical applications*. New York: Springer. 30, 32, 33, 37, 39, 79

Murrell, M., P. W. Oakes, M. Lenz, and M. L. Gardel

2015. Forcing cells into shape: the mechanics of actomyosin contractility. *Nature Reviews Molecular Cell Biology*, 16(8):486–498. 6, 17, 18, 77

Neilson, M. P., J. A. Mackenzie, S. D. Webb, and R. H. Insall

2011. Modeling cell movement and chemotaxis using pseudopod-based feedback. *SIAM Journal on Scientific Computing*, 33(3):1035–1057. 12, 15, 18, 19

Nobes, C. D. and A. Hall

1995. Rho, rac, and cdc42 GTPases regulate the assembly of multimolecular focal complexes associated with actin stress fibers, lamellipodia, and filopodia. *Cell*, 81(1):53–62. 104

Noguchi, M., K. Sumiyama, and M. Morimoto

2015. Directed migration of pulmonary neuroendocrine cells toward airway branches organizes the stereotypic location of neuroepithelial bodies. *Cell reports*, 13(12):2679–2686. 104

Oster, G. F., J. D. Murray, and G. Odell

1985. Formation of microvilli. Technical report, Los Alamos National Lab., NM (USA). 59

Ouyang, Q. and H. L. Swinney

1991. Transition from a uniform state to hexagonal and striped turing patterns. *Nature*, 352(6336):610–612. 17

Paluch, E. and C.-P. Heisenberg

2009. Biology and physics of cell shape changes in development. *Current Biology*, 19(17):R790–R799. 2

Paňková, K., D. Rösel, M. Novotnỳ, and J. Brábek

2010. The molecular mechanisms of transition between mesenchymal and amoeboid invasiveness in tumor cells. *Cellular and molecular life sciences*, 67(1):63–71. x, 9

Peskin, C. S.

2002. The immersed boundary method. *Acta numerica*, 11:479–517. 20

Petrie, R. J., N. Gavara, R. S. Chadwick, and K. M. Yamada

2012. Nonpolarized signaling reveals two distinct modes of 3D cell migration. *J Cell Biol*, 197(3):439–455. 2, 8, 72, 102

Petrie, R. J. and K. M. Yamada

2012. At the leading edge of three-dimensional cell migration. *J Cell Sci*, 125(24):5917–5926. 2, 3, 8

Petrie, R. J. and K. M. Yamada

2015. Fibroblasts lead the way: a unified view of 3D cell motility. *Trends in cell biology*, 25(11):666–674. 15

Poincloux, R., O. Collin, F. Lizárraga, M. Romao, M. Debray, M. Piel, and P. Chavrier

2011. Contractility of the cell rear drives invasion of breast tumor cells in 3D matrigel. *Proceedings of the National Academy of Sciences*, 108(5):1943–1948. 2, 8

Pollard, T. D. and G. G. Borisy

2003. Cellular motility driven by assembly and disassembly of actin filaments. *Cell*, 112(4):453–465. 6

Porter, K., D. Prescott, and J. Frye

1973. Changes in surface morphology of chinese hamster ovary cells during the cell cycle. *The Journal of cell biology*, 57(3):815–836. 10

Pozrikidis, C.

2005. Numerical simulation of cell motion in tube flow. *Annals of Biomedical Engineering*, 33(2):165–178. 19

Press, W. H., S. A. Teukolsky, W. T. Vetterling, and B. P. Flannery

2007. *Numerical recipes 3rd edition: The art of scientific computing*. Cambridge university press. 114

Prigogine, I. and R. Lefever

1968. Symmetry breaking instabilities in dissipative systems. ii. *The Journal of Chemical Physics*, 48(4):1695–1700. 37

Pullarkat, P. A., P. A. Fernández, and A. Ott

2007. Rheological properties of the eukaryotic cell cytoskeleton. *Physics Reports*, 449(1-3):29–53. ix, 4, 5

Rafelski, S. M. and J. A. Theriot

2004. Crawling toward a unified model of cell motility: spatial and temporal regulation of actin dynamics. *Annual review of biochemistry*, 73(1):209–239. 2

Rätz, A. and M. Röger

2014. Symmetry breaking in a bulk–surface reaction–diffusion model for signalling networks. *Nonlinearity*, 27(8):1805. 104

Reddy, J.

1993. *An introduction to the finite element method.* New York: McGraw-Hill. 25, 110

Rubinstein, B., M. F. Fournier, K. Jacobson, A. B. Verkhovsky, and A. Mogilner

2009. Actin-myosin viscoelastic flow in the keratocyte lamellipod. *Biophysical journal*, 97(7):1853–1863. 12, 13, 16, 17, 18, 75, 77

Rubinstein, B., K. Jacobson, and A. Mogilner

2005. Multiscale two-dimensional modeling of a motile simple-shaped cell. *Multiscale Modeling & Simulation*, 3(2):413–439. 12, 13, 18, 20, 21

Ruuth, S.

1995. Implicit-explicit methods for reaction-diffusion problems in pattern formation. *J Math Biol*, 34(2):148–176. 39, 42, 106, 114

Saad, Y. and M. H. Schultz

1986. Gmres: A generalized minimal residual algorithm for solving nonsymmetric linear systems. *SIAM Journal on scientific and statistical computing*, 7(3):856–869. 114

Sahai, E. and C. J. Marshall

2003. Differing modes of tumour cell invasion have distinct requirements for Rho/ROCK signalling and extracellular proteolysis. *Nature cell biology*, 5(8):711. 2, 8, 9, 10

Sakamoto, Y., S. Prudhomme, and M. Zaman

2014. Modeling of adhesion, protrusion, and contraction coordination for cell migration simulations. *Journal of mathematical biology*, 68(1-2):267–302. 12, 14, 20, 21

Sanz-Moreno, V., C. Gaggioli, M. Yeo, J. Albrengues, F. Wallberg, A. Viros, S. Hooper, R. Mitter, C. C. Féral, M. Cook, et al.

2011. ROCK and JAK1 signaling cooperate to control actomyosin contractility in tumor cells and stroma. *Cancer cell*, 20(2):229–245. 2, 8

Savage, N.

2015. High-protein research. *Nature*, 527(7576):S6. 23

Schmidt, A., K. Siebert, D. Köster, O. Kriessl, and C. Heine

2007. Alberta-an adaptive hierarchical finite element toolbox. *URL http://www. alberta-fem. de*. 103

Schnakenberg, J.

1979. Simple chemical reaction systems with limit cycle behaviour. *J Theor Biol*, 81(3):389–400. 17, 37

Schneider, L., M. Cammer, J. Lehman, S. K. Nielsen, C. F. Guerra, I. R. Veland, C. Stock, E. K. Hoffmann, B. K. Yoder, A. Schwab, et al.

2010. Directional cell migration and chemotaxis in wound healing response to PDGF-AA are coordinated by the primary cilium in fibroblasts. *Cellular physiology and Biochemistry*, 25(2-3):279–292. 7

Schopf, J. W., A. B. Kudryavtsev, A. D. Czaja, and A. B. Tripathi

2007. Evidence of Archean life: stromatolites and microfossils. *Precambrian Research*, 158(3-4):141–155. 3

Shao, D., H. Levine, and W.-J. Rappel

2012. Coupling actin flow, adhesion, and morphology in a computational cell motility model. *Proceedings of the National Academy of Sciences*, 109(18):6851–6856. 12, 16, 17, 18, 20, 77

Sherratt, J., P. Martin, J. Murray, and J. Lewis

1992. Mathematical models of wound healing in embryonic and adult epidermis. *Math Med Biol*, 9(3):177–196. 26

Sick, S., S. Reinker, J. Timmer, and T. Schlake

2006. Wnt and dkk determine hair follicle spacing through a reaction-diffusion mechanism. *Science*, 314(5804):1447–1450. 26

Simon, C. M., E. M. Vaughan, W. M. Bement, and L. Edelstein-Keshet

2013. Pattern formation of Rho GTPases in single cell wound healing. *Molecular biology of the cell*, 24(3):421–432. 104

Stephanou, A., M. Chaplain, and P. Tracqui

2004. A mathematical model for the dynamics of large membrane deformations of isolated fibroblasts. *Bulletin of mathematical biology*, 66(5):1119. 12, 17, 19, 59, 60, 61, 64

Stewart, G.

2002. A Krylov–Schur algorithm for large eigenproblems. *SIAM Journal on Matrix Analysis and Applications*, 23(3):601–614. 38

Strang, G. and G. J. Fix

1973. *An analysis of the finite element method*, volume 212. Prentice-hall Englewood Cliffs, NJ. 54

Strychalski, W., D. Adalsteinsson, and T. C. Elston

2010. Simulating biochemical signaling networks in complex moving geometries. *SIAM Journal on Scientific Computing*, 32(5):3039–3070. 19

Sun, M. and M. H. Zaman

2017. Modeling, signaling and cytoskeleton dynamics: integrated modeling-experimental frameworks in cell migration. *Wiley Interdisciplinary Reviews: Systems Biology and Medicine*, 9(1). 16

Svitkina, T. M., A. B. Verkhovsky, K. M. McQuade, and G. G. Borisy

1997. Analysis of the actin–myosin II system in fish epidermal keratocytes: mechanism of cell body translocation. *The Journal of cell biology*, 139(2):397–415. 7

Taylor, M.

1996. *Partial Differential Equations II*. New York: Springer. 40

te Boekhorst, V., L. Preziosi, and P. Friedl

2016. Plasticity of cell migration in vivo and in silico. *Annual Review of Cell and Developmental Biology*, 32:491–526. 2, 8

Thomas, D. and J. E. Kernevez

1976. *Analysis and control of immobilized enzyme systems*. Amsterdam: North-Holland Pub. Co. 38

Tjhung, E., A. Tiribocchi, D. Marenduzzo, and M. Cates

2015. A minimal physical model captures the shapes of crawling cells. *Nature communications*, 6. 8, 12, 14

Tozluoğlu, M., A. L. Tournier, R. P. Jenkins, S. Hooper, P. A. Bates, and E. Sahai

2013. Matrix geometry determines optimal cancer cell migration strategy and modulates response to interventions. *Nature cell biology*, 15(7):751–762. 12, 14, 20

Turing, A. M.

1952. The chemical basis of morphogenesis. *Philosophical Transactions of the Royal Society of London B: Biological Sciences*, 237(641):37–72. 17, 26, 32

Venkataraman, C., T. Sekimura, E. A. Gaffney, P. K. Maini, and A. Madzvamuse

2011. Modeling parr-mark pattern formation during the early development of amago trout. *Phys Rev E*, 84(4):041923. 39, 54, 58

Wang, J. and H. Gao

2011. On hyperelastic stress-strain law of F-actin bundles. *Theoretical and Applied Mechanics Letters*, 1(1). 16

Webb, D. J., J. T. Parsons, and A. F. Horwitz

2002. Adhesion assembly, disassembly and turnover in migrating cells–over and over and over again. *Nature cell biology*, 4(4):E97. 11

Wilson, C. A., M. A. Tsuchida, G. M. Allen, E. L. Barnhart, K. T. Applegate, P. T. Yam, L. Ji, K. Keren, G. Danuser, and J. A. Theriot

2010. Myosin II contributes to cell-scale actin network treadmilling through network disassembly. *Nature*, 465(7296):373. 7

Wolf, K., I. Mazo, H. Leung, K. Engelke, U. H. Von Andrian, E. I. Deryugina, A. Y. Strongin, E.-B. Bröcker, and P. Friedl

2003. Compensation mechanism in tumor cell migration. *The Journal of cell biology*, 160(2):267–277. 2, 8, 9, 10

Wolgemuth, C. W., J. Stajic, and A. Mogilner

2011. Redundant mechanisms for stable cell locomotion revealed by minimal models. *Biophysical journal*, 101(3):545–553. 16, 17, 18, 75, 77

Wolgemuth, C. W. and M. Zajac

2010. The moving boundary node method: A level set-based, finite volume algorithm with applications to cell motility. *Journal of computational physics*, 229(19):7287–7308. 12, 19

Yang, F. W., C. Venkataraman, V. Styles, and A. Madzvamuse

2017. A robust and efficient adaptive multigrid solver for the optimal control of phase field formulations of geometric evolution laws. *Communications in Computational Physics*, 21(1):65–92. 20

Yang, L., M. Dolnik, A. M. Zhabotinsky, and I. R. Epstein

2002. Pattern formation arising from interactions between Turing and wave instabilities. *The Journal of chemical physics*, 117(15):7259–7265. 87

Zaman, M. H., R. D. Kamm, P. Matsudaira, and D. A. Lauffenburger

2005. Computational model for cell migration in three-dimensional matrices. *Biophysical journal*, 89(2):1389–1397. 12, 14, 16

Zaman, M. H., L. M. Trapani, A. L. Sieminski, D. MacKellar, H. Gong, R. D. Kamm, A. Wells, D. A. Lauffenburger, and P. Matsudaira

2006. Migration of tumor cells in 3D matrices is governed by matrix stiffness along with cell-matrix adhesion and proteolysis. *Proceedings of the National Academy of Sciences*, 103(29):10889–10894. 12, 16

Zhu, J. and A. Mogilner

2016. Comparison of cell migration mechanical strategies in three-dimensional matrices: a computational study. *Interface Focus*, 6(5):20160040. 8, 12, 14, 104

Zill, D. and M. Cullen

2000. *Advanced Engineering Mathematics*. Jones and Bartlett Publishers International. 28